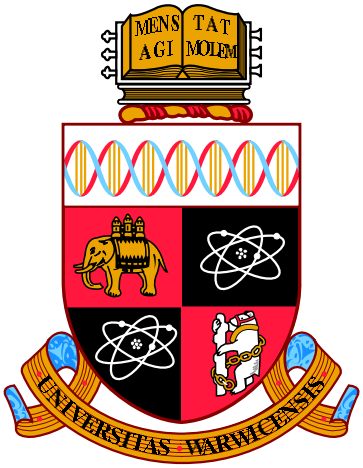

New Electrochemical Methods for Visualizing Interfacial Ion Fluxes

by

Binoy Paulose Nadappuram

Thesis

Submitted to the University of Warwick

for the degree of

Doctor of Philosophy

Chemistry

July 2015

THE UNIVERSITY OF WARWICK

Contents

List of Tables

List of Figures

Acknowledgments

I find myself incredibly fortunate to have had the opportunity to do my PhD at the Warwick Electrochemistry and Interfaces Group and at the University of Warwick.

First, to my supervisor Prof Patrick Unwin, I thank you for your leap of faith in giving me the opportunity to work on a subject that I really learned to enjoy, and for the freedom to explore and experiment with my project. The time you took to mentor and advice and your incredible support and encouragement in the midst of difficult circumstances were paramount to the completion of this thesis. I am appreciative to your comments and critiques that ultimately made my work stronger and for pushing the limits of my reasoning and understanding of my work.

I would also like to acknowledge and thank Prof. Julie Macpherson for being kind and supportive throughout my studies. Your door was always open for the much needed personal counsel and I am grateful for steering me to the right direction, especially when I was thinking about whats next.

Thank you Josh for your mentorship, guidance and friendship; you have led by example in all areas from success as a scientist, being an effective leader, collaborator and a caring friend. I really enjoyed working with you. Also thank you for all the "satsuma" bets, "Subway" walks and "KFC" drives and the never ending discussions about science, politics, and everything under the sky.

I would like to thank Dr Alex Colburn for the excellent technical help, for

his constant willingness to push the boundaries to design the best instruments without which this work would not have been possible.

Thanks to Dr Kim McKelvey for his contributions to this thesis and the time spent reviewing and providing valuable feedbacks on my projects especially during the earlier days of my research, to Dr Robert Lazenby for helping me with the lab induction and training and for the numerous helps during all these years. Further, thanks to Dr Kate Meadows, Rehab Al Botros and Dr Tahani Bawazeer who contributed to the work mentioned in this thesis and for doing their best to teach me various electrochemical techniques. Also thanks to Dr Aleix G*üe*ll for helping with the illustrator and Sophie Kinnear for helping with MatLab and LabView.

Special thanks to James, Laura, Steve, Jon, Hollie, and Michael for the movie/ (bean) game nights and making me feel like home and Lucy for helping with the accomodation. Thanks to, David for the friendship, the science and fun inside and outside the lab, Minkyung for being a good friend and letting me perfect on 'binnoying', you and crew made my last trying few months most enjoyable, and to my batch mates, Barak, Hui, Jenny and Rob C for sharing the PhD worries.

To all the past and present members of the group,especially the C111 inhabitants, thank you for your friendship, for always making the time to chat, listen, grab a cup of tea, constantly encouraging, and keeping me grounded in reality. This journey was a whole lot more meaningful with you all around to share in it.

To all my friends in India, Singapore, and United Kingdom, thank you for the love, understanding, and encouragement that each of you have extended to me, especially to Daiyi, Pamela and Archana, you were always there for me and I would not have got through this without you three.

To the extended family at JSOC Birmingham, your love and prayers have been a source of strength and light during the last four years.

Finally I acknowledge the University of Warwick (Chancellor Scholarship) and European Research Council (ERC-2009-AdG247143-QUANTIF) for funding my Research.

Declarations

The work presented in this thesis is entirely original and my own except for the following contributions: 1) Chapter 3. Finite element method simulations and thylakoid membrane preparations were carried out by Dr Kim McKelvey. 2) Chapter 4. Finite element method simulations were carried out by Rehab Al Botros. 3) Chapter 5. Single-walled carbon nanotube samples were prepared by Ms. Minkyung Kang and experiments were performed with Dr Joshua Bayers. 4) Chapter 6. Experiments were performed jointly with Dr Joshua Bayers and the simulations were developed by Mr David Perry. 5) Chapter 7. Experiments were carried out with and Finite element method simulations were developed by Dr Katherine Meadows.

I confirm that this thesis has not been submitted for any degree at another university.

Part of this thesis have been published as detailed below:

K. McKelvey, **B. P. Nadappuram**, P. Actis, Y. Takahashi, Y. E. Korchev, T. Matsue, C. Robinson, and P. R. Unwin, Fabrication, Characterization, and Functionalization of Dual Carbon Electrodes as Probes for Scanning Electrochemical Microscopy (SECM), *Anal. Chem.*, **2013**, 85, 7519-7526.

B. P. Nadappuram, K. McKelvey, R. Al-Botros, A. W. Colburn, and P. R.

Unwin, Fabrication and Characterization of Dual Function Nanoscale pH-Scanning Ion Conductance Microscopy (SICM) Probes for High Resolution pH Mapping, *Anal. Chem.*, **2013**, 85, 8070-8074.

B. P. Nadappuram, K. McKelvey, J. C. Byers, A. G. G*ü*ell, A. W. Colburn, R. A. Lazenby, P. R. Unwin, Quad-Barrel Multifunctional Electrochemical and Ion Conductance Probe for Voltammetric Analysis and Imaging, *Anal. Chem.*, **2015**, 87, 3566-3573.

J. C. Byers, **B. P. Nadappuram**, D. Perry, K. McKelvey, A. W. Colburn, and P. R. Unwin, Single Molecule Electrochemical Detection, submitted to *Anal. Chem.*, **2015**, 87, 10450-10456.

K. E. Meadows, **B. P. Nadappuram**, and P.R. Unwin, A new approach for the fabrication of microscale lipid bilayers at glass pipets: application to quantitative passive permeation visualization, *Soft Matter.* **2014**, 10, 8433-8441

Abstract

This thesis is concerned with the development of new electrochemical methods for the visualization of ion fluxes at various interfaces. These techniques allow spatially resolved visualization and quantification of ion fluxes associated with various physiochemical and biological processes aiding to understand the mechanism and kinetics of such processes along with mapping the heterogeneity of such interfaces. In the first part of this thesis, a fast an inexpensive way to fabricate a nanoscale dual carbon electrode system was introduced. These electrode systems are well suited for detection and quantification of interfacial fluxes using scanning electrochemical microscopy because of their relatively small tip size enabling close positioning to an interface, while the small inter-electrode distance leads to high sensitivity. To enhance the capability of electrochemical scanning probe microscopy to simultaneous topography and potentiometric imaging of interfaces, a new pH-scanning ion conductance microscopy probe was developed and tested as a part of this thesis. Further, a quad-barrel multifunctional electrochemical and ion conductance probe for voltammetric analysis and electrochemical imaging of interfaces was developed and characterized in this study. These probes are amenable to further functionalization thus offering opportunities for functional imaging of both conducting and insulating pristine surfaces along with the capability of assembling nanoscale electrochemical cells for high sensitivity measurements. The ability of these probes

for performing single molecule electrochemical detection was also explored in this thesis. Weak acids constitute an important group of molecules transported passively across the cell membrane. Most of the weak acids upon reaching specific intracellular sites produce various pharmacological responses which are widely exploited in therapeutics. It is thus extremely timely to have available experimental methods to accurately determine their permeation rates across bilayer membranes. A new method of forming lipid bilayers at the end of a glass pipet was reported in the later part of this thesis for quantitative passive permeation visualization. An attractive feature of all the techniques described herein is that they are very well-defined and amenable to precise modelling of mass transport/reactivity. This was accomplished in this thesis using finite element modelling.

Abbreviations

2D	Two Dimensional
3D	Three Dimensional
AC	Alternating Current
AC-SECM	Alternating Current- Scanning Electrochemical Microscopy
BLM	Bilayer Lipid Membrane
CLSM	Confocal Laser Scanning Microscopy
CV	Cyclic Voltammetry
CVD	Chemical Vapour Deposition
DAQ	Data Acquisition
DC	Direct Current
DCE	Dual Carbon Electrodes
DCMU	3-(3,4-Dichlorophenyl)-1,1-Dimenthylurea
DPPC	1,2-Dipalmitoyl-Sn-Glycero-3-Phosphocholine
EC-SPM	Electrochemical Scanning Probe Microscopy
FcTMA	Ferrocenylmethyltrimethylammonium
FEM	Finite Element Method
FE-SEM	Field Emission-Scanning Electron Microscope
FIB	Focused Ion Beam
FPGA	Field-Programmable Gate Array
G/C	Generation/Collection

HEPES	4-(2-Hydroxyethyl)-1-Piperazineethanesulfonic Acid
HOMO	Highest Occupied Molecular Orbital
HOPG	Highly Oriented Pyrolytic Graphite
IC-SECM	Intermittent Contact Scanning Electrochemical Microscopy
LSV	Linear Sweep Voltammetry
LUMO	Lowest Unoccupied Molecular Orbital
NADPH	Nicotinamide Adenine Dinucleotide Phosphate
PC	Personal Computer
PC	Phosphatidylcholine
PGA	Poly-L-Glutamic Acid
PLL	Poly-L-Lysine
PS I	Photosystem I
PS II	Photosystem II
QRCE	Quasi-Reference Counter Electrode
RTIL	Room Temperature Ionic Liquid
RuHax	Hexaaminеruthenium
SECCM	Scanning Electrochemical Cell Microscopy
SECM	Scanning Electrochemical Microscopy
SICM	Scanning Ion Conductance Microscopy
SMCM	Scanning Micropipet Contact Method
SWNT	Single-Walled Carbon Nanotube
SMED	Single Molecule Electrochemical Detection
TPM-SECM	Tip Position Modulation Scanning Electrochemical Microscopy
UME	Ultramicroelectrode
USL	Unstirred Layer

Chapter 1

Introduction

Spatially resolved visualization of interfacial fluxes is hugely valuable in explaining complex physiochemical and biological processes.The aim of this thesis is the development of new electrochemical scanning probe microscopy based methods for visualization of interfacial fluxes. This chapter provides an overview of the basic electrochemistry principles and summarizes the various electrochemical techniques explored in this study along with their applications and limitations to give a context to the subsequent chapters.

1.1 Electrode Reactions

Electrochemical scanning probe microscopy (EC-SPM) works by employing a tip electrode to measure electrochemical signals, when it is held or moved in an electrolyte solution in the vicinity of a substrate. This electrochemical signal is often generated as a result of an electron transfer reaction between the electrode and an electroactive species in the electrolyte solution.[1] General schematic of such a reaction is shown in Figure 1.1 where an electroactive species O is transported

from the bulk solution to the electrode surface, where it undergoes a potential dependent electron transfer reaction producing the species R, which is then transported back to the bulk solution. The electron transfer in these reactions results in a measurable current, which originates from both faradaic and non-faradaic processes, the former being the processes involving the transfer of an electric charge (electron) across the electrode/electrolyte interface and the latter associated with processes such as adsorption and desorption, which changes the structure of the electrode/electrolyte interface with change in potential of the electrode and/or solution composition.[2]

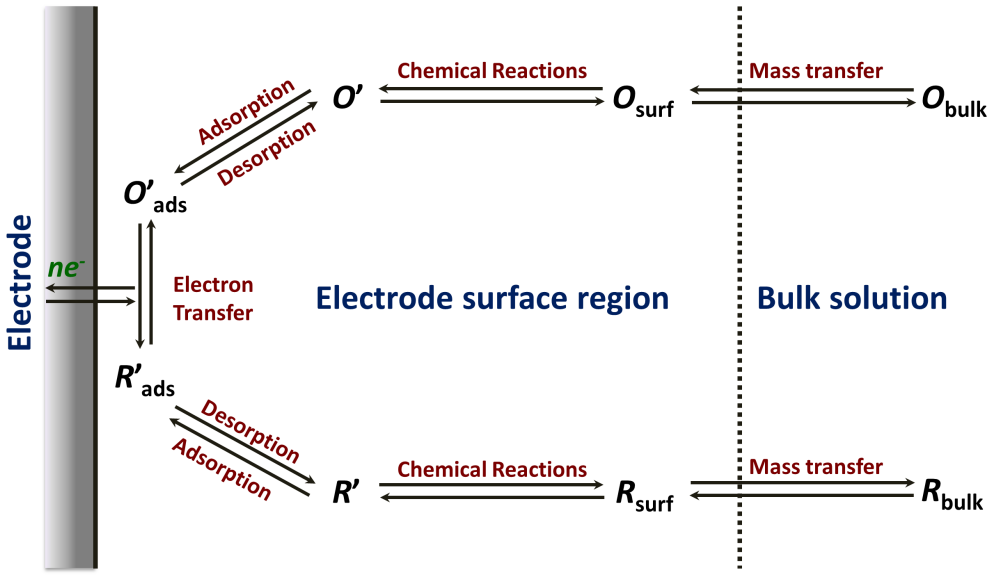

Figure 1.1: Schematic of a general electrode reaction. The electroactive species O is transported from the bulk solution to the electrode surface, where it undergoes a potential dependent electron transfer reaction producing the species R, which is then transported back to the bulk solution.[2]

The rate of an electrode reaction is often governed by the rate of different electrode processes such as the mass transfer of the reactant to the electrode, heterogeneous electron transfer involving nonadsorbed species and the rate of other surface reactions such as adsorption, desorption, or crystallization where the slowest step called the rate determining step decides the overall rate of the reaction. For systems used in EC-SPMs mentioned herein, the faradaic processes are usually of primary interest, where the electrode reaction rate depends on the mass transport of electroactive species towards and away from the electrode surface and the rate of electron transfer at the electrode surface.[2]

1.1.1 Mass Transport

Mass transport, in an electrochemical system, is the movement of electroactive species from one location in the electrolyte solution to another, driven either by the differences in electrical or chemical potential between these two locations or by the movement of a volume element of the electrolyte solution. For most electrode systems, mass transport from bulk towards the electrode interface is the kinetically limiting step, and is defined by the Nernst-Planck equation[3] as,

$$J_{\mathrm{i}} = -D_{\mathrm{i}} \nabla C_{\mathrm{i}} - \frac{z_i F}{RT} D_{\mathrm{i}} C_{\mathrm{i}} \phi + C_{\mathrm{i}} \nu \tag{1}$$

where J_{i} is the flux of the electroactive species i from/to the electrode surface, D_{i}, C_{i}, z_{i} are the diffusion coefficient, concentration and charge of the of the electroactive species i ,ϕ and ν are the electrostatic potential and velocity factor of the solution respectively. The three components in the right hand side of the equation represent contributions of three modes of transport of the electroactive

species in the solution namely diffusion, migration and convection, to the flux.

Diffusion in an electrochemical system is the movement of the electroactive species under the influence of a concentration gradient, generally caused as a result of the production or depletion of the electroactive species at the electrode surface. The rate of diffusion at a given point in a solution depends upon the concentration gradient of the electroactive species at that point, described by Ficks first law of diffusion[3] as,

$$J_{\mathrm{i,d}} = \text{-}D_{\mathrm{i}} \nabla C_{\mathrm{i}} \tag{2}$$

where D_{i} is the diffusion coefficient. Further the rate of change in concentration of the electroactive species close to the electrode surface due to diffusion can be estimated by using Ficks second law of diffusion[3]

$$\frac{\partial Ci}{\partial t} = D_{\mathrm{i}} \nabla^2 C_{\mathrm{i}} \tag{3}$$

where the geometry dependent Laplace operator ∇^2 could be used to describe both 2D and 3D and diffusion fields.

Migration is the movement of charged species within an electrolyte solution under the influence of an applied electric field. When an electric field is applied to an electrochemical system, the charged species are either electrostatically attracted to, or repelled from the electrode/electrolyte interface giving rise to a migratory flux which in turn affect the mass transport of the electroactive species in that electrochemical system. The migratory flux induced in such a system ($J_{\mathrm{i,m}}$) is described by the equation

$$J_{\mathrm{i,m}} = \text{-} \frac{z_i F}{RT} D_{\mathrm{i}} C_{\mathrm{i}} \nabla \phi \tag{4}$$

where ($\nabla\phi$) is the strength of the external electric field and the magnitude of ($\frac{z_i F}{RT} D_\mathrm{i}$) denotes the mobility of the electroactive species (Ui). In most of the electrochemical systems, the effect of migration is often suppressed by the inclusion of an inert supporting electrolyte in sufficiently excess amount (typically, 100 times the concentration of the electroactive species). The presence of a supporting electrolyte in excess concentration also serves to significantly reduce the electrolyte solution resistance and thereby reducing the ohmic drop effects.[1,3]

Convection in an electrochemical system describes the movement of electroactive species due to the movement of the electrolyte solution caused by factors like thermal gradients, density variation (natural convection) or by the application of an external mechanical force (forced convection). For electrochemical systems mentioned in this thesis, the influence of convection on mass transport was kept at minimum by maintaining stable temperature and avoiding any unnecessary solution movement.

1.1.2 Electron Transfer

Electron transfer occurs at the electrode surface wherein an electroactive species either gains or looses electrons under the influence of an applied electrical potential.[2] The applied potential either increases or decreases the Fermi level energy of the free electrons in the electrode surface, and hence facilitates the transfer of electrons between the electroactive species and the electrode. A decrease in Fermi level of the free electron in the electrode surface (by the application of a positive potential to the electrode), below the energy of the highest occupied molecular orbital (HOMO) of the electroactive species in the solution can trigger the transfer

of electrons from the electroactive species into the electrode resulting in the electrochemical oxidation of the electroactive species at the electrode surface (Figure 1.2A).

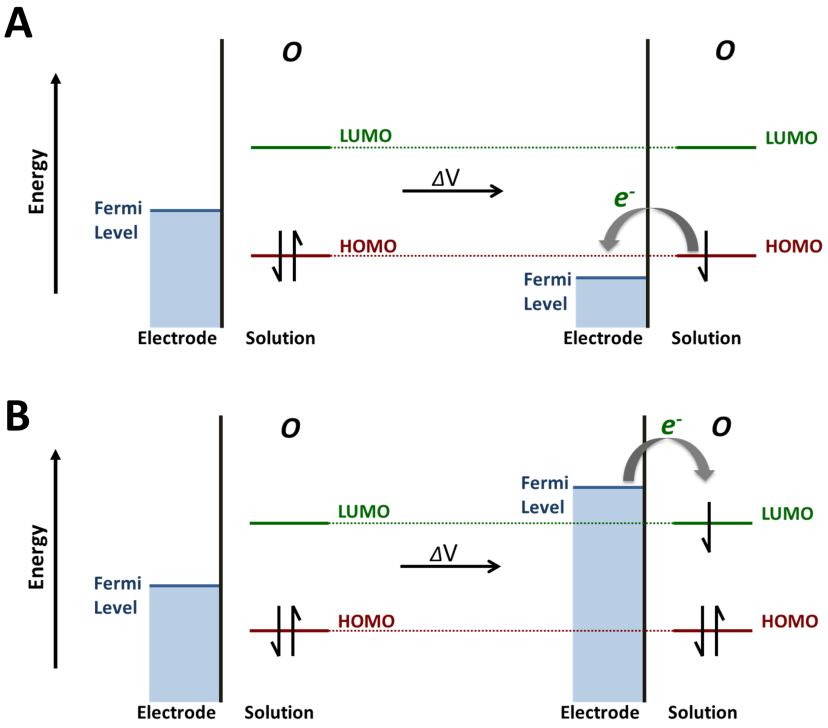

Figure 1.2: Energy level diagrams of electron transfer reaction at the electrode surface. (A) Decrease in Fermi level of the electrode with applied potential favours the transfer of electron(s) from the highest occupied molecular orbital (HOMO) of the electroactive species O into the electrode resulting in the oxidation of the electroactive species whereas, (B) an increase in Fermi level of the electrode induces the transfer of electron(s) from the electrode surface to the lowest unoccupied molecular orbital (LUMO) of the electroactive species (reduction of the electroactive species)[4]

In cases where the Fermi level of the free electrons in the electrode surface is higher than the energy of the lowest unoccupied molecular orbital (LUMO) of the electroactive species, electron transfer will take place from the electrode into the

species in solution resulting in the electrochemical reduction of the species (Figure 1.2B).[4]

For electrochemical systems, where the rate of electron transfer at the electrode surface is much higher than the mass transport towards the electrode surface, the relationship between applied potential and the concentrations of oxidized (O) and reduced (R) species for the reversible equilibrium reaction,

$$O + n\mathrm{e}^{-} \rightleftharpoons R$$

is described by the Nernst equation[2] as,

$$E = E^{\Theta} + \frac{RT}{neF} \ln \frac{[O]}{[R]} \tag{5}$$

where$E$ is the electrode potential, E^{Θ}, R, T, F and n are the standard electrode potential of the redox couple, universal gas constant, temperature, Faraday constant and number of electrons transferred during the reaction.

The Nernst equation can be successfully employed to explain electrode reactions in cases where mass transport is the kinetically limiting step, however for systems where this is not the case, electron transfer kinetics could be explained by using the Butler-Volmer equation,[2]

$$k_{\mathrm{f}} = k^{\circ} \exp\left[-\alpha \frac{(E-E^{\circ'})F}{RT}\right] \tag{6}$$

$$k_{\mathrm{b}} = k^{\circ} \exp\left[1-\alpha \frac{(E-E^{\circ'})F}{RT}\right] \tag{7}$$

where, k° is the rate constant, k_{f},k_{b} are the first order heterogeneous rate constants for the forward and backward (oxidation and reduction) reactions respectively, α

is the transfer coefficient, and $E^{\circ'}$ is the electrode formal potential.

1.2 Ultramicroelectrodes

EC-SPMs generally employ a disk-shaped ultramicroelectrode (UME) to measure the perturbations in electrochemical response while they are in close proximity to a substrate surface, to investigate the nature and electrochemical properties of that substrate.[2, 5-8] UMEs used in EC-SPMs are generally fabricated by sealing a metal wire or carbon fiber (radius typically <25 μm) in a tapered glass capillary and polishing the end of the capillary to expose the disk-shaped electrode.[1,2, 7-18]

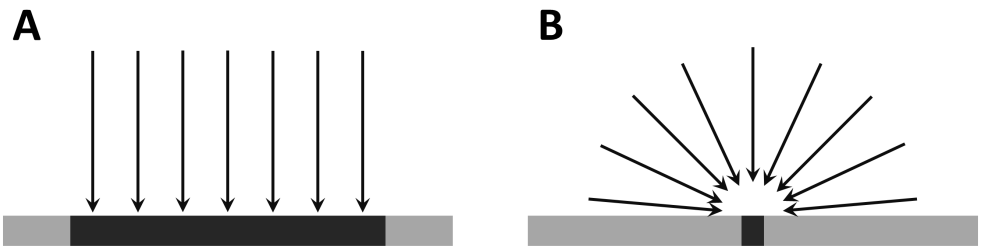

Figure 1.3: Planar (A) and hemispherical diffusion (B) of electroactive species towards the electrode surface.[1]

Unlike a macroelectrode where planner diffusion of the electroactive species to the electrode surface causes a fast depletion of the species near the surface, the diffusion of species to a UME is hemispherical due to the increased contribution of the radial diffusion component, resulting a high mass transport rate ideal for EC-SPM measurements (Figure 1.3).[1,2,19] This high mass transport towards the

UME surface enables the electrochemical current generated at the UME to reach steady state within fraction of a second. For a disk-shaped UME, this steady-state diffusion-limited current (i_α) in a bulk electrolyte solution containing an electroactive species is described using an analytical solution to Ficks first law[1,2] as,

$$i_\alpha = 4 n_e a F D c_\alpha \tag{8}$$

where a is the radius of the UME, D and c_α are the diffusion coefficient and concentrations of the electroactive species respectively.

Besides the high mass transport rate, owing to their smaller size, UMEs offer high current densities and the currents typically measured at UMEs are low (in the order of pA to nA). This low current significantly decreases the resistive ohmic drops in the electrolyte solution and is relatively immune to convective effects like stirring in the solution due to the high flux of the electroactive species to the electrode surface.[1,6,7,20,21] This enables the UME used in EC-SPM to be treated as a steady state system for quantitative electrochemical measurements near to surfaces and interfaces.[1,7,8]

1.3 Scanning Electrochemical Microscopy

Scanning Electrochemical Microscopy (SECM), developed by Bard[1, 5-8] in 1989 is one of the earliest EC-SPM techniques employing a disk shaped UME also known as a tip to induce an electrochemical reaction near to a surface of interest while measuring the current changes as a function of the surface activity.[1,2, 5-8, 11, 19, 22-34] The electrochemical current recorded at an SECM tip electrode is a function of the

solution composition, the distance between the tip and substrate surface and the nature of the substrate itself. If the potential applied to the tip is sufficiently large to oxidize or reduce the electroactive species at a diffusion limited rate, then the current will rapidly assume a steady state value, the magnitude of which depends on the concentration of the electroactive species.[1,2,5,19]

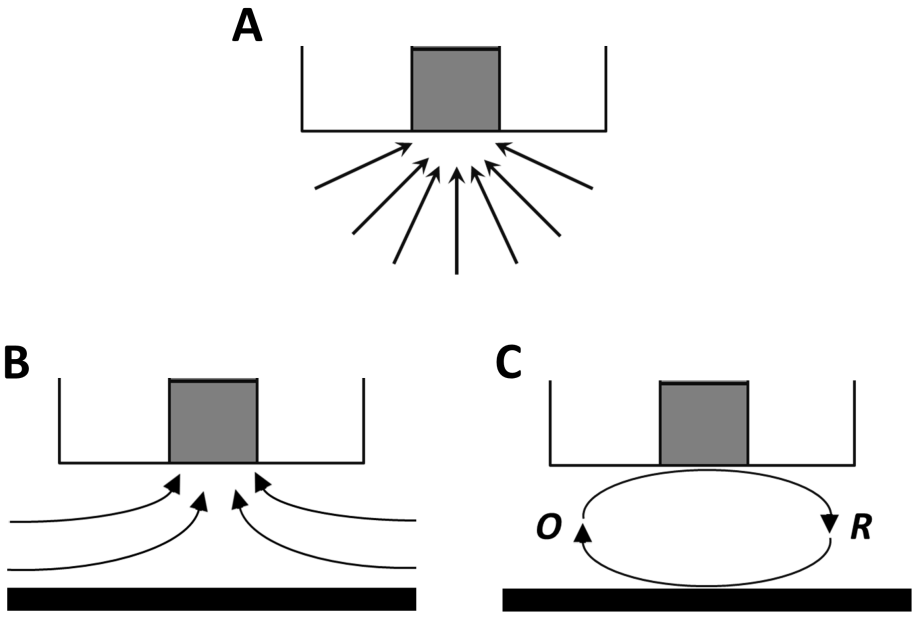

Figure 1.4: Feedback modes in SECM. (A) When the tip electrode is placed far from the substrate surface, the diffusion layer around the electrode is nearly hemispherical resulting in a steady-state electrochemical current. (B) The electrochemical current starts to decrease (negative feedback) as the tip approaches an insulating surface due to the partial blocking of the diffusion of electroactive species towards the tip electrode. (C) An increase in electrochemical current (Positive feedback) is observed when the tip electrode approaches a conductive surface which regenerates the reactive species thereby enhancing the diffusion towards the tip electrode.[1]

When the tip electrode is placed far from the substrate surface, the diffusion layer around the electrode is nearly hemispherical (Fig 1.4A), but when the tip is

brought near to the surface, this diffusion layer changes depending on the nature of the surface and this change in diffusion layer results in a change in electrochemical current which is often used as the feedback signal to characterize such surfaces. In case of insulting surfaces, part of the diffusion layer will be blocked when the tip is near to the surface resulting in a decrease in electrochemical current (negative feedback, Figure 1.4B), where as in case of a conducting surface, in spite of the partial blocking of the diffusion layer, the electrochemical current increases due the recycling of the electroactive species at the substrate surface (positive feedback, Figure 1.4C).[1,5,6] This mode of operation of SECM is generally called the feedback mode SECM. A plot of the tip current as a function of the tip-surface separation, as the tip is moved towards the substrate is called an approach curve and is the simplest form of SECM measurement. When complemented with digital simulation, such approach curves could be used to estimate the heterogeneous rate constants for the oxidation or reduction of an electroactive species at substrate surfaces.[26,35,36]

Apart from the feedback mode SECM, various other SECM configurations were also realized namely, competitive mode, tip generation/substrate collection mode and substrate generation/tip collection mode.[1, 6, 37, 38] In competitive mode, both the substrate and the tip are held at the same potential to either oxidise or reduce the same electroactive species and hence they compete for the very same species present in the small gap between the sample surface and the accurately positioned tip (Figure 1.5A).

In tip generation/substrate collection mode, the tip electrode and substrate were held at two different potentials, so that the tip oxidizes or reduces the electroactive species A to produce another species B which will then diffuse towards

the substrate where it undergoes another reaction (oxidation or reduction) to produce the species C (Figure 1.5B) or in some cases the starting species A (Figure 1.5C).

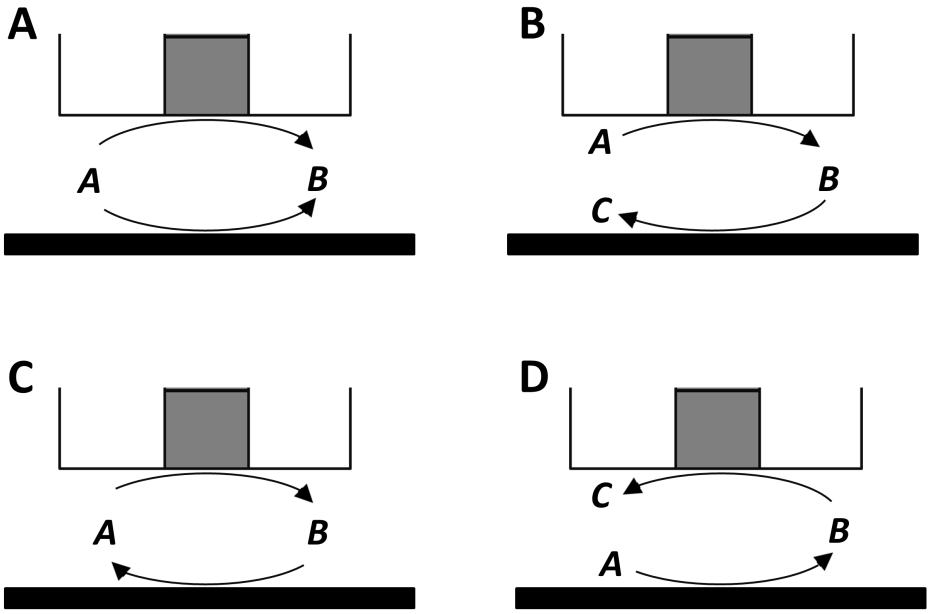

Figure 1.5: Different SECM configurations. (A) Competitive mode where both the substrate and the tip were held at the same potential and generate the same species. (B) Tip generation/substrate collection mode where the tip electrode generates species B and the substrate converts it into either the starting species or (C) another species. (D) Substrate generation/tip collection mode where the substrate electrode generates species B and the tip electrode converts it into another species or converts back into the initial species (not shown).[1]

In case of substrate generation/tip collection mode, the substrate electrode is held at a potential favouring the conversion of the electroactive species A in the electrolyte solution to another species B which will then diffuse towards the tip electrode where it undergoes an oxidation or reduction reaction to species C, as shown in Figure 1.5D (or in some cases the starting species A).

In SECM, the tip and the substrate are part of an electrochemical cell along with a reference and an auxiliary electrode immersed in an electrolyte containing a redox mediator. General schematics of a typical SECM set-up in shown in Figure 1.6.[5, 7, 8, 19, 39-43]

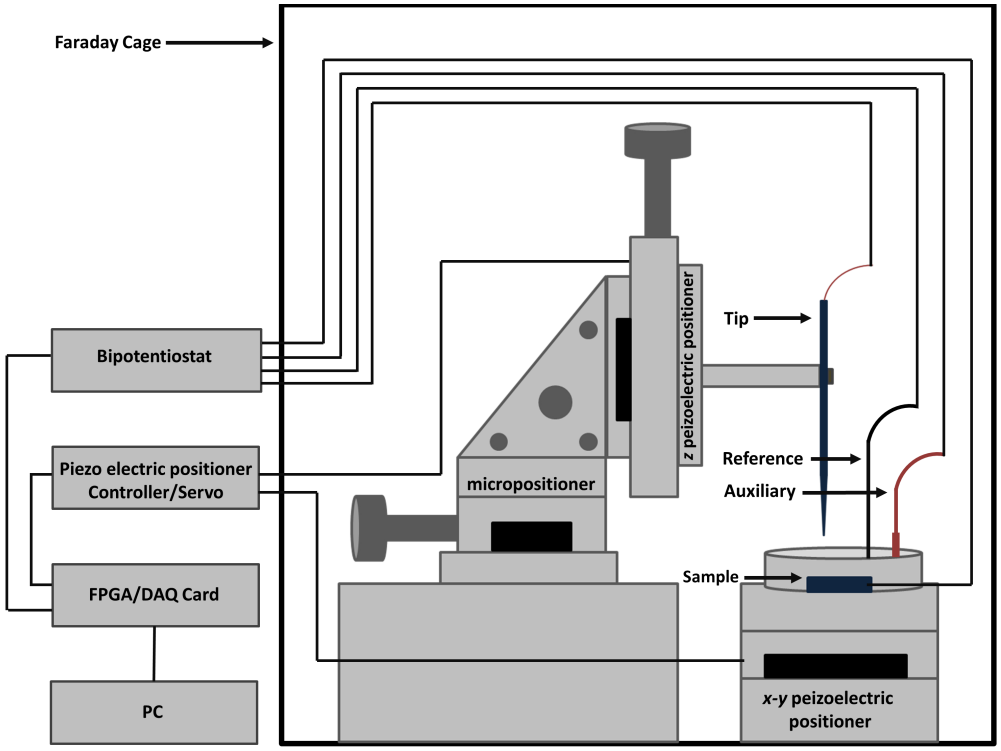

Figure 1.6: Schematic of a typical SECM set-up. The tip electrode is mounted onto a z piezoelectric-positioner for its vertical movement during an electrochemical scanning. The sample holder containing the substrate is mounted onto an x-y piezoelectric-positioner for the lateral movement. The entire system was mounted inside a Faraday cage. A bipotentiostat is generally used for controlling the potential (bias) of the tip and /or substrate during the experiment.The tip position, bias and the electrochemical currents were controlled and measured by using a personal computer through a data acquisition (DAQ) or a field-programmable gate array (FPGA) card

The tip electrode is mounted in a XYZ piezoelectric-positioner for the x, y

and z movement of the tip during electrochemical scanning. In some cases, two separate piezoelectric positioners, one for x-y movement of the sample holder and another for the z-translation of tip were also used. A bipotentiostat is generally used for controlling the potential (bias) of the tip and /or substrate during the experiment. The tip position, bias and the electrochemical currents were controlled and measured by using a personal computer through a data acquisition (DAQ) or a field-programmable gate array (FPGA) card.[5, 44]

SECM imaging of surfaces was achieved by scanning the tip laterally across the surfaces while monitoring the tip current as a function of the tip position. For this the tip is first positioned close to the surface by recording an approach curve to the surface. Traditionally two different schemes, namely the constant height mode and constant current mode were employed for SECM imaging.

In constant height mode, the tip is approached towards the substrate surface and a lateral scan is initiated after the tip is positioned at a fixed distance away from the surface. For a surface that has both conducting and insulating regions, the tip current recorded could vary depending on their conductivity and can be easily mapped by using this type of SECM imaging technique provided the surface is flat and well aligned with respect to the lateral plane in which the probes is moved. In case of rough or misaligned surfaces, as mentioned earlier, the variation in tip/surface separation during the scan can also contribute to the variation in the tip current adding uncertainty into the measurements.[1, 6, 7]

In constant current mode, after the initial approach, instead of scanning along a single plane at a constant height, the tip is moved across the sample while maintaining a constant current response and hence tip/surface separation assuming a uniform activity across the surface.[1, 19] However for samples with varying

reactivity, like the constant height mode, this method is ineffective in separating topology from reactivity.

This inability of SECM in separating the effects of topography and activity on the electrochemical measurements in SECM has motivated the development of various SECM configurations incorporating additional positioning methods, such as the alternating current SECM (AC-SECM), tip position modulation SECM (TPM-SECM), shear force SECM and intermittent contact SECM (IC-SECM).[1]

AC-SECM works by applying an alternating potential to the tip electrode which induces an alternating current (AC) component into the electrochemical current measured at the tip electrode.[45-50] Unlike the direct current (DC) component, which depends on the faradic current generated at the tip electrode, the AC component relies only on the ion movement between the tip electrode and the reference electrode in the bulk electrolyte solution. As the tip approaches the surface, the decrease in tip/surface separation hinders this ion movement, resulting in a decrease in the AC amplitude which can be used as the feedback signal to maintain a constant tip/surface separation while the tip is scanning across the surface. While AC-SECM requires the use of a function generator or lock-in amplifier, it can be easily implemented as it uses a standard UME as the tip electrode. However the use of AC-SECM as a vertical positioning technique is limited only to homogenously insulating or unbiased substrates (when a low alternating frequency and electrolyte concentration is used) since the AC signal can also be modulated by the local conductivity of the substrate surface. Nevertheless this technique was widely used for investigating cellular processes[47, 51] and corrosion studies.[46, 52-55]

In TPM-SECM, the position of tip is oscillated normal to the substrate surface by applying a sinusoidal signal into the z-piezo while the tip is scanned

over the surface.[56-58] As the tip approaches the surface, since the electrochemical current measured at the tip electrode depends on the tip/surface separation, the modulation in distance caused by the vertical oscillation of the tip induces an AC component in the tip current. The magnitude of this AC component depends on the tip/surface distance, i.e. the current increases over a conductive region while it decreases when the tip is over an insulating region, and the phase shows a 180° difference which can be used to control the tip/surface separation.

Shear force SECM uses the fluid damping effect or shear force for measuring and controlling the tip/surface distance. A shear force is induced when the tip is oscillated parallel to the substrate surface at very high frequency (in the order of hundreds of kilo hertz).[1, 36, 59-64] This shear force is independent of the electrochemical behaviour and hence can be successively employed for the precise control of the tip positioning during an SECM imaging. This was achieved by either using a vibrating needle tip electrode[62, 64-66] or by using a quartz crystal resonator for inducing the shear force,[67, 68] where the former is the most commonly employed method. In a typical shear force SECM scan, a flexible SECM tip is vibrated laterally using an excitation piezo at its resonant frequency and the vibrational motion of the tip was monitored by focusing a laser beam onto the vibrating tip and projecting the resulting diffraction pattern onto a split photodiode. As the tip approaches the sample surface, the increase in shear force induces a decrease in vibration amplitude. This damping in amplitude generally occurs when the tip is within a distance of 100 nm from the surface and is used as the feedback signal to maintain a constant tip/surface separation for recording a high resolution electrochemical map of surfaces[60] and was successfully employed to image single cells[64, 69-71] as well as immobilized enzymes[65, 72-75] along with investigation of crys-

tal dissolution[76] and patterned surfaces.[19] Even though the non- electrochemical nature of the feedback signal used in shear force SECM simplifies the analysis of electrochemical signal recoded at the tip electrode, the dependence of shear force on the hardness of the sample and the complexities in interpreting the feedback signal still remains a challenge towards the wider adoption of this technique.

In IC-SECM, the tip/surface separation was controlled by applying a small AC positional perturbation onto the z-piezoelectric positioner which controls the vertical positioning of the tip over the surface.[39] As the tip approaches the substrate surface, the amplitude of oscillation is observed to decrease at very close distances. This damping in oscillation is used as the feedback signal for maintaining a constant tip/surface separation during the SECM scan. For this, the tip is positioned at a distance at which a predefined value of damping is reached and a computer-controlled closed-loop feedback scheme was employed to continuously compare the actual value of the oscillation amplitude with the set point value, and respond rapidly to any resulting differences by readjusting the tip/surface separation using the z-piezoelectric positioner while the tip is laterally scanned over the substrate surface. IC-SECM has been widely used for the quantification of molecular transport through porous samples and for visualization of interfacial reaction and fluxes from surface to bulk solutions.[38, 39, 44, 77, 78]

Over the last two decades, SECM has been extensively used in a multitude of applications, notably for imaging various surfaces[19, 33, 79-83] and fabricating nanostructures on surfaces.[5, 19, 40, 84-89] As an imaging technique, SECM has been widely used in studying the structure and process on the nanoscale,[7, 8, 39, 82] especially in electrocatalysis to detect and image regions with different catalytic activities,[90-98] and in biological systems for imaging living cells,[99-103] to monitor respiration and

other cellular function,[77, 104-112] to study biological redox systems[28, 74, 83, 113-121] and to investigate transport of various molecules across biological membranes including planar lipid bilayer membranes and liposomes.[122-129] In addition to this, the SECM technique has been reported for investigating electron transfer kinetics at solid/liquid interfaces,[7, 130-136] charge transport across liquid/ liquid interfaces,[137-142] and lateral mass/ charge transfer across various interfaces.[35, 143-146]

The introduction of various nanofabrication methods for preparation of nanoscale tips along with the development of numerous hybrid techniques and advances in instrumentations have greatly enhanced the use of SECM towards solving many problems in cell biology, surface science and nanotechnology.[7, 8]

1.4 Scanning Ion Conductance Microscopy

Scanning Ion Conductance Microscopy (SICM) is a pipet based EC-SPM technique developed by Hansma[147] in 1989 to image nonconductive substrate surfaces immersed in an electrolyte solution.[1, 148] SICM employs a glass capillary pulled to a sharp point, usually with a sub-micrometer capillary opening (nanopipet) filled with an electrolyte solution and containing a reference electrode (typically a Ag/AgCl quasi-reference counter electrode) as the scanning probe for imaging surfaces.[149-155].

The general schematic of a typical SICM set-up is shown in Figure 1.7.[148, 156] The electrolyte filled nanopipet containing a Ag/AgCl quasi-reference counter electrode (QRCE) inserted, is placed in an electrolyte solution containing another Ag/AgCl QRCE, and a bias is applied between the QRCEs in the nanopipet and the bulk electrolyte solution to generate an ion current flow between the QRCEs

whose magnitude is highly dependent on the tip/surface separation. As the pipet

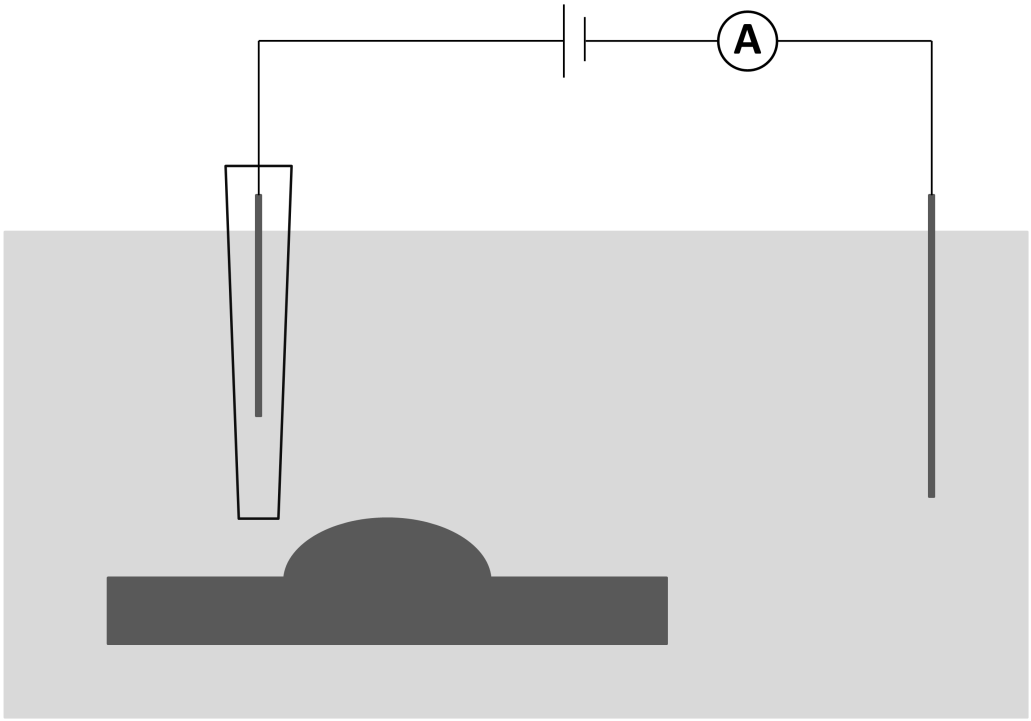

Figure 1.7: Schematic of a scanning ion conductance microscope. The electrolyte filled nanopipet containing a Ag/AgCl quasi-reference counter electrode (QRCE), is placed in an electrolyte solution containing another Ag/AgCl QRCE. A bias is applied between the QRCEs in the nanopipet and the bulk electrolyte solution to generate an ion current, which can be used for the feedback control.

approaches the substrate surface, the decreasing tip/surface separation impedes the ion flow and hence causes a rapid decrease in ion current which can be readily detected an monitored to maintain a constant tip/surface separation using a z-piezoelectric positioner while scanning over the sample surfaces.[148, 151, 157-160]

SICM has been widely used to image the topography of a variety of sample

surfaces including soft biological systems. Three different SICM scanning schemes,

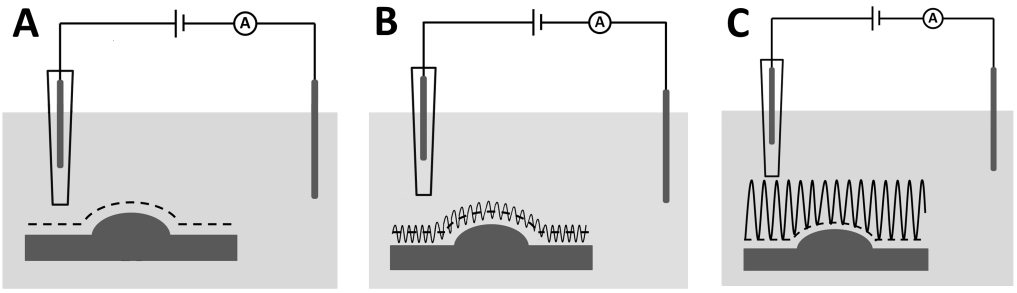

Figure 1.8: Schematic of nonmodulated (A), distance modulated (B) and hopping mode (C) scanning ion conductance microscopy.

namely the nonmodulated SICM (*DC* mode SICM),[147, 149, 161, 162] distance- modulated SICM[150, 152-155, 159, 160, 163, 164] and hopping mode SICM[148, 151, 164-166] were generally employed for acquiring images of surfaces along with the recently reported bias-modulated[156] and phase -modulated SICM.[167]

Nonmodulated SICM is the simplest SICM scanning procedure, where the probe is moved laterally across the sample using an ion current (DC) set-point to maintain a fixed tip/surface separation (Figure 1.8A). Even though SICM with nonmodulated feedback could provide adequate control over the tip/surface separation to image submicrometer features in the sample surfaces, it is less effective in imaging samples with large topographical features especially living cells. Also the response of DC feedback can be too slow and is susceptible to variations in ion current caused by partial blockage of the pipet, DC drift and changes in ionic strength of the electrolyte solution.

Distance-modulated SICM works by using an AC feedback control scheme.

For this the pipet is oscillated normal to the substrate surface by applying a sinusoidal signal into the z-piezo (Figure 1.8B). As the pipet approaches the surface, the oscillation of the pipet produces a modulation in tip/surface separation and hence a modulation in ion current which induces an AC component in the ion current that can be separated and measured by using a lock-in amplifier to use as the feedback signal. This AC component, unlike the ion current, is more surface sensitive and is independent of the changes in ion current that are not in phase with the modulation frequency and hence offers a more precise and stable feedback control during scanning. Distance-modulated SICM therefore could be employed for long-term continuous observation of living cell samples.[50, 168-175]

Hopping mode SICM is one of the most widely studied SICM scanning scheme which employs a series of approach curves for imaging the sample surfaces.[148] In hopping mode SICM, the pipet is approached to the surface to defined tip/surface separation using either AC or DC feedback, is withdrawn back to the bulk (to a predefined height), repositioned, and then approached to the surface again at the new location (Figure 1.8C). In this mode, the number of approaches (imaging points) determines both resolution and imaging time. Hopping mode SICM has been used to image samples with complex topographical structures including neurons and other biological systems.[151, 165, 176-181] Images obtained with the hopping mode have revealed nanoscale structures in the sample surface with minimum sample damage from the pipet, demonstrating the ability of this mode to image samples with extremely convoluted surfaces.[148, 153, 182-186]

Over the past decade, SICM has developed into a versatile non-invasive, high resolution imaging tool, largely due to the advances in feedback control systems and the introduction of various probe fabrication techniques. Further, the

introduction of various hybrid SICM techniques is extending the practical use of SICM into the fields of molecular biology for investigation of structure and properties of nucleic acids and proteins along with applications in cellular physiology and crystal dissolution.[148, 164]

1.5 Scanning Droplet Cell Microscopy

Scanning droplet cell microscopy uses a liquid droplet formed at the end of a pipet to assemble an electrochemical cell on the sample surface, and hence confine electrochemical reactions to the contact area between the droplet and the surface. Pipets used in these techniques typically have foot prints of several hundred micrometres defined by a silicone or rubber seal formed at the tip of the pipet and have been applied mainly to study the mechanism and kinetics of metal corrosion.[187-195]

In scanning droplet cell microscopy the sample surface wetted by the meniscus acts as a working electrode where the electrochemical activity can be measured.[188-190,196,197] However, by incorporating further working electrodes into the end of the probe it is possible enhance the capability these type of techniques. Fountain pen probes, incorporating a microfluidic channel with integrated working and counter/reference electrodes, employ just such a scheme.[1, 23, 33] The built-in microfluidic channel aids the assembly of an electrolyte droplet and electrochemical reactions are performed in the droplet by means of the working electrode in the tip of the probe. The working electrode in the droplet is used in a feedback mode to probe the local electrochemical responses of the substrate in contact with the droplet. Microfluidic push-pull probes, similar to the fountain pen probe but

containing two microfluidic channels for delivery and aspiration of the electrolyte solution, also incorporating a working electrode directly into the droplet at the end of the probe were also reported for performing scanning electrochemical measurements in a constantly renewed electrolyte droplet.[24, 198] However the use of these probes are limited to investigation of larger sample surfaces due to their large foot print.

The introduction of the scanning micropipet contact method and scanning electrochemical cell microscopy extended the use of scanning droplet cell microscopy in to nanoscale electrochemical characterization of materials and enabled the simultaneous electrochemical and topography imaging of surfaces and interfaces.

1.5.1 Scanning Micropipet Contact Method

Scanning micropipet contact method (SMCM) was developed [199]to investigate the mechanism and kinetics of electrochemical reactions at pristine electrode surfaces with high spatial resolution. In SMCM, a liquid droplet formed at the end of a micro or nanopipet filled with an electrolyte containing the electroactive species, was used as a positionable electrochemical cell for performing electrochemical measurements.

In a typical SMCM set-up, an Ag/AgCl QRCE inserted into the pipet acts as the reference electrode and the substrate surface wetted by the meniscus acts as a working electrode where the electrochemical current is measured. SMCM imaging was performed by operating the pipet in a hopping mode. For this, the pipet was approached toward the substrate surface and approach was paused upon the

contact of the droplet with the substrate (detected as a current flow), a steady-state current value or a currentvoltage curve was then recorded and the pipet was withdrawn back to a predefined height and repositioned, before approaching to the surface again at the new location.[199-201] The implementation of the hopping mode in SMCM enabled images of reactivity to be built up across the substrate of interest and the simplified probe design allowed precise control of the droplet contact area with high reproducibility. SMCM has been successfully employed for the electrochemical interrogation of redox activity at highly oriented pyrolytic graphite (HOPG), investigations of heterogeneities in the electroactivity of aluminium alloys[199] and more recently for voltammetric studies at single-walled carbon nanotubes (SWNTs) and metal nanowires.[202-204]

1.5.2 Scanning Electrochemical cell Microscopy

Scanning electrochemical cell microscopy (SECCM) is a recently introduced EC-SPM technique[190, 196, 205] which builds on the idea of using a nanoscale liquid droplet formed at the end of a dual barrel (theta) pipet[206] for localized electrochemical measurements at pristine surfaces.

SECCM employs a dual barrel pipet with sub-micrometer tip diameter as the scanning probe. A schematic of a typical SECCM experimental set-up is shown in Figure 1.9. These SECCM probes are fabricated from either borosilicate or quartz double-barrel pipets, pulled into a sharp point using a laser puller. The size of the probe can be controlled by adjusting the pulling parameters, with probes with tip diameters between 50 nm and tens of micrometers across at the tip ends fabricated easily and quickly. The pipet barrels were filled using an electrolyte

solution containing an electroactive species of interest.

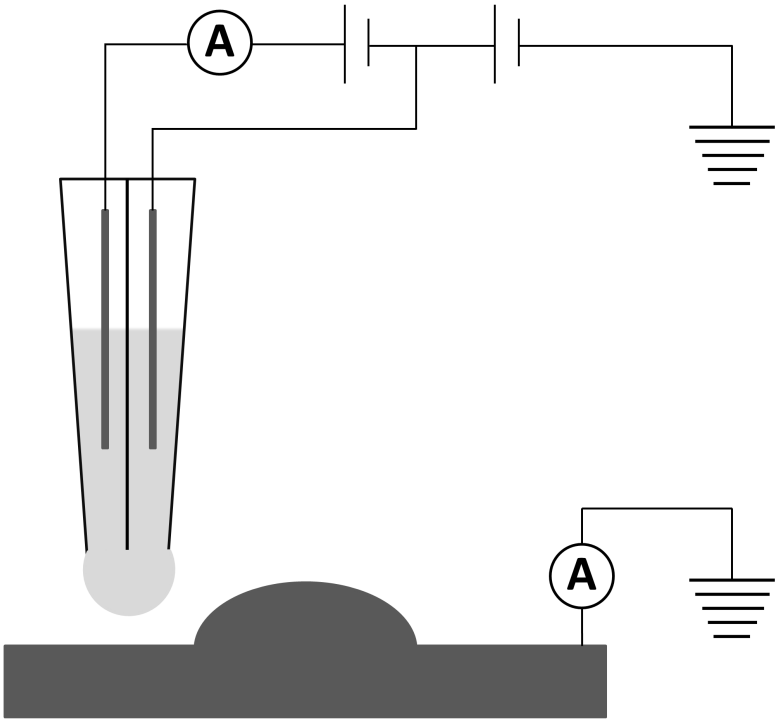

Figure 1.9: Illustration of scanning electrochemical cell microscopy (SECCM) operation. Typically a bias is applied between the QRCEs in the electrolyte filled pipet barrels to induce an ion current flow across the droplet formed at the pipet tip which is used as the feedback signal for droplet positioning during SECCM imaging. Simultaneously, the potentials of the QRCEs with respect to a (semi)conducting substrate surface can be varied to drive electrochemical reactions at the substrate which can then be measured while the droplet is scanning across the surface to generate surface activity maps.

A liquid droplet meniscus naturally forms at the tip of the pipet connecting the two barrels whose size determined by the tip diameter of the pipet. QRCEs (typically Ag/AgCl QRCEs) are then inserted into each barrel, and a bias is applied between the QRCEs to induce an ion current flow across the droplet. The magnitude of this conductance current depends on the size and shape of the liq-

uid droplet and therefore when this droplet deforms, as is the case when it comes into contact with the substrate surface, a change in ionic current results which can be measured and used as the feedback signal for droplet positioning during SECCM imaging.[196] Simultaneously, the potentials of the QRCEs with respect to a (semi)conducting substrate surface can be varied to drive electrochemical reactions at the substrate which can then be measured while the droplet is scanning across the surface to generate surface activity maps. To increase the sensitivity of the feedback signal, a probe modulation scheme has also been used where in the pipet is oscillated normal to the surface which induces an AC component in the ion current when the droplet is in contact with the surface. This AC component can be measured by using a lock-in amplifier and can be used as the feedback signal. Two dimensional electrochemical images of the substrate surfaces were constructed from a series of line scans, during which the probe was moved laterally, while a constant AC magnitude was maintained using a feedback loop and thus a constant tip/surface separation.

Ever since its inception, SECCM was employed to study the electrochemical properties of a range of electrode materials ranging from graphene[207-210] to polycrystalline platinum[211-214] to SWNTs[215-218] with nanoscale resolution. More recently SECCM was reported for electrochemical patterning[219] and surface modifications of electrode materials[208, 220, 221] and for crystal dissolution studies.[222, 223] The capability of SECCM can further be enhanced by incorporating additional working electrodes into the end of the SECCM probe. Chapters 5 and 6 report on the fabrication characterization and use of an SECCM probe incorporating carbon working electrodes for voltammetric analysis and imaging of sample substrates and electrochemical single molecule detection.

1.6 Hybrid EC-SPM Techniques

Whilst each EC-SPM technique is a powerful tool in itself, their capabilities can be further enhanced either by combining them with other complimentary techniques such as atomic force microscopy and confocal laser scanning microscopy or by combing two different EC-SPM techniques.[1] Taking this concept one step further, variants of SECM, including SECM-SICM,[224] SECM-confocal laser scanning microscopy,[122] SECM-atomic force microscopy[225] etc. were reported to add positional feedback mechanisms to conventional SECM and/or to allow fundamental aspects of electrochemical interfaces to be probed.

1.6.1 SECM-SICM

The combination of SICM and SECM into a single platform enabled the simultaneous determination of topography and electrochemical activity of surfaces and interfaces. This was achieved by fabricating tip electrodes (probes) that have dual functionalities. The most commonly used SECM-SICM probes are fabricated, either as a ring electrode that surrounds an open barrel that forms the SICM channel,[224] or as a dual barrel probe with an electrode formed in one barrel while the other open barrel forms the SICM channel.[153, 164, 215, 226] The former is fabricated from a laser pulled glass pipet by coating a layer of gold around the tip and covering it with an insulating layer and exposing the aperture of the tip by using focussed ion beam milling. The latter is fabricated by using a much simpler method where one of the barrels of a laser pulled dual barrel pipet was filled with amorphous carbon by pyrolytic decomposition of butane.

SECM-SICM imaging of sample surfaces was performed either by using an

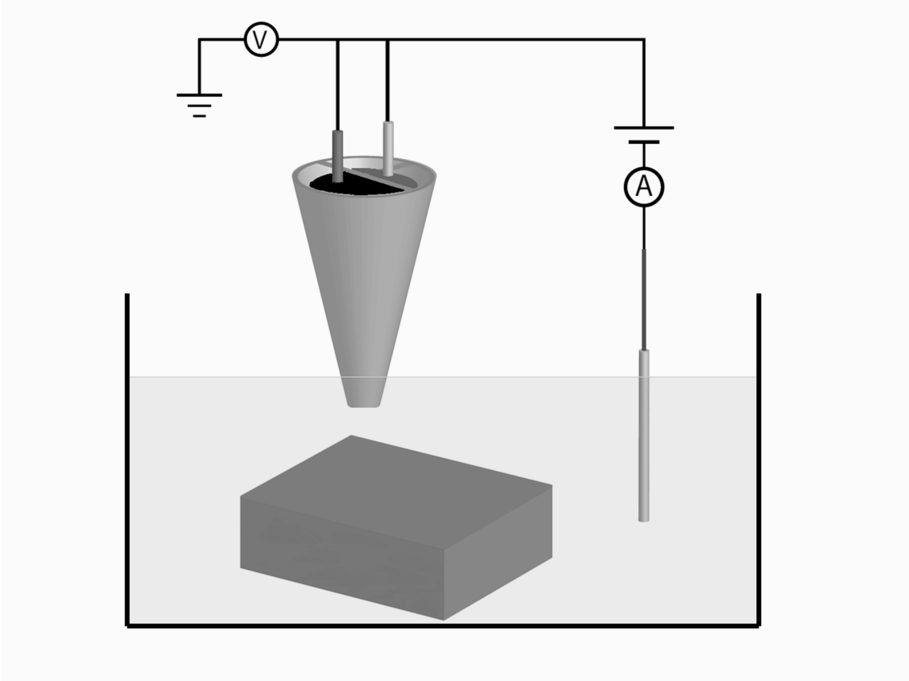

Figure 1.10: Schematic of SECM-SICM. The SICM channel of the probe is filled with an electrolyte solution and a bias is applied between the Ag/AgCl QRCE inserted into the SICM channel of the probe and the Ag/AgCl QRCE positioned in the bulk electrolyte solution. Simultaneously, the potentials of the SECM electrode in the probe with respect to the QRCE in the bulk solution is varied to drive electrochemical reactions at the probe electrode which can then be measured.

SICM hopping mode scheme discussed earlier (section 1.4) or by using a constant separation scheme similar to that of SECCM, where either the DC or AC component of the ionic current is used for maintaining a constant tip/surface separation. In both the cases, the SICM channel of the probe was filled with an electrolyte solution and a bias is applied between the Ag/AgCl QRCE inserted into the SICM channel of the probe and the Ag/AgCl QRCE positioned in the bulk electrolyte solution. Simultaneously, the potentials of the SECM electrode in the probe with respect to the QRCE in the bulk solution is varied to drive electrochemical re-

actions at the probe electrode which can then be measured while the droplet is scanning across the surface to generate surface activity maps.[227]

SECM-SICM offers a flexible hybrid electrochemical imaging technique which makes it easy to further extend the capability of this technique to functional imaging and has been employed for imaging the topography and corresponding electrochemical responses for gold band substrate,[153, 224, 228-230] and living cells.[153, 183, 224, 231-233] Chapter 4 of this thesis describes a combined pH-SICM technique developed to record simultaneous pH and topography maps of dynamic surfaces with high spatial resolution.

1.6.2 SECM-Confocal Laser Scanning Microscopy

SECM-confocal laser scanning microscopy (SECM-CLSM) enables simultaneous electrochemical and optical imaging of surfaces and interfaces.[234] In its simplest form, the SECM-CLSM consists of a typical SECM set-up mounted onto a CLSM. While the SECM enables the positioning of a tip electrode close to the surface or interface of interest to induce an electrochemical reaction, the CLSM allows high resolution optical imaging of the reaction products or intermediates with the aid of a suitable fluorophore molecule.

SECM-CLSM was reported previously for quantifying the three-dimensional pH diffusion gradient generated at a tip electrode in solution[235, 236] and for quantitatively measuring the permeation coefficients of week acids across lipid bilayer membranes[122] using a pH sensitive fluorophore. SECM-CLSM was also used for activity mapping of various patterned biomolecules.[75, 237] Chapter 7 of this thesis describes the use of a hybrid CLSM/EC-SPM technique for investigation of passive

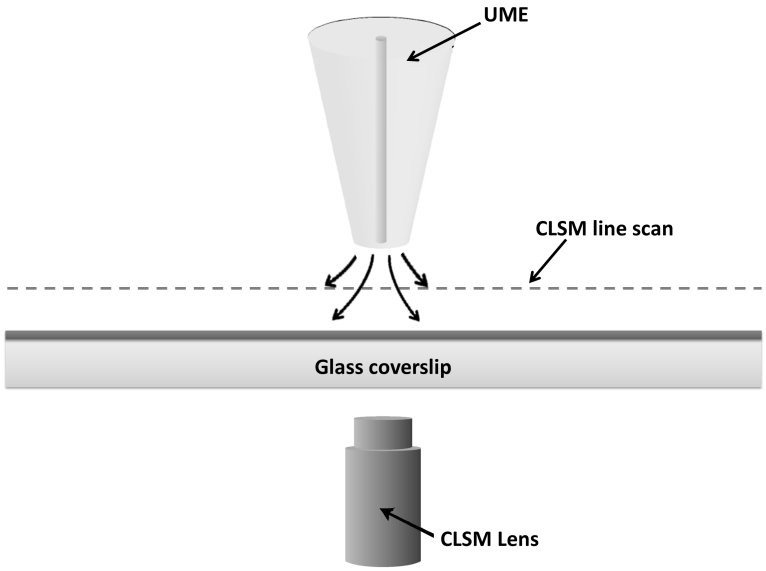

Figure 1.11: Schematic of SECM-CLSM. While the SECM enables the positioning of a tip electrode close to the surface or interface of interest to induce an electrochemical reaction, the CLSM allows high resolution optical imaging of the reaction products or intermediates with the aid of a suitable fluorophore molecule.

permeation of weak acids across lipid bilayer membranes.

1.7 Aim of this Thesis

The aim of this thesis is to develop new electrochemical methods for visualizing interfacial ion fluxes using different EC-SPM techniques. These EC-SPM based methods were developed to (i) to improve the spatial resolution of SECM by incorporating inexpensive nanoelectrode systems, (ii) to advance combined SECM-SICM from amperometry/voltammetry to potentiometric imaging by using dual

functional nanoprobes, (iii) to adapt SECCM for multifunctional electrochemical imaging of surfaces and interfaces and for localized investigation of electrochemical processes at pristine surfaces (both conducting and insulating), (iv) to extend the use of SECCM for electrochemical detection of single entities, and (v) to further the capabilities of SECM-CLSM to quantify passive permeation of molecules across biological membranes.

Different electrochemical methods employing unique electrode systems were developed and tested to address this objective. An attractive feature of these methods is that they are very well-defined and amenable to precise modelling of mass transport/reactivity. This was accomplished by using finite element modelling.

Chapter 3 describes the development of a nanoscale dual carbon electrode and it's use in visualization and quantification of photosynthetic electron transport at thylakoid membranes. The possibility of using the developed nanoscale dual carbon electrode for electrochemical sensing was also explored in this chapter.

Chapter 4 introduces an extremely quick and simple method to fabricate a hybrid pH-SICM probe. This advances the existing SECM-SICM capability from amperometry/voltammetry to potentiometric imaging. Further the capability of these probes for high resolution quantitative pH mapping on topographically challenging interfaces were also demonstrated.

A new multifunctional electrochemical and ion conductance probe combining the capabilities of both SECM and SECCM for voltammetric analysis and electrochemical imaging was reported in chapter 5.

Chapter 6 presents a powerful new approach for the measurement of single molecule electrochemistry using a pipet probe cell. This an application of the multifunctional probe described in chapter 5.

Chapter 7 describes the use of a hybrid CLSM/EC-SPM technique for visualization and quantification of permeation of week acids across lipid bilayer membranes.

Chapter 8 provides a brief conclusion of the thesis.

1.8 References

[1] Bard, A. J., Mirkin, M. V., *Scanning electrochemical microscopy*, CRC Press, Boca Raton, FL. 2012.

[2] Bard, A. J., Faulkner, L. R., *Electrochemical Methods: Fundamentals and Applications*, Wiley 2000.

[3] Brett, C. M. A., Brett, A. M. O., *Electrochemistry: Principles, Methods, and Applications*, Oxford University Press 1993.

[4] Fisher, A. C., *Electrode Dynamics*, Oxford University Press 1996.

[5] Bard, A. J., Fan, F. R. F., Kwak, J., Lev, O., *Anal. Chem.* **1989**, 61.

[6] Amemiya, S., Bard, A. J., Fan, F.-R. F., Mirkin, M. V., Unwin, P. R., *Annu. Rev. Anal. Chem.*. **2008**, 1, 95-131.

[7] Sun, P., Laforge, F. O., Mirkin, M. V., *Phys. Chem. Chem. Phys.* **2007**, 9, 802-823.

[8] Mirkin, M. V., Nogala, W., Velmurugan, J., Wang, Y., *Phys. Chem. Chem. Phys.* **2011**, 13, 21196-21212.

[9] Fleischmann, M., *Ultramicrolectrodes*, Datatech Systems 1987.

[10] Bard, A. J., Zoski, C. G., *Electroanalytical Chemistry: a Series of Advances*, Vol 24 2012.

[11] Lee, C., Miller, C. J., Bard, A. J., *Anal. Chem.* **1991**, 63, 78-83.

[12] Pendley, B. D., Abruna, H. D., *Anal. Chem.* **1989**, 62, 782-784.

[13] Ramirez-Garcia, S., Alegret, S., Cespedes, F., Forster, R. J., *Anal. Chem.* **2004**, 76, 503-512.

[14] Marken, F., Gerrard, M. L., Mellor, I. M., Mortimer, R. J., Madden, C. E., Fletcher, S., Holt, K., Foord, J. S., Dahm, R. H., Page, F., *Electrochem. Commun.*

2001, 3, 177-180.

[15] Zhang, M., Liu, K., Xiang, L., Lin, Y., Su, L., Mao, L., *Anal. Chem.* **2007**, 79, 6559-6565.

[16] Edmonds, T. E., *Anal. Chim. Acta* 1985, 175, 1-22.

[17] Wipf, D. O., Ge, F. Y., Spaine, T. W., Bauer, J. E., *Anal. Chem.* **2000**, 72.

[18] Zhang, X. J., Ogorevc, B., Wang, J., *Anal. Chim. Acta* **2002**, 452.

[19] Bard, A. J., Denuault, G., Lee, C., Mandler, D., Wipf, D. O., *Acc. Chem. Res.* **1990**, 23, 357-363.

[20] Heinze, J., *Angew. Chem., Int. Ed. Engl.* **1993**, 32, 1268-1288.

[21] Silva, S. M., Alves, C. R., Correia, A. N., Martins, R. M., Nobre, A. L. R., Machado, S. A. S., Mazo, L. H., Avaca, L. A., *Quim. Nova* **1998**, 21, 78-85.

[22] McKelvey, K., Nadappuram, B. P., Actis, P., Takahashi, Y., Korchev, Y. E., Matsue, T., Robinson, C., Unwin, P. R., *Anal. Chem.* **2013**, 85, 7519-7526.

[23] Cortes-Salazar, F., Lesch, A., Momotenko, D., Busnel, J.-M., Wittstock, G., Girault, H. H., *Anal. Methods* **2010**, 2, 817-823.

[24] Momotenko, D., Cortes-Salazar, F., Lesch, A., Wittstock, G., Girault, H. H., *Anal. Chem.* **2011**, 83, 5275-5282.

[25] Lee, C., Wipf, D. O., Bard, A. J., Bartels, K., Bovik, A. C., *Anal. Chem.* **1991**, 63, 2442-2447.

[26] Bard, A. J., Mirkin, M. V., Unwin, P. R., Wipf, D. O., *J. Phys. Chem.* **1992**, 96, 1861-1868.

[27] Pierce, D. T., Bard, A. J., *Anal. Chem.* **1993**, 65, 3598-3604.

[28] Horrocks, B. R., Schmidtke, D., Heller, A., Bard, A. J., *Anal. Chem.* **1993**, 65, 3605-3614.

[29] Wei, C., Bard, A. J., Kapui, I., Nagy, G., Toth, K., *Anal. Chem.* **1996**, 68,

2651-2655.

[30] Mauzeroll, J., Bard, A. J., *Proc. Natl. Acad. Sci. U. S. A.* **2004**, 101, 7862-7867.

[31] Tsionsky, M., Zhou, J. F., Amemiya, S., Fan, F. R. F., Bard, A. J., Dryfe, R. A. W., *Anal. Chem.* **1999**, 71, 4300-4305.

[32] Amemiya, S., Bard, A. J., *Anal. Chem.* **2000**, 72, 4940-4948.

[33] Cortes-Salazar, F., Momotenko, D., Girault, H. H., Lesch, A., Wittstock, G., *Anal. Chem.* **2011**, 83, 1493-1499.

[34] Calhoun, R. L., Bard, A. J., in: Minteer, S. (Ed.), *Grahame Award Symposium and Physical and Analytical Electrochemistry* **2011**, pp. 39-51.

[35] Zhang, J., Unwin, P. R., *Phys. Chem. Chem. Phys.* **2002**, 4, 3814-3819.

[36] Ludwig, M., Kranz, C., Schuhmann, W., Gaub, H. E., *Rev. Sci. Instrum.***1995**, 66, 2857-2860.

[37] Lee, C., Kwak, J. Y., Anson, F. C., *Anal. Chem.* **1991**, 63, 1501-1504.

[38] McKelvey, K., Nadappuram, B. P., Actis, P., Takahashi, Y., Korchev, Y. E., Matsue, T., Robinson, C., Unwin, P. R., *Anal. Chem.* **2013**, 85, 7519-7526.

[39] Lazenby, R. A., McKelvey, K., Peruffo, M., Baghdadi, M., Unwin, P. R., J. *Solid State Electrochem.* **2013**, 17, 2979-2987.

[40] Zoski, C. G., Aguilar, J. C., Bard, A. J., *Anal. Chem.*. **2003**, 75, 2959-2966.

[41] Cannan, S., Zhang, J., Grunfeld, F., Unwin, P. R., *Langmuir* **2004**, 20, 701-707.

[42] Gonsalves, M., Barker, A. L., Macpherson, J. V., Unwin, P. R., O'Hare, D., Winlove, C. P., *Biophys. J.* 2000, 78, 1578-1588.

[43] Edwards, M. A., Martin, S., Whitworth, A. L., Macpherson, J. V., Unwin, P. R., *Physiol. Meas.* **2006**, 27, R63-R108.

[44] Lazenby, R. A., McKevey, K., Unwin, P. R., *Anal. Chem.* **2013**, 85, 2937-2944.

[45] Eckhard, K., Schuhmann, W., *Analyst* **2008**, 133, 1486-1497.

[46] Wang, W., Xu, L., Sun, H., Li, X., Zhao, S., Zhang, W., *J. Mater. Chem. A* 2015, 3, 5599-5607.

[47] Diakowski, P. M., Ding, Z., *Phys. Chem. Chem. Phys.* **2007**, 9, 5966-5974.

[48] Diakowski, P. M., Ding, Z., *Electrochem. Commun.* **2007**, 9, 2617-2621.

[49] Baranski, A. S., Diakowski, P. M., *J. Solid State Electrochem.* **2004**, 8, 683-692.

[50] Koch, J. A., Baur, M. B., Woodall, E. L., Baur, J. E., *Anal. Chem.* **2012**, 84, 9537-9543.

[51] Kurulugama, R. T., Wipf, D. O., Takacs, S. A., Pongmayteegul, S., Garris, P. A., Baur, J. E., *Anal. Chem.* **2005**, 77, 1111-1117.

[52] Belger, S., Schulte, A., Hessing, C., Pohl, M., Schuhmann, W., *Materialwiss. Werkstofftech.* **2004**, 35, 276-279.

[53] Paehler, M., Santana, J. J., Schuhmann, W., Souto, R. M., *Chem. - Eur. J.***2011**, 17, 905-911.

[54] Eckhard, K., Etienne, M., Schulte, A., Schuhmann, W., *Electrochem. Commun.* **2007**, 9, 1793-1797.

[55] Eckhard, K., Erichsen, T., Stratmann, M., Schuhmann, W., *Chem. - Eur. J.***2008**, 14, 3968-3976.

[56] Wipf, D. O., Bard, A. J., *Anal. Chem.* **1992**, 64, 1362-1367.

[57] Edwards, M. A., Whitworth, A. L., Unwin, P. R., *Anal. Chem.* 2011, 83, 1977-1984.

[58] Cougnon, C., Bauer-Espindola, K., Fabre, D. S., Mauzeroll, J., *Anal. Chem.*

2009, 81, 3654-3659.

[59] Nebel, M., Eckhard, K., Erichsen, T., Schulte, A., Schuhmann, W., *Anal. Chem.* **2010**, 82, 7842-7848.

[60] Katemann, B. B., Schulte, A., Schuhmann, W., *Chem. - Eur. J.***2003**, 9, 2025-2033.

[61] Schuhmann, W., Schulte, A., Etienne, M., Turcu, F., Fritsch, I., *Abstr. Pap. Am. Chem. S.* **2003**, 226, U132-U132.

[62] Katemann, B. B., Schulte, A., Schuhmann, W., *Electroanalysis* **2004**, 16, 60-65.

[63] Etienne, M., Anderson, E. C., Evans, S. R., Schuhmann, W., Fritsch, I., *Anal. Chem.* **2006**, 78, 7317-7324.

[64] Michael, A., C., Borland, L. M., *Electrochemical Methods for Neuroscience*, CRC Press, Boca Raton FL. **2007**.

[65] Hengstenberg, A., Kranz, C., Schuhmann, W., *Chem. - Eur. J.***2000**, 6, 1547-1554.

[66] Clausmeyer, J., Actis, P., Cordoba, A. L., Korchev, Y., Schuhmann, W., *Electrochem. Commun.* **2014**, 40, 28-30.

[67] Karrai, K., Grober, R. D., Appl. Phys. Lett. **1995**, 66, 1842-1844.

[68] James, P. I., Garfias-Mesias, L. F., Moyer, P. J., Smyrl, W. H., *J. Electrochem. Soc.* **1998**, 145, L64-L66.

[69] Hengstenberg, A., Blochl, A., Dietzel, I. D., Schuhmann, W., *Angew. Chem., Int. Ed.* **2001**, 40, 905-908.

[70] Michael, C. P., *Imaging and Spectroscopic Analysis of Living Cells: Optical and Spectroscopic Techniques*, Academic Press, 2012.

[71] Takahashi, Y., Shiku, H., Murata, T., Yasukawa, T., Matsue, T., *Anal. Chem.*

2009, 81, 9674-9681.

[72] Yamada, H., Haraguchi, D., Yasunaga, K., *Anal. Chem.* **2014**, 86, 8547-8552.

[73] Garay, M. F., Ufheil, J., Borgwarth, K., Heinze, J., *Phys. Chem. Chem. Phys.* **2004**, 6, 4028-4033.

[74] Hirano, Y., Yasukawa, T., Mase, Y., Oyamatsu, D., Shiku, H., Mizutani, F., Matsue, T., *Electrochemistry* **2012**, 80, 30-32.

[75] Oyamatsu, D., Hirano, Y., Kanaya, N., Mase, Y., Nishizawa, M., Matsue, T., *Bioelectrochemistry* **2003**, 60, 115-121.

[76] Etienne, M., Schulte, A., Mann, S., Jordan, G., Dietzel, L. D., Schuhmann, W., *Anal. Chem.* **2004**, 76, 3682-3688.

[77] McKelvey, K., Martin, S., Robinson, C., Unwin, P. R., *J. Phys. Chem. B* **2013**, 117, 7878-7888.

[78] McGeouch, C.-A., Peruffo, M., Edwards, M. A., Bindley, L. A., Lazenby, R. A., Mbogoro, M. M., McKelvey, K., Unwin, P. R., *J. Phys. Chem. C* **2012**, 116.

[79] Lee, C. M., Kwak, J. Y., Bard, A. J., *Proc. Natl. Acad. Sci. U. S. A.* **1990**, 87, 1740-1743.

[80] Lee, C., Anson, F. C., *Anal. Chem.* **1992**, 64, 528-533.

[81] Wittstock, G., Yu, K. J., Halsall, H. B., Ridgway, T. H., Heineman, W. R., *Anal. Chem.* **1995**, 67, 3578-3582.

[82] Laforge, F. O., Velmurugan, J., Wang, Y., Mirkin, M. V., *Anal. Chem.* **2009**, 81, 3143-3150.

[83] Bard, A. J., Fan, F. R. F., Pierce, D. T., Unwin, P. R., Wipf, D. O., Zhou, F. M., *Science* **1991**, 254, 68-74.

[84] McCarley, R. L., Hendricks, S. A., Bard, A. J., *J. Phys. Chem.* **1992**, 96, 10089-10092.

[85] Shiku, H., Takeda, T., Yamada, H., Matsue, T., Uchida, I., *Anal. Chem.* **1995**, 67, 312-317.

[86] Husser, O. E., Craston, D. H., Bard, A. J., *J. Electrochem. Soc.* **1988**, 135, C393-C394.

[87] Adenier, A., Combellas, C., Kanoufi, F., Pinson, J., Podvorica, F. I., *Chem. Mater.* **2006**, 18, 2021-2029.

[88] Combellas, C., Kanoufi, F., Mazouzi, D., Journal of Electro*Anal. Chem.* **2006**, 589, 243-248.

[89] Borgwarth, K., Ricken, C., Ebling, D. G., Heinze, *Phys. Chem. Chem. Phys.* **1995**, 99, 1421-1426.

[90] Horrocks, B. R., Mirkin, M. V., Bard, A. J., *J. Phys. Chem.* **1994**, 98, 9106-9114.

[91] Jayaraman, S., Hillier, A. C., *Meas. Sci. Technol.* **2005**, 16, 5-13.

[92] Jeon, I. C., Anson, F. C., *Anal. Chem.* **1992**, 64, 2021-2028.

[93] Zhou, J. F., Zu, Y. B., Bard, A. J., *J. Electroanal. Chem.* **2000**, 491, 22-29.

[94] Fernandez, J. L., Hurth, C., Bard, A. J., *J. Phys. Chem. B* 2005, 109, 9532-9539.

[95] Casillas, N., Charlebois, S. J., Smyrl, W. H., White, H. S., *J. Electrochem. Soc.* **1993**, 140, L142-L145.

[96] Sugimura, H., Shimo, N., Kitamura, N., Masuhara, H., Itaya, K., *J. Electroanal. Chem.* **1993**, 346, 147-160.

[97] Wipf, D. O., Bard, A. J., *J. Electrochem. Soc.* **1991**, 138, L4-L6.

[98] Selzer, Y., Turyan, I., Mandler, D., *J. Phys. Chem.* B **1999**, 103, 1509-1517.

[99] Yasukawa, T., Kaya, T., Matsue, T., *Electroanalysis* **2000**, 12, 653-659.

[100] Bergner, S., Vatsyayan, P., Matysik, F.-M., *Anal. Chim. Acta* **2013**, 775,

1-13.

[101] Razzaghi, F., Seguin, J., Amar, A., Griveau, S., Bedioui, F., *Electrochim. Acta* **2015**, 157, 95-100.

[102] Roberts, W. S., Lonsdale, D. J., Griffiths, J., Higson, S. P. J., *Biosens. Bioelectron.* **2007**, 23, 301-318.

[103] Amemiya, S., Guo, J., Xiong, H., Gross, D. A., Anal. *Bioanal. Chem.* **2006**, 386, 458-471.

[104] Chen, K. S., Hirst, J., Camba, R., Bonagura, C. A., Stout, C. D., Burgess, B. K., Armstrong, F. A., *Nature* **2000**, 405, 814-817.

[105] Kaya, T., Numai, D., Nagamine, K., Aoyagi, S., Shiku, H., Matsue, T., *Analyst* **2004**, 129, 529-534.

[106] Shiku, H., Shiraishi, T., Aoyagi, S., Utsumi, Y., Matsudaira, M., Abe, H., Hoshi, H., Kasai, S., Ohya, H., Matsue, T., *Anal. Chim. Acta* **2004**, 522, 51-58.

[107] Kaya, T., Torisawa, Y. S., Oyamatsu, D., Nishizawa, M., Matsue, T., *Biosens. Bioelectron.* **2003**, 18, 1379-1383.

[108] Skiku, H., Shiraishi, T., Ohya, H., Matsue, T., Abe, H., Hoshi, H., Kobayashi, M., *Electrochemistry* **2000**, 68, 890-892.

[109] Takii, Y., Takoh, K., Nishizawa, M., Matsue, T., *Electrochim. Acta* **2003**, 48, 3381-3385.

[110] Hirano, Y., Kodama, M., Shibuya, M., Maki, Y., Komatsu, Y., *Anal. Biochem.* **2014**, 447, 39-42.

[111] Abe, H., Yokoo, M., Itoh-Sasaki, T., Nasu, M., Goto, K., Kumasako, Y., Araki, Y., Shik, H., Matsue, T., Utsunomiya, T., *Proc. Int. Forum Post-Genome Technol.* **2007**, 5, 1-6.,

[112] Nebel, M., Gruetzke, S., Diab, N., Schulte, A., Schuhmann, W., *Angew.*

Chem., Int. Ed. **2013**, 52, 6335-6338.

[113] Pierce, D. T., Unwin, P. R., Bard, A. J., *Anal. Chem.* **1992**, 64, 1795-1804.

[114] Zhao, X., Zhang, M., Long, Y., Ding, Z., *Can. J. Chem.* **2010**, 88, 569-576.

[115] Niculescu, M., Gaspar, S., Schulte, A., Csoregi, E., Schuhmann, W., *Biosens. Bioelectron.* **2004**, 19, 1175-1184.

[116] Li, X., Geng, Q., Wang, Y., Si, Z., Jiang, W., Zhang, X., Jin, W., *Electrochim. Acta* **2007**, 53, 2016-2024.

[117] Burchardt, M., Wittstock, G., *Bioelectrochemistry* **2008**, 72, 66-76.

[118] Nogala, W., Szot, K., Burchardt, M., Joensson-Niedziolka, M., Rogalski, J., Wittstock, G., Opallo, M., *Bioelectrochemistry* **2010**, 79, 101-107.

[119] Kueng, A., Kranz, C., Mizaikoff, B., Biosens. *Bioelectron.* **2005**, 21, 346-353.

[120] Ge, F. Y., Tenent, R. C., Wipf, D. O., *Anal. Sci.* **2001**, 17, 27-35.

[121] Gao, N., Wang, X., Li, L., Zhang, X., Jin, W., *Analyst* **2007**, 132, 1139-1146.

[122] Grime, J., Edwards, M. A., Rudd, N. C., Unwin, P. R., *Proc. Natl. Acad. Sci. U. S. A.* **2008**, 105, 14277.

[123] Matsue, T., Shiku, H., Yamada, H., Uchida, I., *J. Phys. Chem.* **1994**, 98, 11001-11003.

[124] Kim, J., Izadyar, A., Nioradze, N., Amemiya, S., *J. Am. Chem. Soc.* **2013**, 135, 2321-2329.

[125] Slevin, C. J., Liljeroth, P., Kontturi, K., *Langmuir* **2003**, 19, 2851-2858.

[126] Hueske, E. A., Bard, A. J., *Abstr. Pap. Am. Chem. S.* **2001**, 221, U216-U217.

[127] Li, J., Jia, X., Yan, Y., Zhang, X., *Int. J. Electrochem. Sci.* **2011**, 6, 1216-1229.

[128] Guo, J. D., Amemiya, S., *Anal. Chem.* **2005**, 77, 2147-2156.

[129] Wilburn, J. P., Wright, D. W., Cliffel, D. E., *Analyst* **2006**, 131, 311-316.

[130] Wang, Y., Kececi, K., Velmurugan, J., Mirkin, M. V., *Chem. Sci.* **2013**, 4, 3606-3616.

[131] Zhang, B., Xu, X., Zhang, X., Huang, D., Li, S., Zhang, Y., Zhan, F., Deng, M., He, Y., Chen, W., Shen, Y., Wang, M., *Chemphyschem* **2014**, 15, 1182-1189.

[132] Lu, X., Wang, Q., Liu, X., *Anal. Chim. Acta* **2007**, 601, 10-25.

[133] Taylor, A. W., Qiu, F., Hu, J., Licence, P., Walsh, D. A., *J. Phys. Chem. B* **2008**, 112, 13292-13299.

[134] Holt, K. B., *Langmuir* **2006**, 22, 4298-4304.

[135] Kiani, A., Alpuche-Aviles, M. A., Eggers, P. K., Jones, M., Gooding, J. J., Paddon-Row, M. N., Bard, A. J., *Langmuir* **2008**, 24, 2841-2849.

[136] Pust, S. E., Scharnweber, D., Baunack, S., Wittstock, G., *J. Electrochem. Soc.* **2007**, 154, C508-C514.

[137] Zhang, J., Unwin, P. R., *J. Chem. Soc., Perkin Trans. 2* **2001**, 1608-1612.

[138] Li, F., Unwin, P. R., *J. Phys. Chem. C* **2015**, 119, 4031-4043.

[139] Wei, C., Bard, A. J., Mirkin, M. V., *J. Phys. Chem.* **1995**, 99, 16033-16042.

[140] Zhang, J., Unwin, P. R., *J. Electroanal. Chem.* **2000**, 494, 47-52.

[141] Barker, A. L., Unwin, P. R., Zhang, J., *Electrochem. Commun.* **2001**, 3, 372-378.

[142] Barker, A. L., Macpherson, J. V., Slevin, C. J., Unwin, P. R., *J. Phys. Chem. B* **1998**, 102, 1586-1598.

[143] Prats, M., Tocanne, J. F., Teissie, J., Eur. *J. Biochem.* **1985**, 149, 663-668.

[144] Serowy, S., Saparov, S. M., Antonenko, Y. N., Kozlovsky, W., Hagen, V., Pohl, P., *Biophys. J.* **2003**, 84, 1031-1037.

[145] Strutwolf, J., Zhang, J., Unwin, P. R., *Prog. React. Kinet. Mech.* **2007**, 32,

195-217.

[146] Zhang, J., Unwin, P. R., *J. Am. Chem. Soc.* **2002**, 124, 2379-2383.

[147] Hansma, P. K., Drake, B., Marti, O., Gould, S. A. C., Prater, C. B., *Science* **1989**, 243, 641-643.

[148] Chen, C.-C., Zhou, Y., Baker, L. A., Annu. Rev. *Anal. Chem.* **2012**, 5, 207-228.

[149] Korchev, Y. E., Bashford, C. L., Milovanovic, M., Vodyanoy, I., Lab, M. J., *Biophys. J.* **1997**, 73, 653-658.

[150] Korchev, Y. E., Gorelik, J., Lab, M. J., Sviderskaya, E. V., Johnston, C. L., Coombes, C. R., Vodyanoy, I., Edwards, C. R. W., *Biophys. J.* **2000**, 78, 451-457.

[151] Novak, P., Li, C., Shevchuk, A. I., Stepanyan, R., Caldwell, M., Hughes, S., Smart, T. G., Gorelik, J., Ostanin, V. P., Lab, M. J., Moss, G. W. J., Frolenkov, G. I., Klenerman, D., Korchev, Y. E., *Nat. Methods* **2009**, 6, 279-281.

[152] Richards, O., Johson, N., Li, C., Novak, P., Clarke, R., Korchev, Y., Klenerman, D., *Biophys. J.* **2010**, 98, 394A-394A.

[153] Takahashi, Y., Shevchuk, A. I., Novak, P., Zhang, Y., Ebejer, N., Macpherson, J. V., Unwin, P. R., Pollard, A. J., Roy, D., Clifford, C. A., Shiku, H., Matsue, T., Klenerman, D., Korchev, Y. E., *Angew. Chem., Int. Ed.* **2011**, 50, 9638-9642.

[154] Miragoli, M., Moshkov, A., Novak, P., Shevchuk, A., Nikolaev, V. O., El-Hamamsy, I., Potter, C. M. F., Wright, P., Kadir, S. H. S. A., Lyon, A. R., Mitchell, J. A., Chester, A. H., Klenerman, D., Lab, M. J., Korchev, Y. E., Harding, S. E., Gorelik, J., *J. R. Soc. Interface* **2011**, 8, 913-925.

[155] Takahashi, Y., Shevchuk, A. I., Novak, P., Babakinejad, B., Macpherson, J., Unwin, P. R., Shiku, H., Gorelik, J., Klenerman, D., Korchev, Y. E., Matsue, T., *Proc. Natl. Acad. Sci. U. S. A.* **2012**, 109, 11540-11545.

[156] McKelvey, K., Perry, D., Byers, J. C., Colburn, A. W., Unwin, P. R., *Anal. Chem.* **2014**, 86, 3639-3646.

[157] Morris, C. A., Friedman, A. K., Baker, L. A., *Analyst* **2010**, 135, 2190-2202.

[158] Ying, L. M., Bruckbauer, A., Zhou, D. J., Gorelik, J., Shevehuk, A., Lab, M., Korchev, Y., Klenerman, D., *Phys. Chem. Chem. Phys.* **2005**, 7, 2859-2866.

[159] Li, C., Johnson, N., Ostanin, V., Shevchuk, A., Ying, L., Korchev, Y., Klenerman, D., *Prog. Nat. Sci.-Mat. Int.* **2008**, 18, 671-677.

[160] Edwards, M. A., Williams, C. G., Whitworth, A. L., Unwin, P. R., *Anal. Chem.* **2009**, 81, 4482-4492.

[161] Korchev, Y. E., Milovanovic, M., Bashford, C. L., Bennett, D. C., Sviderskaya, E. V., Vodyanoy, I., Lab, M. J., *J. Microsc. (Oxford, U. K.)* **1997**, 188, 17-23.

[162] Milovanovic, M., Korchev, Y. E., Lab, M. J., Bashford, C. L., *Biophys. J.* **1997**, 72, TU430-TU430.

[163] Boecker, M., Anczykowski, B., Wegener, J., Schaeffer, T. E., *Nanotechnology* **2007**, 18.

[164] Nadappuram, B. P., McKelvey, K., Al Botros, R., Colburn, A. W., Unwin, P. R., *Anal. Chem.* **2013**, 85, 8070-8074.

[165] Liu, X., Yang, X., Zhang, X., Lu, H., Liu, L., Zhang, Y., Chin. J. *Biomed. Eng. (Beijing, China, Engl. Ed.)* **2010**, 27, 1365-1378.

[166] McKelvey, K., Kinnear, S. L., Perry, D., Momotenko, D., Unwin, P. R., *J. Am. Chem. Soc.* **2014**, 136, 13735-13744.

[167] Li, P., Liu, L., Wang, Y., Yang, Y., Zhang, C., Li, G., *Appl. Phys. Lett.* **2014**, 105.

[168] Zhang, Y. J., Gorelik, J., Sanchez, D., Shevchuk, A., Lab, M., Vodyanoy, I.,

Klenerman, D., Edwards, C., Korchev, Y., *Kidney Int.* **200**5, 68, 1071-1077.

[169] Gorelik, J., Ali, N. N., Shevchuk, A. I., Lab, M., Williamson, C., Harding, S. E., Korchev, Y. E., *Tissue Eng.* **2006**, 12, 657-664.

[170] Shin, W., Gillis, K. D., *Biophys. J.* 2006, 91, L63-L65.

[171] Liu, B.-C., Lu, X.-Y., Song, X., Lei, K.-Y., Alli, A. A., Bao, H.-F., Eaton, D. C., Ma, H.-P., *Front. Physiol.* **2013**, 3.

[172] Happel, P., Dietzel, I. D., *j. Nanobiotechnol* **2009**, 7.

[173] Happel, P., Thatenhorst, D., Dietzel, I. D., *Sensors* **2012**, 12, 14983-15008.

[174] Walker, S. C., Allen, S., Bell, G., Roberts, C. J., *Microsc.* **2015**, 258, 119-126.

[175] Seifert, J., Rheinlaender, J., Novak, P., Korchev, Y. E., Schaffer, T. E., *Langmuir* **2015**, 31, 6807-6813.

[176] Novak, P., Li, C., Shevchuk, A. I., Stepanyan, R., Caldwell, M., Hughes, S., Smart, T. G., Gorelik, J., Ostanin, V. P., Lab, M. J., Moss, G. W. J., Frolenkov, G. I., Klenerman, D., Korchev, Y. E., *Nat. Methods* **2009**, 6, 935-935.

[177] Liu, X., Yang, X., Zhang, B., Zhang, X., Lu, H., Zhang, J., Zhang, Y., *Brain Res.* **2011**, 1386, 35-40.

[178] Yang, X., Liu, X., Zhang, X., Lu, H., Zhang, J., Zhang, Y., *Ultramicroscopy* **2011**, 111, 1417-1422.

[179] Zhao, X., Liu, X., Lu, H., Ma, L., Gao, R., Zhang, J., Gao, M., Zhang, Y., in: Chen, R. (Ed.), *Front. Nanosc. Tech.* **2011**, pp. 54-58.

[180] Chen, X., Zhu, H., Liu, X., Lu, H., Li, Y., Wang, J., Liu, H., Zhang, J., Ma, Q., Zhang, Y., *J. Membr. Biol.* **2013**, 246, 7-11.

[181] Velez-Ortega, A. C., Belov, O., Novak, P., Rawashdeh, S. A., Sinha, G. P., Korchev, Y. E., Frolenkov, G. I., *Biophys. J.* **2014**, 106, 797A-798A.

[182] Takahashi, Y., Murakami, Y., Nagamine, K., Shiku, H., Aoyagi, S., Yasukawa, T., Kanzaki, M., Matsue, T., *Phys. Chem. Chem. Phys.* **2010**, 12, 10012-10017.

[183] Takahashi, Y., Ito, K., Wang, X., Matsumae, Y., Komaki, H., Kumatani, A., Ino, K., Shiku, H., Matsue, T., *Electrochemistry* 2014, 82, 331-334.

[184] Chen, C.-C., Baker, L. A., *Analyst* **2011**, 136, 90-97.

[185] Chen, C.-C., Zhou, Y., Baker, L. A., *ACS Nano* **2011**, 5, 8404-8411.

[186] Weber, A. E., Baker, L. A., *J. Electrochem. Soc.* **2014**, 161, H924-H929.

[187] Hassel, A. W., Seo, M., *Electrochim. Acta* **1999**, 44, 3769-3777.

[188] Lohrengel, M. M., Moehring, A., Pilaski, M., Fresenius J. *Anal. Chem.*. **2000**, 367, 334-339.

[189] Lohrengel, M. M., Moehring, A., Pilaski, M., *Electrochim. Acta* **2001**, 47, 137-141.

[190] Ebejer, N., G*ü*ell, A. G., Lai, S. C. S., McKelvey, K., Snowden, M. E., Unwin, P. R., *Annu. Rev. Anal. Chem.* **2013**, 6, 329-351.

[191] Gasiorowski, J., Mardare, A. I., Sariciftci, N. S., Hassel, A. W., *J. Electroanal. Chem.* **2013**, 691, 77-82.

[192] Gregoire, J. M., Xiang, C., Liu, X., Marcin, M., Jin, J., *Rev. Sci. Instrum.* **2013**, 84.

[193] Arjmand, F., Adriaens, A., *J. Solid State Electrochem.* **2014**, 18, 1779-1788.

[194] Clausmeyer, J., Henig, J., Schuhmann, W., Plumere, N., *Chemphyschem* **2014**, 15, 151-156.

[195] Gasiorowski, J., Kollender, J. P., Hingerl, K., Sariciftci, N. S., Mardare, A. I., Hassel, A. W., *Phys. Chem. Chem. Phys.* **2014**, 16, 3739-3748.

[196] Ebejer, N., Schnippering, M., Colburn, A. W., Edwards, M. A., Unwin, P.

R., *Anal. Chem.* **2010**, 82, 9141-9145.

[197] Snowden, M. E., G*ü*ell, A. G., Lai, S. C. S., McKelvey, K., Ebejer, N., O'Connell, M. A., Colburn, A. W., Unwin, P. R., *Anal. Chem.* **2012**, 84, 2483-2491.

[198] Momotenko, D., Qiao, L., Cortes-Salazar, F., Lesch, A., Wittstock, G., Girault, H. H., *Anal. Chem.* **2012**, 84, 6630-6637.

[199] Williams, C. G., Edwards, M. A., Colley, A. L., Macpherson, J. V., Unwin, P. R., *Anal. Chem.* **2009**, 81, 2486-2495.

[200] Yang, D. Z., Han, L. H., Yang, Y., Zhao, L. B., Zong, C., Huang, Y. F., Zhan, D. P., Tian, Z. Q., *Angew. Chem., Int. Ed.* **2011**, 50, 8679-8682.

[201] Zhan, D. P., Yang, D. Z., Zhu, Y. L., Wu, X. R., Tian, Z. Q., *Chem. Commun.* **2012**, 48, 11449-11451.

[202] Miller, T. S., Macpherson, J. V., Unwin, P. R., *J. Electroanal. Chem.* **2014**, 729, 80-86.

[203] Miller, T. S., Macpherson, J. V., Unwin, P. R., *Phys. Chem. Chem. Phys.* **2014**, 16, 9966-9973.

[204] Miller, T. S., Sansuk, S., Pei, S. E., Lai, S. C. S., Macpherson, J. V., Unwin, P. R., *Catal. Today* **2015**, 244, 136-145.

[205] Mirkin, M. V., Amemiya, S., *Nanoelectrochemistry*, CRC Press 2015.

[206] Rodolfa, K. T., Bruckbauer, A., Zhou, D. J., Korchev, Y. E., Klenerman, D., *Angew. Chem., Int. Ed.* **2005**, 44, 6854-6859.

[207] G*ü*ell, A. G., Ebejer, N., Snowden, M. E., Macpherson, J. V., Unwin, P. R., *J. Am. Chem. Soc.* **2012**, 134, 7258-7261.

[208] Kirkman, P. M., G*ü*ell, A. G., Cuharuc, A. S., Unwin, P. R., *J. Am. Chem. Soc.* **2014**, 136, 36-39.

[209] Zhang, G., Kirkman, P. M., Patel, A. N., Cuharuc, A. S., McKelvey, K., Unwin, P. R., *J. Am. Chem. Soc.* **2014**, 136, 11444-11451.

[210] Güell, A. G., Cuharuc, A. S., Kim, Y.-R., Zhang, G., Tan, S.-y., Ebejer, N., Unwin, P. R., *ACS Nano* **2015**, 9, 3558-3571.

[211] Aaronson, B. D. B., Chen, C.-H., Li, H., Koper, M. T. M., Lai, S. C. S., Unwin, P. R., *J. Am. Chem. Soc.* **2013**, 135, 3873-3880.

[212] Chen, C.-H., Meadows, K. E., Cuharuc, A., Lai, S. C. S., Unwin, P. R., *Phys. Chem. Chem. Phys.* **2014**, 16, 18545-18552.

[213] Aaronson, B. D. B., Byers, J. C., Colburn, A. W., McKelvey, K., Unwin, P. R., *Anal. Chem.* **2015**, 87, 4129-4133.

[214] Chen, C.-H., Jacobse, L., McKelvey, K., Lai, S. C. S., Koper, M. T. M., Unwin, P. R., *Anal. Chem.* **2015**, 87, 5782-5789.

[215] Actis, P., Tokar, S., Clausmeyer, J., Babakinejad, B., Mikhaleva, S., Cornut, R., Takahashi, Y., Cordoba, A. L., Novak, P., Shevchuck, A. I., Dougan, J. A., Kazarian, S. G., Gorelkin, P. V., Erofeev, A. S., Yaminsky, I. V., Unwin, P. R., Schuhmann, W., Klenerman, D., Rusakov, D. A., Sviderskaya, E. V., Korchev, Y. E., *ACS Nano* **2014**, 8, 875-884.

[216] Güell, A. G., Ebejer, N., Snowden, M. E., McKelvey, K., Macpherson, J. V., Unwin, P. R., *Proc. Natl. Acad. Sci. U. S. A.* **2012**, 109, 11487-11492.

[217] Güell, A. G., Meadows, K. E., Dudin, P. V., Ebejer, N., Macpherson, J. V., Unwin, P. R., *Nano Lett.* **2014**, 14, 220-224.

[218] Güell, A. G., Meadows, K. E., Dudin, P. V., Ebejer, N., Byers, J. C., Macpherson, J. V., Unwin, P. R., *Faraday Discuss.* **2014,** 172, 439-455.

[219] McKelvey, K., O'Connell, M. A., Unwin, P. R., *Chem. Commun.* **2013**, 49, 2986-2988.

[220] Patten, H. V., Lai, S. C. S., Macpherson, J. V., Unwin, P. R., *Anal. Chem.* **2012**, 84, 5427-5432.

[221] Patten, H. V., Hutton, L. A., Webb, J. R., Newton, M. E., Unwin, P. R., Macpherson, J. V., *Chem. Commun.* **2015**, 51, 164-167.

[222] Kinnear, S. L., McKelvey, K., Snowden, M. E., Peruffo, M., Colburn, A. W., Unwin, P. R., *Langmuir* **2013**, 29, 15565-15572.

[223] Parker, A. S., Patel, A. N., Al Botros, R., Snowden, M. E., McKelvey, K., Unwin, P. R., Ashcroft, A. T., Carvell, M., Joiner, A., Peruffo, M., *J. dent.* **2014**, 42 Suppl 1, S21-29.

[224] Takahashi, Y., Shevchuk, A. I., Novak, P., Murakami, Y., Shiku, H., Korchev, Y. E., Matsue, T., *J. Am. Chem. Soc.* **2010**, 132.

[225] Macpherson, J. V., Unwin, P. R., *Anal. Chem.* **2001**, 73, 550-557.

[226] Kranz, C., *Analyst* **2014**, 139, 336-352.

[227] Nadappuram, B. P., McKelvey, K., Al Botros, R., Colburn, A. W., Unwin, P. R., *Anal. Chem.* **2013**, 85, 8070-8074.

[228] Alvarez, O., Brodwick, M., Latorre, R., McLaughlin, A., McLaughlin, S., Szabo, G., *Biophys. J.* **1983**, 44, 333-342.

[229] O'Connell, M. A., Wain, A. J., *Anal. Chem.* **2014**, 86, 12100-12107.

[230] O'Connell, M. A., Lewis, J. R., Wain, A. J., *Chem. Commun.* **2015**, 51, 10314-10317.

[231] Ino, K., Ono, K., Arai, T., Takahashi, Y., Shiku, H., Matsue, T., *Anal. Chem.* **2013**, 85, 3832-3835.

[232] Korchev, Y. E., Negulyaev, Y. A., Edwards, C. R. W., Vodyanoy, I., Lab, M. J., *Nat. Cell Biol.* **2000**, 2, 616-619.

[233] Sen, M., Takahashi, Y., Matsumae, Y., Horiguchi, Y., Kumatani, A., Ino,

K., Shiku, H., Matsue, T., *Anal. Chem.* **2015**, 87, 3484-3489.

[234] Rutkowska, A., Bawazeer, T. M., Macpherson, J. V., Unwin, P. R., *Phys. Chem. Chem. Phys.* **2011**, 13, 5223-5226.

[235] Rudd, N. C., Cannan, S., Bitziou, E., Ciani, L., Whitworth, A. L., Unwin, P. R., *Anal. Chem.* **2005**, 77, 6205-6217.

[236] Cannan, S., Macklam, I. D., Unwin, P. R., *Electrochem. Commun.* **2002**, 4, 886-892.

[237] Oyamatsu, D., Kanaya, N., Shiku, H., Nishizawa, M., Matsue, T., *Sens. Actuators, B* **2003**, 91, 199-204.

Chapter 2

Experimental Methods

This chapter describes the materials and the experimental procedure used throughout this thesis. Details of the carbon electrode fabrication procedure is also explained, along with descriptions of the electrochemical configuration and instrumentation of various electrochemical scanning probe microscopy techniques employed in the studies described within this thesis.

2.1 Chemicals

All aqueous solutions were prepared with 18.2 M Milli-Q reagent water (Millipore Corp.). A detailed list of chemicals used in this thesis is given in Table 2.1. All chemicals, unless otherwise mentioned, were used as received. Chemicals were weighed using a four decimal place analytical balance (Sartorius A2008) and Solution pH values were measured using a pH meter (UltraBASIC pH meter, Denver Instruments). All experiments were performed at room temperature.

Table 2.1: List of chemicals used in this thesis.

Chemical	**Purity**	**Supplier**
Potassium chloride	>99.99%	Fisher Scientific
Hexaammineruthenium(III)chloride	>99.00%	Strem Chemicals
Potassium nitrate	>99.99%	Sigma-Aldrich
4-(2-hydroxyethyl)-1-piperazineethanesulfonic acid		Sigma-Aldrich
Iceland spar calcite (naturally occurring from Creel, Mexico)		Richard Tayler Minerals
Ferrocenylmethyltrimethylammonium iodide	>99%	Strem Chemicals
Silver hexafluorophosphate	>99%	Strem Chemicals
Sulfuric acid	>99.99%	Sigma-Aldrich
Sodium fluoride	>99%	Sigma-Aldrich
Fluorescein sodium salt		Sigma-Aldrich
Egg phosphatidyl choline		Avanti Polar Lipids
Poly-L-Lysine	>99%	Sigma-Aldrich
Poly-L-glutamic acid	>99%	Sigma-Aldrich
1,2-dipalmitoyl-sn-glycero-3-phosphocholine	>99%	Avanti Polar Lipids
Soy phosphatidylcholine	>95%	Avanti Polar Lipids
1,2-dioctadecanoyl-sn-glycero-3-phospho-(1'-rac-glycerol)	>99%	Avanti Polar Lipids
Chloroform	>99.8%	Sigma-Aldrich
1-butyl-3-methlimidazolium tetrafluoroborate		Sigma-Aldrich
Phosphate buffer solution (pH 7.2)		Fluka
Iridium tetrachloride hydrate	>99.99%	Sigma-Aldrich
Hydrogen peroxide solution	>30%w/w	Sigma-Aldrich
Oxalic acid dihydrate	>99.99%	Sigma-Aldrich
Potassium carbonate	>99.99%	Sigma-Aldrich
Calcium Chloride	>99.99%	Sigma-Aldrich
Sodium Hydroxide	>99.99%	Sigma-Aldrich

Sorbitol		Sigma-Aldrich
3-(3,4-dichlorophenyl)-1,1-dimenthylurea	>98.00%	Sigma-Aldrich
Ferritin (horse spleen)		Sigma-Aldrich
Percoll		Sigma-Aldrich

2.2 Fabrication of Carbon Electrodes

The carbon electrode used in this thesis was fabricated by a two-step process.[1-4] Briefly, in the first step a suitable quartz capillary was pulled in a laser puller (P-2000, Sutter Instruments) to a sharp point pipet using custom-developed two line programs.

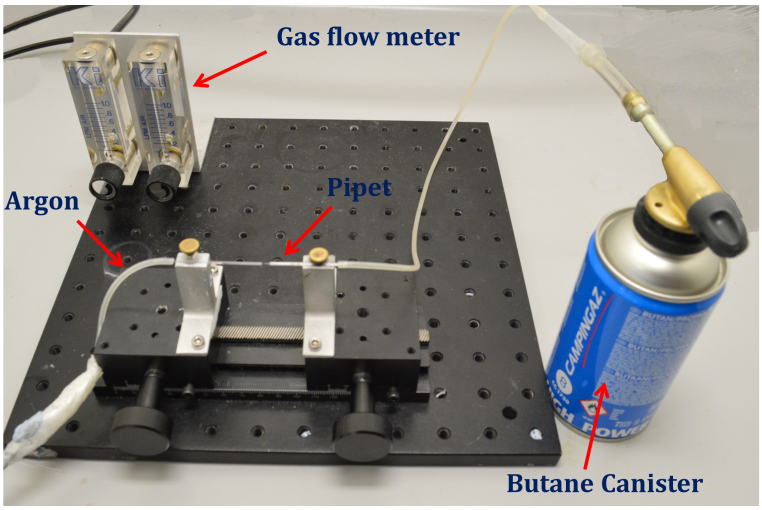

Figure 2.1: Illustration showing the carbon electrode fabrication set-up. The pulled pipets were fixed onto a Tygon (Saint-Gobain) tube with a carbon feed-stock (butane, Campingaz) flowing through and placed in a holder with another quartz pipet fixed opposite, through which argon was flowed. The tip of the probe was heated with a butane torch to pyrolytically deposit carbon from the butane.

For fabricating the dual carbon electrodes described in Chapter 3, and the pH-SICM probe described in Chapter 4, quartz theta capillaries were used (O.D.

1.2 mm, I.D. 0.90 mm, Intracel) The multifunctional probes described in chapter 5 and 6 were fabricated from quartz quadruple-barrelled capillaries (MBT-015-062-4Q, Friedrich and Dimmock, Inc.).

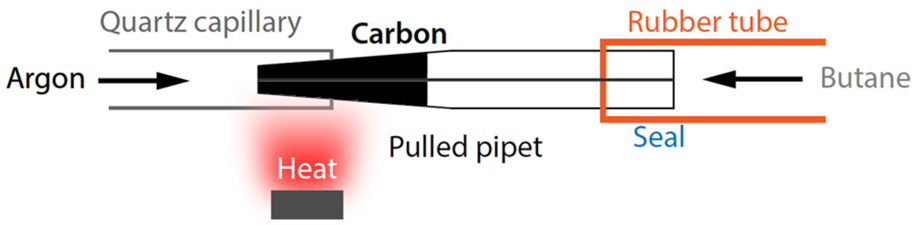

Figure 2.2: Schematic of the carbon deposition step for the fabrication of carbon electrodes. Butane passed through the pulled pipet barrels and pyrolyzed using a hand held butane torch under an argon atmosphere.

The pulled pipets were then fixed onto a Tygon (Saint-Gobain) tube with a carbon feedstock (butane, Campingaz) flowing through and placed in a holder with another quartz pipet fixed opposite, through which argon was flowed, as shown in Figure 2.1. To prevent deposition of carbon inside one or more barrels (in case of the pH-SICM and multifunctional probes), the required barrel(s) were closed by using Blu-Tack (Bostik). The two pipets were then pushed close together with the pipet flowing argon through covering the end of the theta pipet. A gas blow torch (RS Components) was then used to heat the covered end, to pyrolytically deposit carbon from the butane, as illustrated in Figure 2.2, producing an extensive filling of carbon inside the sharp ended pipet barrel(s). A more detailed description of the fabrication of dual carbon, pH-SICM and multifunctional probes were given in chapter 3, 4 and 5 respectively.

2.3 Thylakoid Membrane Sample Preparation

Thylakoid membranes were prepared from the leaves of 8 to 9 day old peas (*Pisum sativum*, var. Kelvedon Wonder) using a mechanical disruption method.[5] First, chloroplasts S2 were prepared by homogenizing pea leaves using a Polytron blender (Kinematica GmbH) in HS buffer (50 mM HEPES, 0.33 M Sorbitol (Sigma-Aldrich)) andKOH to adjust the pH to 8.0. This solution was then filtered through Microcloth (Calbiochem) and centrifuged (3300 x g for 2 minutes). The chloroplast pellet was re-suspended in 2 ml of HS buffer and moved onto a Percoll pad (2 ml of 5 HS, 3.5 ml Percoll and 4.5 ml Milli-Q water), before being centrifuged (1400 x g for 8 minutes). The supernatant was discarded and the pellet resuspended in 10 ml HS buffer before being centrifuged (3000 x g for 2 minutes) and finally being re-suspended in HS buffer (0.5 ml). Thylakoid membranes were prepared from the chloroplasts by taking 0.4 ml of the solution, centrifuging (7000 rpm for 2 minutes) and then re-suspending in HM buffer on ice for 5 minutes to osmotically lyse the chloroplasts, and expose the thylakoid membranes. This solution was then washed twice in HS buffer and once in HM buffer by centrifuging (14,000 rpm for 2 minutes) and re- suspending. Thylakoid membranes were then re-suspended in 0.4 ml HM buffer and kept on ice. Finally, thylakoid membranes were deposited on poly-L-lysine-covered glass bottomed petri dishes immediately before experiments.

2.4 Preparation of Calcite Microcrystals

Calcite microcrystal samples for the pH-SICM study were prepared by a precipitation process.[6] Briefly, equal volumes of solutions of 0.005 M calcium chloride and 0.01 M sodium bicarbonate (pH 10.5) were mixed in a glass petri dish. The dish was then left open in a clean environment, and after 24 hours microcrystals formed on the base of the dish, with typical dimensions ca. 30 μm x 30 μm surface area and 20-30 μm height. The solution was washed away with Milli-Q water, and the crystals were then dried with a stream of nitrogen.

2.5 Preparation of Iridium Oxide Electrodeposition Solution

The electrodeposition solution was prepared according to the method described by Yamanaka.[7,8] Briefly, 0.15 g of iridium tetrachloride, 1 mL of 30% w/w H_2O_2, and 0.5 g of oxalic acid dihydrate were added gradually to 100 mL of Milli-Q water over an interval of 30-60 min and were left to dissolve in a stirred solution. Anhydrous potassium carbonate was then added incrementally until the pH reached 10.5, forming a pale yellow solution. The solution was covered and left at room temperature for 48 h during which a color change to pale blue occurred. This solution was stored in a refrigerator and could be used for a few months to successfully produce iridium oxide films.

2.6 Preparation of Single-Walled Carbon Nanotube Samples

Single-walled carbon nanotube (SWNT) samples were prepared by using a catalytic chemical vapour deposition method.[9] Briefly, a silicon/silicon oxide substrate (IDB Technologies Ltd.,n-type Si, 525 μm thick with 300 nm thermally grown SiO_2) was cut into 1 cm x 1 cm squares and was partially immersed in an aqueous solution of horse spleen ferritin, diluted from the original concentration in a ratio of 1:200, to give a band of Ferritin along one side of the substrate. The substrates were then ashed using an oxygen plasma for 2 minutes (K1050X plasma system,Emitech, UK) to break down the ferritin molecules exposing the catalytic iron nanoparticles on the substrate surface. The samples were then placed in the cold wall CVD reactor with the catalyst nanoparticles in line with the direction of flow. The samples were heated to 950 °C under a flow of 150 sccm hydrogen and 250 sccm argon for 5 minutes. Ethanol was then introduced to the system via a flow of 250 sccm argon with 150 sccm hydrogen, which was maintained for 5 minutes. After this period, the system was left to cool under an argon flow (1000 sccm). by means of a thermally evaporated 100 nm palladium layer deposited at the side of the substrate (60-90 nm, with a 2 nm Cr adhesive layer)

2.7 EC-SPM Instrumentation

All electrochemical measurements described in this thesis were performed on the Warwick electrochemical scanning probe microscopy (WEC-SPM) platform developed in-house, unless otherwise mentioned. Figure 2.3 shows the components of a

typical WEC-SPM set-up.

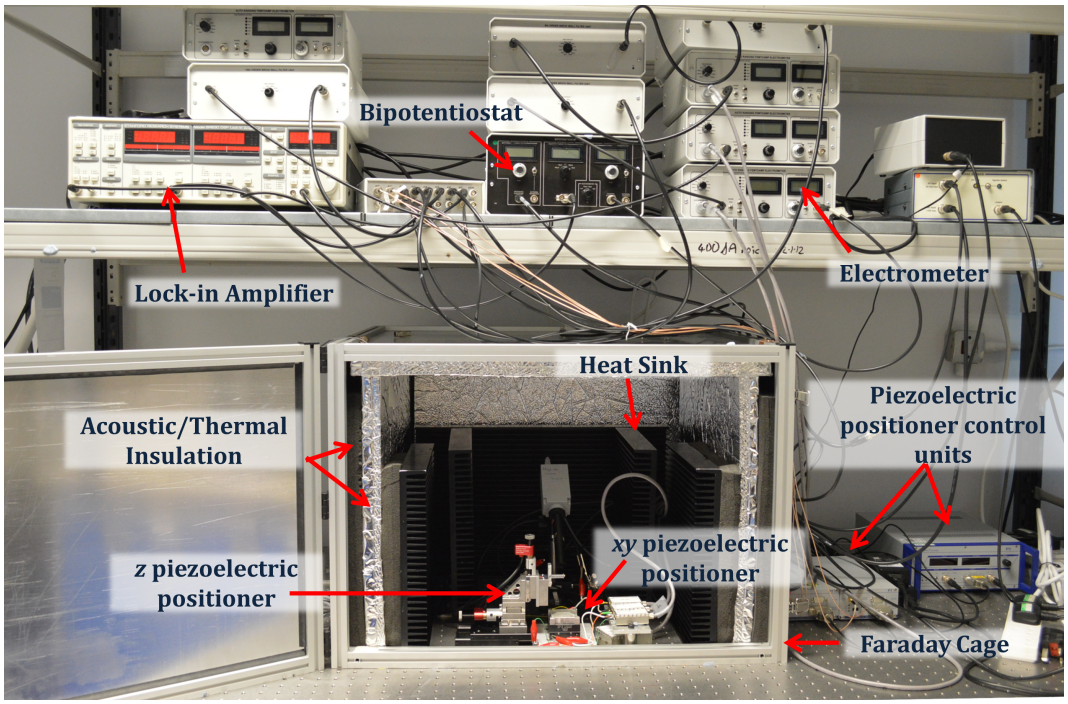

Figure 2.3: Illustration showing the Warwick electrochemical scanning probe microscopy (WEC-SPM) set-up.

In general for electrochemical measurements, the tip electrode (not shown in the figure) was mounted perpendicular to the surface of interest on a single axis (z) piezoelectric positioner (P-753-3CD, Physik Instrumente) to control the height of the probe. This, in turn, was attached to a micrometer-driven 3-axis stage (Newport, 461-XYZ-M) for manual coarse positioning and a pico-motor driven z-positioner for controlled coarse vertical positioning. A lock-in amplifier (SR830, Stanford Research Systems) was typically used to generate a oscillating signal for modulating the probe in the z direction during tip approach measurements and imaging. An x-y piezoelectric positioner (Nano-BioS300, Mad City Labs, Inc.) was

used for lateral positioning of the sample substrate with respect to the probe. The probe was positioned close to the substrate surface with the aid of a camera (B700, PixeLINK). The whole system was mounted in a Faraday cage fitted with heat sinks and thermal and acoustic shields to protect the electrochemical cell from electrical noise and to minimize thermal drift. The Faraday cage was, in turn, mounted on a vibration isolation table (RS 2000, Newport). A bipotentiostat or an electrometer(s) (both custom-built) or both were generally used for controlling the potential (bias) of the tip and /or substrate during the experiment. The instrument was controlled and data were recorded using an FPGA card (7852R, National Instruments) which, in turn, was controlled from a PC running LabVIEW 2013 (National Instruments).

2.8 SECM Measurements

Two SECM systems were used in Chapter 3, and are based on a previously described configurations.[2] Briefly, for the IC-SECM approach curve measurements a DCE was mounted on a bender-piezoelectric positioner (P-871.112, Physik Instrumente), which was in turn mounted on a 3 axis piezoelectric positioner (611.3S Nanocube, Physik Instrumente). The bender piezoelectric positioner was used to oscillate the probe normal to the surface; and also measure the oscillation amplitude of the probe, through the inbuilt strain gauge sensor for the approach curves that used IC-SECM mode.[2] For the thylakoid membrane measurements a DCE was mounted directly on a 3 axis piezoelectric positioner (611.3S Nanocube, Physik Instrumente). This was situated on a confocal microscope (TCS SP5 MP, Lieca). Within both configurations, the piezoelectric positioners were mounted on

micropositioners (Newport Corp.) inside a Faraday cage with vibration isolation (granite slab or an optical table). The piezoelectric positioners were controlled and the currents recorded through either a DAQ card (E-671, National Instruments) or a FPGA card (PCIe-7852R, National Instruments), which was, in turn, controlled using custom code from a PC running LabVIEW 2010 or LabVIEW 2011 (National Instruments).

2.9 pH-SICM Measurements

For pH-SICM measurements described in chapter 4, the probe was mounted perpendicular to the surface of interest on a single axis (z) piezoelectric positioner (P-753-3CD, Physik Instrumente) to control the height of the probe. This, in turn, was attached to a micrometer-driven 3-axis stage (Newport, 461-XYZ-M) for coarse positioning. A lock-in amplifier (SR830, Stanford Research Systems) was used to oscillate the probe in the z direction during tip approach measurements and imaging. The petri dish containing the calcite microcrystals and solution was mounted on XY piezoelectric positioners (Nano-BioS300, Mad City Labs Inc.) for lateral positioning with respect to the probe. The entire system was mounted on an optical microscope (Axiovert 40 CFL, Zeiss) fitted with an online camera (B700, PixeLINK), which aided the selection of the crystal of interest. A Faraday cage was mounted on the microscope stage to shield the electrochemical cell. The microscope was, in turn, mounted on a vibration isolation table (RS 2000, Newport). A home-built, high sensitivity bipotentiostat was used to measure the ion current between the Ag/AgCl QRCE in the bulk of the solution and the Ag/AgCl QRCE in the open, KCl-filled, barrel of the pH-SICM probe. The open-circuit

potential between the nanoscale pH electrode and the Ag/AgCl QRCE in the bulk solution was measured using a home-built voltage follower. The piezoelectric positioners were controlled using an FPGA card (7852R, National Instruments), which, in turn, was controlled from a PC running Labview 2011 (National Instruments). The FPGA card was also used to record the SICM current and pH electrode potential.

2.10 Pressure/Area Isotherms Recording

Pressure/area isotherms for DPPC monolayers on aqueous electrolyte solution were recorded using a Langmuir trough (Nima Technology, Model 611D), with surface pressures measured using a Wilhemy balance.

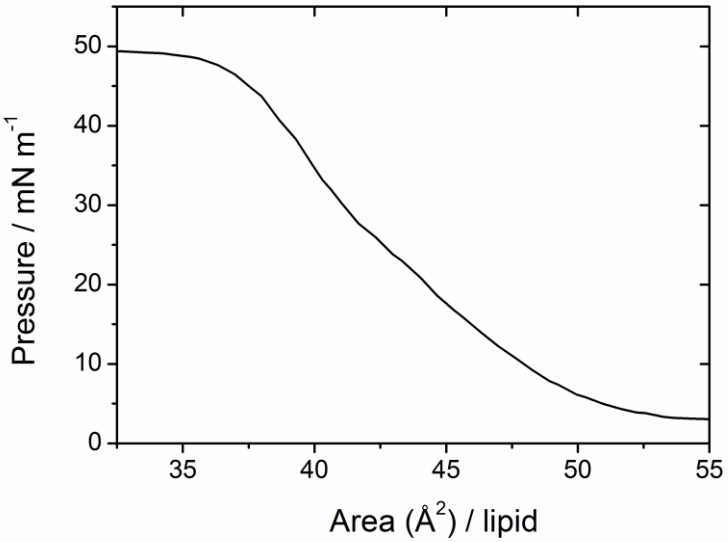

Figure 2.4: Pressure/area isotherm for the compression of a DPPC monolayer.

The Langmuir trough was first thoroughly cleaned with chloroform, and a

pressure/area isotherm was run to check that there was no surface contamination. After cleaning, 50 μl of 0.5 mg/ml DPPC in chloroform was deposited onto the 0.1 M KCl subphase, and the solvent allowed to evaporate before compression was initiated. These isotherms indicated that the area per molecule in a fully assembled monolayer is $\sim$35 $A^{\circ 2}$ with a surface pressure of $\sim$50 mN m^{-1} (Figure 2.4). To ensure full monolayer coverage on the surface of the bulk electrolyte solution in the CLSM cell, 10 μl of 1 mg/ml lipid solution was added, yielding an area per lipid of 34 $A^{\circ 2}$.

2.11 CLSM Measurements

CLSM measurements were performed using a Leica TCS SP5X confocal fluorescence system on a Leica DMI6000 inverted microscope. An Argon laser at 488 nm was used to excite the fluorescein in solution and the resulting emission was collected between 500 and 540 nm at 8000 Hz line scanning frequency with a 10x/0.3 HC PL Fluotar dry lens. The glass bottom dish containing the modified surface was mounted onto to a micrometer-driven 3-axis microscope stage (Newport). The sample was mounted onto a xyz-piezoelectric positioner (PhysLink) which, in turn, was attached to a micrometer-driven 3-axis stage (Newport) for coarse positioning. A Faraday cage was mounted on the microscope stage to shield the electrochemical cell. The microscope was, in turn, mounted on a vibration isolation table (Newport). 3D fluorescence profiles of week acid permeation across different bilayer membranes were recorded as a series of xy slices collected at 1 micrometer intervals in the z direction at a scanning frequency of 1400 Hz.

2.12 References

[1] Takahashi, Y., Shevchuk, A. I., Novak, P., Zhang, Y., Ebejer, N., Macpherson, J. V., Unwin, P. R., Pollard, A. J., Roy, D., Clifford, C. A., Shiku, H., Matsue, T., Klenerman, D., Korchev, Y. E., *Angew. Chem., Int. Ed.* **2011**, 50, 9638-9642.

[2] McKelvey, K., Nadappuram, B. P., Actis, P., Takahashi, Y., Korchev, Y. E., Matsue, T., Robinson, C., Unwin, P. R., *Anal. Chem.* **2013**, 85, 7519-7526.

[3] Nadappuram, B. P., McKelvey, K., Byers, J. C., Gueell, A. G., Colburn, A. W., Lazenby, R. A., Unwin, P. R., *Anal. Chem.* **2015**, 87, 3566-3573.

[4] Nadappuram, B. P., McKelvey, K., Al Botros, R., Colburn, A. W., Unwin, P. R., *Anal. Chem.* **2013**, 85, 8070-8074.

[5] Mills, W. R.; Joy, K. W. *Planta* **1980**, 148, 7583

[6] Kazmierczak, T. F.; Tomson, M. B.; Nancollas, G. H., *J. Phys. Chem.* **1982**, 86,103-107.

[7] Yamanaka, K. Jpn. *J. Appl. Phys. 1* **1991**, 30, 1285-1289.

[8] Bitziou, E.; O'Hare, D.; Patel, B. A. *Anal. Chem.* **2008**, 80, 8733-8740.

[9] G*ü*ell, A. G., Ebejer, N., Snowden, M. E., McKelvey, K., Macpherson, J. V., Unwin, P. R., *Proc. Natl. Acad. Sci. U. S. A.* **2012**, 109, 11487-11492.

Chapter 3

Fabrication, Characterization and Functionalization of Dual Carbon Electrodes as Probes for Scanning Electrochemical Microscopy (SECM)

This chapter reports the an easy, quick and cheap fabrication of a Dual carbon electrode (DCEs) by depositing pyrolytic carbon into a quartz theta nanopipet. The size of DCEs can be controlled by adjusting the pulling parameters used to make the nanopipet. When operated in generation/collection (G/C) mode, the small separation between the electrodes leads to reasonable collection efficiencies of ca. 30%. A three-dimensional finite element method (FEM) simulation was developed to predict the current response of these electrodes as a means of estimating the probe geometry. Voltammetric measurements at individual electrodes combined with generation/collection measurements provide a reasonable guide to the electrode size. DCEs are employed in a scanning electrochemical microscopy (SECM) configuration, and their use for both approach curves and imaging is considered.

G/C approach curve measurements are shown to be particularly sensitive to the nature of the substrate, with insulating surfaces leading to enhanced collection efficiencies, whereas conducting surfaces lead to a decrease of collection efficiency. As a proof-of-concept, DCEs are further used to locally generate an artificial electron acceptor and to follow the flux of this species and its reduced form during photosynthesis at isolated thylakoid membranes. In addition, 2-dimensional images of a single thylakoid membrane are reported and analyzed to demonstrate the high sensitivity of G/C measurements to localized surface processes. It is finally shown that individual nanometer-size electrodes can be functionalized through the selective deposition of platinum on one of the two electrodes in a DCE while leaving the other one unmodified. This provides an indication of the future versatility of this type of probe for nanoscale measurements and imaging.

3.1 Introduction

Ultramicroelectrodes (UMEs) offer high mass transport rates, low ohmic (IR) effects, low double layer charging,[1-3] and, as such, are optimal for many applications from kinetic measurements to electrochemical imaging. UMEs serve as imaging probes in scanning electrochemical microscopy (SECM), which has been used widely to study the interfacial process at the microscale and nanoscale, especially electrocatalysis[4-6] and biological systems.[7-12] However, the overwhelming majority of these systems use single electrode probes and SECM can be productively extended to increasingly complex and challenging systems through the use of dual-electrode probes. In principle, such probes would allow two redox-active species to be detected concurrently or would permit redox-active species to be generated at one electrode and collected at the other electrode.[13, 14]

Dual-electrode systems are widely used to study the kinetics of redox reactions.[15,16] Usually, but not exclusively,[17] such devices operate in an amperometric/voltammetric mode, where each electrode is held at a potential to oxidize or reduce a target species of interest, and the current measured at each electrode relates to the flux of that active species, arriving at the electrode. In generation/collection (G/C) mode, one electrode generates the species of interest (oxidizes or reduces the analyte (A) to produce an active species (S1) that is then collected at the other electrode [via oxidation or reduction to produce the starting material or another species (S2)]:

$$\text{Electrode 1: } A \pm e^- \rightleftharpoons S1$$

$$\text{Electrode 2: } S1 \pm e^- \rightleftharpoons S2$$

The flux of active species generated and collected depends on the geometry of the dual-electrode system and the mass transport between the electrodes. The G/C mode is often characterized by the collection efficiency, which is defined as the ratio of the current measured at the collector electrode to that measured at the generator electrode, usually under steady-state conditions.

Dual electrode systems that are constructed in a probe-type configuration include ring-disk,[18, 19] dual-ring,[20] and dual-disk[21-24] geometries. Probe-based dual electrode systems have been constructed using single and dual barrel (theta) borosilicate and quartz pipets as a scaffold.[21, 25] However, collection efficiencies for the majority of these systems have been low because the interelectrode distance has often been large with respect to the electrode size. A range of electrode sizes from 50 μm[21] to nm[23] have been reported, but the wider adoption of these systems has been limited due to difficulties in fabricating and characterizing the probes.

Herein, we present a quick and simple method for the fabrication of probe-based dual carbon electrodes (DCEs). This method allows the reproducible fabrication of a wide range of DCE sizes (from nanoscale to microscale). DCEs are prepared from a laser-pulled quartz theta pipet followed by pyrolytic carbon deposition. This is a development of a recent method reported for making scanning ion conductance - scanning electrochemical microscopy (SICM - SECM) probes.[25] Pyrolytic deposition of carbon to form electrodes is a popular method, employed to form several different SECM probes.[20, 26-28]

Nanoscale DCEs are rather challenging to characterize geometrically. [29-31] As part of this study, we therefore developed a finite element method (FEM) simulation that allowed the effective geometry of individual nanoscale probes to be estimated from single-barrel voltammetry and G/C measurements. Furthermore,

to demonstrate the suitability of these probes for SECM and to provide further insight into the probe geometry, approach curves, to insulating (inert) and conductive (active) surfaces, were recorded in the probe G/C mode using intermittent contact-SECM (IC-SECM).[32-35]

As a proof-of-concept, we used DCEs to study photosynthesis, at a film of isolated thylakoid membranes. In higher plants, thylakoid membranes contain the light-dependent components of photosynthesis, where light is absorbed and used to split water into oxygen, proton and electron (at photosystem II).[36] Electrons, produced from the splitting of water, are transferred through the linear electron transport pathway before being used to produce the energy-rich molecule, NADPH.[36] Interestingly, a number of artificial electron acceptors can intercept the electrons and be reduced by various components of this thylakoid membrane-bound electron transport pathway.[36, 37]We use a DCE to locally generate an artificial electron acceptor (oxidizing ferrocenylmethyl trimethylammonium, $FcTMA^{+}$, to produce $FcTMA^{2+}$) and to monitor the local flux of both species. The SECM platform also allowed us to construct two-dimensional (2D) current images of a single thylakoid membrane, highlighting the subtle interactions of a locally generated electron acceptor with a dynamic biological membrane.

Finally, we show that individual electrodes within a single probe can be functionalized, through the selective deposition of platinum. This demonstrates that DCEs could be used as a platform for a range of chemical sensing applications in the future.

3.2 Materials and Methods

Materials and reagents, together with details of the protocols used to prepare thylakoid membranes, are detailed in Chapter 2.

3.2.1 Electrode Fabrication

DCEs were fabricated by adapting the method previously described by Takahashi et al.[25] Quartz theta pipets (o.d., 1.2 mm, i.d., 0.9 mm, Intracell) were pulled using a laser puller (P-2000, Sutter Instruments); with a two step program (step 1: HEAT = 750; FILAMENT = 4; VELOCITY = 20; DELAY = 140; PULL = 60. step 2: HEAT = 700; FILAMENT = 3; VELOCITY = 40; DELAY = 135; PULL = 90). The smaller probes, used for the Pt deposition experiment, used a single step program (HEAT = 760; FILAMENT = 3; VELOCITY = 45; DELAY = 130; PULL = 90). Butane was passed through the pulled pipet, via tubing, under an argon atmosphere.The tip of the probe was heated with a butane torch for 35 s, to pyrolytically deposit carbon from the butane, as illustrated in Figure 3.1A. Electrical contact to each electrode was established by inserting a copper wire through the top end of the pipet barrel to make contact with the carbon layers. A field-emission scanning electron micrograph (SEM) (Supra 55-VP, Zeiss) of a typical nanoscale DCE is shown in Figure 3.1B, and an optical image of a larger DCE is shown in Figure 3.1C. The larger DCEs were constructed by polishing smaller DCEs on diamond lapping disks (Buehler).

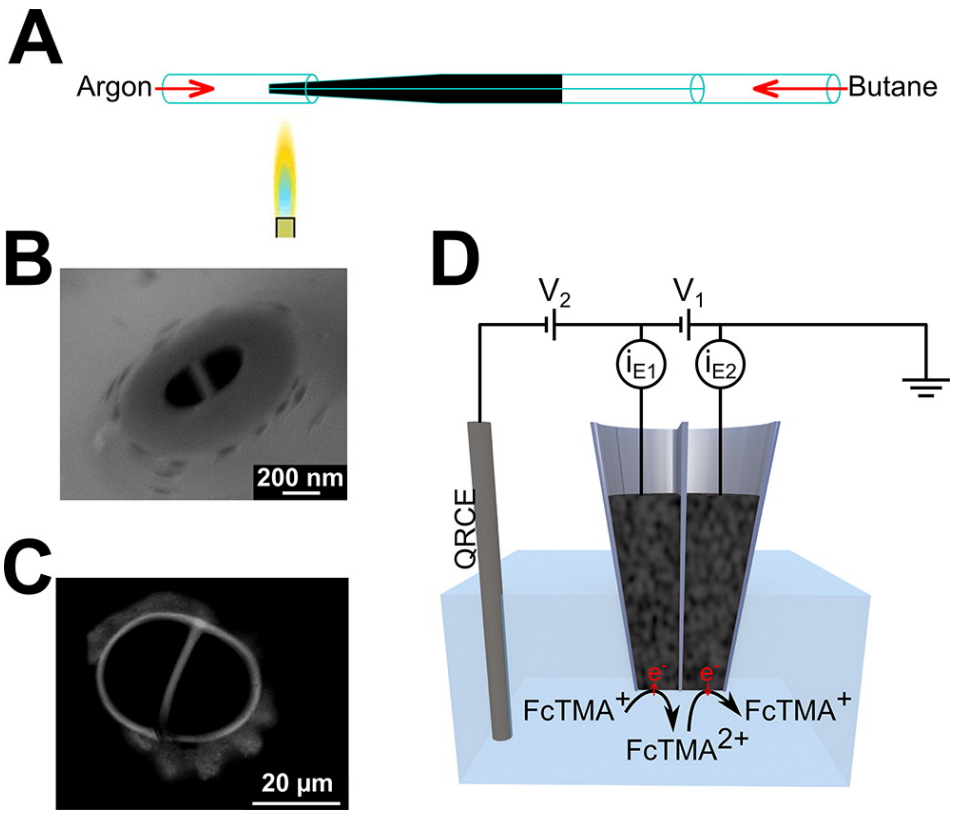

Figure 3.1: (A) Schematic of the carbon deposition step of dual-electrode fabrication, in which butane is passed through the pulled quartz theta pipet and pyrolyzed using a hand-held butane torch under an argon atmosphere. (B) SEM of a typical nanoscale DCE. (C) Optical image of a micrometer-scale DCE. (D) Schematic of dual-electrode configuration, with two working electrodes in the barrels of the probe and an Ag/AgCl QRCE in solution. The current is measured at each working electrode (i_{E1} and i_{E2}), while the potential of the working electrodes, with respect to the QRCE, is controlled by V_1 and V_2. In the G/C mode, $FcTMA^+$ is oxidized at one electrode to produce $FcTMA^{2+}$ that is reduced at the other electrode.

3.2.2 Electrochemical Measurements

A three-electrode configuration was used, with two working electrodes (the two electrodes of the probe) and a single Ag/AgCl (silver chloride-coated silver wire) quasi reference/counter electrode (QRCE) in the bulk of the solution, as illustrated in Figure 3.1D. In the G/C mode, the potential of one electrode was set to 0.5 V with respect to the QRCE for the diffusion-limited one-electron oxidation of $FcTMA^{+}$ to $FcTMA^{2+}$ (based on the LSVs, see Figure 3.3), and the other electrode was at 0 V with respect to the QRCE for the diffusion-limited one-electron reduction of $FcTMA^{2+}$. This was achieved in our electrochemical configuration by setting V_1 = 0.5 V and V_2 = - 0.5 V (Figure 3.1D). The current at each working electrode was measured using a custom-built high sensitivity bipotentiostat (a description of the SECM instrument is given in chapter 2 of this thesis).

3.2.3 Simulations and Theory

Electrochemical measurements provide a quick estimation of the apparent size of an electrode.[29] We developed a steady-state three-dimensional (3D) FEM simulation of nanoscale (100 to 1000 nm) DCEs based on the probe geometry observed in SEM images of typical nanoscale DCEs (e.g., Figure 3.1B) to estimate the probe geometry from steady-state diffusion-limited currents.

A stationary diffusion equation describes the transport of $FcTMA^{+}$ (redox species in bulk solution):

$$D\nabla^{2}c = 0 \qquad (0)$$

where D is the diffusion coefficient (which was 6.0 x 10^{-6} cm^2 s^{-1}) and c is the con-

centration of $FcTMA^+$. The concentration of $FcTMA^{2+}$ is calculated from mass conservation by reasonably assuming equal diffusion coefficient as to $FcTMA^+$.

Two steady-state configurations were simulated: (i) a single electrode oxidizing $FcTMA^+$ to $FcTMA^{2+}$ at a diffusion-limited rate; and (ii) a G/C configuration where $FcTMA^{2+}$ was generated from the oxidation of $FcTMA^+$ at one electrode, while being collected by reduction back to $FcTMA^+$ at the other electrode.

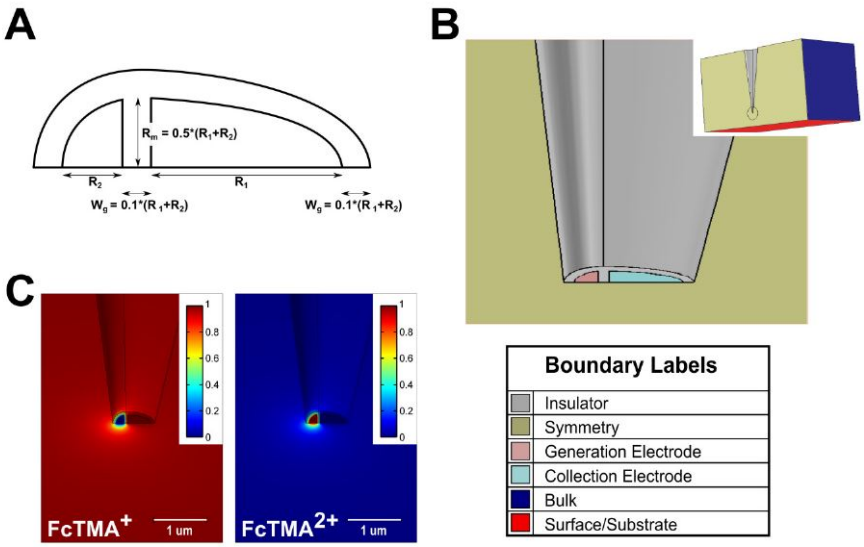

Figure 3.2: (A). Sketch of the end of a DCE probe showing dimensions used in the FE model. R1 is the major axis size of electrode 1 and R2 the major axis size for electrode 2. W_g is the width of the glass surround and is set to $0.1*(R1+R2)$. Rm is the size of the minor axis of both electrodes, and is set to $0.5*(R1+R2)$. (B). 3D geometry of the FEM model, with color coded boundaries to aid understanding of boundary conditions (see text). (C). Typical concentration profiles for $FcTMA^+$ and $FcTMA^{2+}$ (normalized with respect to the bulk concentration of $FcTMA^+$), when $FcTMA^{2+}$ is generated at the left electrode (by oxidation of $FcTMA^+$) and collected at the right electrode.

Based on the probe geometry and dimensions observed in SEM images of typical nanoscale DCEs, a FEM model of the probe geometry was developed. The geometry of the three-dimensional FEM model is summarized in Figure 3.2. Each electrode is semi-elliptical and the size is defined by major and minor axes. The major axis is the distance from the center of the electrode to the outside edge perpendicular to the septum separating the electrodes. The minor axis is the distance from the middle of the electrode to the edge of the electrode parallel to the septum. The size of the minor axis was set to the average of the two major axes, typical of representative SEM images of nanoscale DCEs. The septum width and width of the glass surround of the electrodes was set as a fifth of the minor axis size. These proportions were again based on typical SEM images of nanoscale DCEs. The outer wall of the probe has a typical taper angle of 10 degrees. Configuring the model in this way means that there are only two independent variables in the FEM model, i.e. the major axis size for each of the electrodes. Thus, in principle, only two current measurements are needed to determine the geometry of the probe. Recession, or protrusion, of the carbon from the probe is a possibility as we will discuss latter; however this is not considered in this simple model as it would introduce a number of additional independent variables, which would complicate the basic geometry determination. It is also important to point out a further simplification: we have assumed that the carbon electrode has a uniform activity; although probes formed by pyrolytic carbon deposition have been shown to have a combination of conducting sp^2 (graphitic) and non-conducting sp^3 carbon, and this could complicate the response in certain situations, as we also consider later. Figure 3.2A summarizes the forgoing description, with 2D representation of the dimensions of the end of the probe, while the full 3D geometry of the model

is shown in Figure 3.2B with boundary colours used as an aid to identify the conditions applied.

To solve the mass transport problem and calculate the currents at the DCEs, we applied the following boundary conditions (where n is the surface normal and N is the flux of $FcTMA^+$): insulating boundaries (n.N = 0) which are shown in gray in Figure 3.2B; symmetry boundaries (n.N = 0) which are shown in green on Figure S1 B; generator boundaries (c = 0) which are shown in pink on Figure 3.2B; collector boundaries (c = 1 mM) which are shown in light blue; bulk concentration boundaries (c = 1 mM) which are shown in dark blue; and a surface/substrate boundary, which is either insulating (n.N = 0) or conducting (c = 1 mM), and is shown in red on Figure 3.2B. The initial conditions for the simulations were 1 mM of $FcTMA^+$. The current at an electrode was calculated from the integral of the normal flux of active species to the electrode surface multiplied by the Faraday constant. Comsol 4.2a (Comsol) was used on a PC running WindowsXP 64 (Microsoft)

3.2.4 Platinization of Carbon Nanoelectrodes

Carbon nanoelectrodes were platinized in a solution of chloroplatinic acid H_2PtCl_6 (2 mM) in 0.1 M sulfuric acid. The reduction of Pt at the carbon nanoelectrode was induced by cycling the potential twice from - 1 to + 0.5 V, at a scan rate of 750 mV/s.

3.3 Results and Discussion

DCEs were fabricated with a high success rate (ca. 85%, based on more than 100 made) on the day of use, with approximately 3 min required per tip. A typical DCE (see Figure 2.1, panels B and C) consists of two planar semielliptical electrodes separated by a septum and surrounded by glass. The septum size and small surround of glass are typical for probes constructed from theta nanopipets by the laser pulling technique.[24, 25, 38]

Each electrode of a DCE was individually characterized using the steady-state currents for the one-electron oxidation of $FcTMA^+$ obtained from linear sweep voltammograms. Typical examples for each of the two electrodes of a single probe are shown in Figure 3.3A. As expected, the LSVs show a sigmoidal response. When coplanar electrodes are assumed, the different magnitude of the limiting currents for each electrode, within an individual probe, indicates that the electrodes are not the same size. Generally, the individual electrodes in a single probe may have slightly different sizes due to asymmetry in the individual barrel sizes in the pulled theta pipet.

This DCE was then used in the G/C mode, with the $FcTMA^{+/2+}$ redox couple. The potential of the generation electrode was swept for the oxidation of $FcTMA^+$ to $FcTMA^{2+}$, while the potential of the collection electrode was held constant at 0 V for the reduction of any $FcTMA^{2+}$ back to $FcTMA^+$. The resulting generation and collection currents are shown in Figure 3.3B. The generation current shows the typical sigmoidal shape; however, the magnitude of the limiting current is slightly larger than observed for the single-electrode response above, as the second electrode regenerates $FcTMA^+$, so providing positive redox feed-

back to the generator electrode. The collection current shows a similar sigmoidal shape, resulting from the change in local $FcTMA^{2+}$ concentration induced by the generator electrode. The ratio of collection current to generation current defines the collection efficiency, and this probe had a diffusion-limited collection efficiency of ca. 30%. This reasonable collection efficiency is achieved because the small distance between the two electrodes minimizes diffusional losses.

3.3.1 Nanoscale DCE Characterization

While nanoscale electrodes can be routinely fabricated,[39, 40] the resulting probe geometry is often difficult to determine precisely.[29] In principle, it is possible to determine the individual probe geometry for a DCE by SEM after experiments; however, this was found to be problematic due to crystallization of the redox species and supporting electrolyte on the probe. Practically, the estimation of probe geometry is usually achieved by using analytical expressions, or simulations, to relate the experimental current responses to electrode dimension, taking care to avoid pit falls due to nonplanar geometrical affects (especially recessed electrodes).[41-43] More complex geometries, such as the probes used herein, need custom FEM simulations to determine probe geometries from current measurements. A FEM model of the DCE was formulated so that the geometry only depended on the size of the electrode major axes and this allowed the geometry to be determined from only two current measurements.

We calculated the sizes of the nanoscale electrodes in the DCE used to record the data in Figure 3.3 (panels A and B), using the FEM model. First, the geometry was calculated from the diffusion-limited currents at the individual

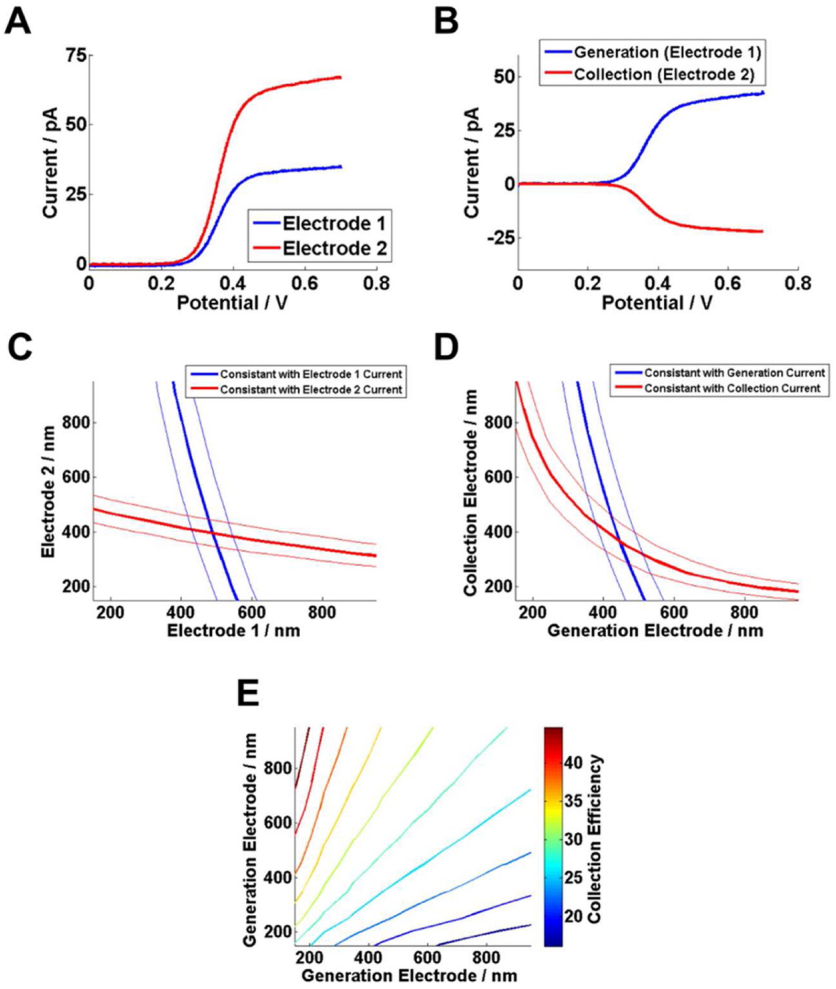

Figure 3.3: (A) LSVs (20 mV s^{-1}) for the oxidation of $FcTMA^{+}$ to $FcTMA^{2+}$ at each individual electrode in a nanoscale DCE, while the other electrode was unconnected. (B) LSV for generation (electrode 1) and corresponding collection current (electrode 2) for $FcTMA^{+}/FcTMA^{2+}$, as the potential of the generator electrode (x-ordinate value) was swept and the collector electrode potential was held at 0 V. (C) The geometry sets, for electrode 1 in blue and electrode 2 in red, calculated from a FEM model that can generate the single barrel currents. The two geometry sets are consistent with electrode 1 major axis radius 500 ± 50 nm and electrode 2 major axis radius 400 ± 25 nm (at the intercept). (D) The set of geometries, for electrode 1 in blue and electrode 2 in red, calculated from the FEM model that is consistent with the generation and collection currents. The two are self-consistent at electrode 1 major axis radius 450 ± 50 nm and electrode 2 major axis radius 400 ± 50 nm (at the intercept). (E) Collection efficiencies, from simulations, for a range of probe sizes.

electrodes (Figure 2A). The probe size (defined by the size of the major axes) consistent with the diffusion-limited current measured at electrode 1 is shown in blue in Figure 2C, while the probe size consistent with the measured limiting current for electrode 2 is shown in red. Note that for this model, the size of a particular electrode, as determined from its current, shows a weak dependence on the size of the other (unconnected) electrode because changing the size of the latter electrode changes the minor axis size (and also the septum and glass surround width). For example, a smaller unconnected electrode promotes more back diffusion and a slightly higher current at the active electrode. The point at which the two curves in Figure 3.3C intersect, 500 ± 50 nm for electrode 1 and 400 ± 25 nm for electrode 2, is the only possible probe geometry, constrained by the model assumptions, which could produce the two individual electrode currents.

The geometry of the probe can also be calculated from the diffusion-limited generation/collection currents, shown in Figure 3.3B. With electrode 1 generating $FcTMA^{2+}$ and electrode 2 collecting $FcTMA^{2+}$ (i.e., both electrodes active), the calculated probe size consistent with the measured generation current is shown in blue in Figure 3.3D, while the probe size consistent with the measured collection current is shown in red. Again, the point at which these two sets of electrode sizes intersect, the electrode 1 major axis of 450 ± 50 nm and electrode 2 major axis of 400 ± 50 nm was the geometry of the probe, constrained by the model assumptions, calculated from the generation/collection currents. It is evident that the size of electrode 1, from the two geometry calculations 500 ± 50 nm versus 450 ± 50 nm, is reasonably consistent, as is the size of electrode 2, 400 ± 25 nm versus 400 ± 50 nm.

This highlights that the G/C experiments are particularly sensitive to the

probe size. In addition, the calculated collection efficiency is shown in Figure 3.3E. This shows that probes with similar-sized electrodes have collection efficiencies of ca. 30%. A relative increase in generation electrode size compared to the collection electrode results in a decrease in collection efficiency, while decreasing the generator electrode size increases the collection efficiency.

3.3.2 SECM Measurements

DCEs were deployed in SECM to investigate their behavior, in G/C mode, close to the surfaces. With $FcTMA^+$ oxidation at one (generator) electrode and $FcTMA^{2+}$ reduction at the second (collector) electrode, DCEs were translated toward insulating (glass) and conductive (gold) surfaces using the IC-SECM mode.[32] With IC-SECM, the probe is oscillated normal to the surface (in this case with an amplitude of 32 nm at 70 Hz frequency), and damping of the oscillation amplitude is detected when the tip comes into physical intermittent contact with the surface. This mode provides a current-independent means of detecting when the tip and the substrate surface make contact, which is valuable for estimating the distance between the probe tip and the surface during the approach curve measurements.

The DCE generation and collection currents for approaches to glass and gold surfaces are shown in Figure 3.4 (panels A and B), respectively. The position at which the tip comes into contact with the surface is seen as a sharp drop in the tip position oscillation amplitude (Figure 3.4, panels C and D). For convenience, this point is assigned as a distance of 0 μm between the probe electrode and the surface, although in reality, imperfection in the probe alignment and geometry lead to nonzero distances between the active electrodes and the surface.[44]

When approaching the inert substrate, the generation current decreases, but interestingly, the collection current increases before dropping off when the tip is very close to the substrate. The transient increase in the collection current is because the substrate confines the generated species, $FcTMA^{2+}$, close to the electrodes, limiting diffusional losses, so leading to enhanced diffusional coupling between the two electrodes. However, once the tip gets much closer to the inert surface, the significant decrease in the generation current, due to the blocking effect of the substrate on the diffusion of $FcTMA^{+}$ to the generator, causes the collection current to decrease. On the other hand, Figure 3.4E clearly shows that the absolute collection efficiency increases as the distance from the substrate surface decreases. In this plot, the collection efficiency at a particular distance is normalized with respect to that measured in bulk solution.

The approach to a conducting substrate shows that the generation current increases with a decrease of the distance to the substrate (positive feedback),[45] while the collection electrode is in competition with the substrate and thus as the tip gets closer to the substrate, the current at this electrode drops. This competition increases with closer tip/substrate separation and so the collection efficiency decreases monotonically throughout an approach (Figure 3.4E). The data in Figure 3.4E highlights that the morphology of an SECM collection efficiency approach curve is hugely sensitive to the nature of the substrate, and this provides a route to functional imaging of surface processes, as we demonstrate below.

We used the FEM model to assess the approach curves. The sizes of the individual electrodes in the probes used for the approach curve experiments were calculated from the steady-state (bulk) generation and collection currents, as described above. For the approach to the insulating surface, the apparent probe

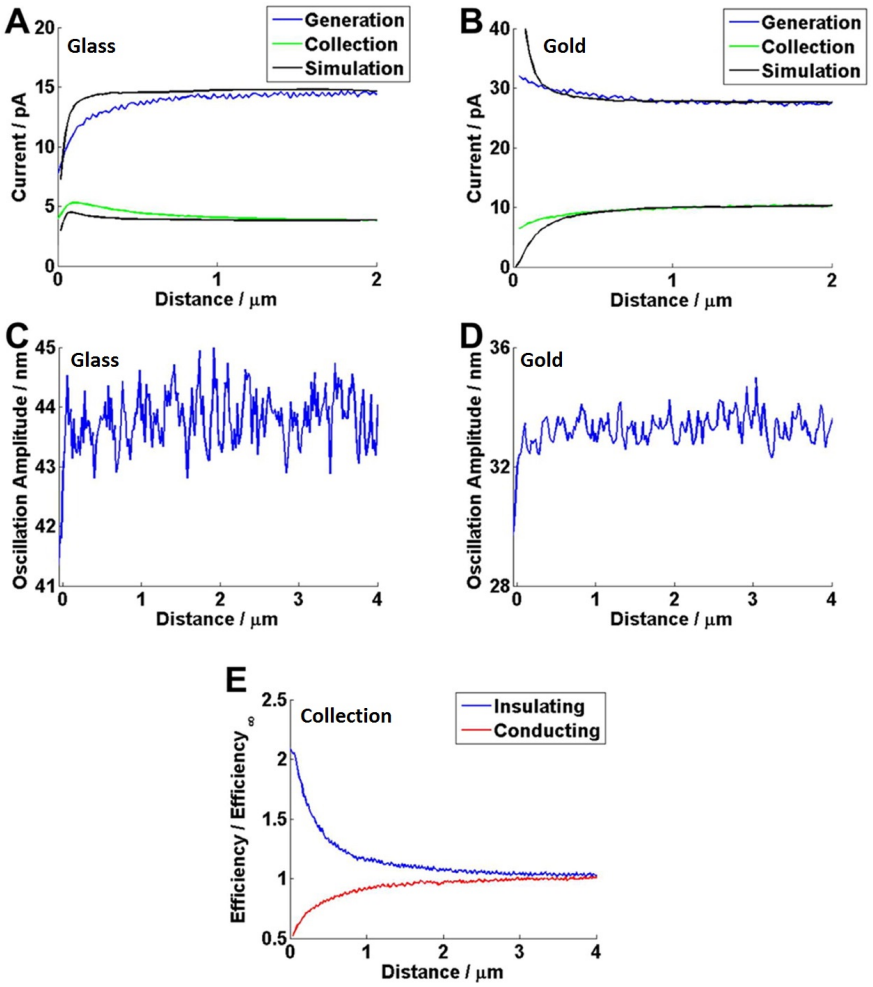

Figure 3.4: (A) Generation and collection currents during the approach of a DCE probe to an insulating (glass) substrate, with the results for a FEM simulation (generation electrode major axis size of 120 nm and collection electrode major axis size of 95 nm) of the same system. (B) Generation and collection currents, for an approach to a conducting (gold) substrate, with the results for a FEM simulation (generation electrode major axis size of 160 nm and collection electrode major axis size of 440 nm). (C and D) Probe oscillation amplitude, showing a sharp decrease that indicates probe contact with the surface, (A and B, respectively). (E) Experimental collection efficiencies (for A and B).

dimensions were defined by 120 nm for the generator electrode major axis and 95 nm for the collector electrode major axis, while for the approach to the conducting surface, the generator electrode major axis was 160 nm, and the collector electrode major axis was 440 nm. Simulation results for approach curves, with the probe perfectly aligned to the surface (which is an approximation as already discussed), to both insulating and conducting substrates were calculated and are shown in black in Figure 3.4 (panels A and B). These show the same topological features as observed in the experimental results, most obviously the increase in collection current when approaching an insulating substrate. However, quantitative differences are evident between the experimental and simulation results, particularly during the approach to the insulating substrate (Figure 3.4A). In this case, the decrease in experimental generator current is apparent at a distance which we would not expect based on the simulation. This suggests that the true probe geometry is larger than determined from the model, and that, in turn, the electrode is recessed. Such recessions are not uncommon in nanoscale electrodes,[29, 46] and quantitative analysis of approach curves is a powerful way of highlighting nonidealized electrode geometries.[41] While we could develop our model to account for misalignment of the probe with respect to the surface and nonideal geometry, this would introduce a number of extra independent parameters, which are not needed for the initial applications herein, in which we seek to demonstrate attributes of DCE generation-collection measurements in a semiquantitative fashion.

3.3.3 Probing Redox Reactions at Thylakoid Membranes

We demonstrate the use of generation-collection measurements to monitor the reactions of an artificial electron acceptor at thylakoid membranes during photosynthesis. The SECM configuration allowed the DCE to be placed close to, but not touching, a monolayer of thylakoid membranes. The DCE, operated in G/C mode, also allowed a flux of the artificial electron acceptor ($FcTMA^{2+}$) to be generated locally in a controllable manner and permitted the local flux of both $FcTMA^{2+}$ and $FcTMA^{+}$ to be measured concurrently, with good time resolution. The interaction of electrogenerated $FcTMA^{2+}$ with thylakoid membranes was investigated using the DCE shown in Figure 1C in the G/C mode, as illustrated in Figure 3.5A. The probe was placed over a sparse monolayer of thylakoid membranes (a typical surface coverage is indicated in the fluorescence image of Figure 3.5B) and approached in the dark to the point of maximum collection current, as shown in the approach curve in Figure 3.5C. Note that the morphologies of the generator and collector current approach curves are consistent with the thylakoid membrane presenting an inert surface, as discussed above. The probe was then held stationary while the sample was illuminated using the fluorescence microscope (at a wavelength of 470 nm with an intensity of 3.5×10^{16} photons s^{-1} cm^{-2} for a period of 30 s, and the generation and collection currents during this time were measured. Figure 3.5 (panels D and E) shows the relative change in the generation current and collection current during this period, respectively. Upon illumination, it is apparent that $FcTMA^{2+}$ is reduced to $FcTMA^{+}$ at the thylakoid membranes, as there is an increase in the magnitude of the generation current and a decrease in the magnitude of the collection current. Interestingly, a steady-state response is

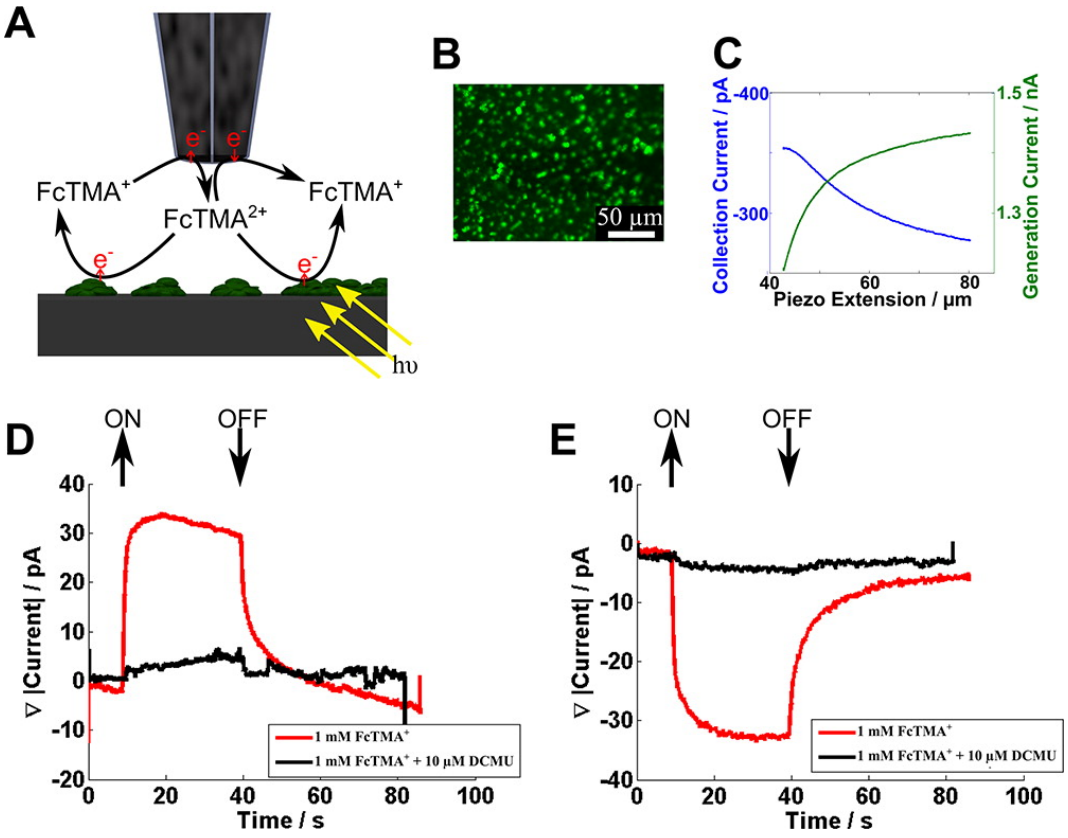

Figure 3.5: (A) Schematic of the DCE in the generation/collection mode, with the $FcTMA^{+/2+}$ couple, above a sparse monolayer of thylakoid membranes. (B) Fluorescence microscopy image of a sparse monolayer of thylakoid membranes, observed as green spots on the surface. (C) Approach curves for placing the DCE above the surface containing thylakoid membranes (probe size defined in text). (D) Generation current response as the monolayer of thylakoid membranes is illuminated with and without DCMU. (E) Collection current response as the monolayer of thylakoid membranes is illuminated with and without DCMU.

quickly reached, with a ca. 30 pA increase in the generation current and a corresponding ca. 30 pA decrease in the collection current. $FcTMA^{2+}$ reduction at the thylakoid membranes ceases immediately when the light is turned off, as evidenced by the return of the generation and collection currents to original values. This corresponds to a turnover rate of $FcTMA^{2+}$ to $FcTMA^{+}$ of ca. 2 x 10^{8} s^{-1}. An advantage of the DCE probe is that the electron acceptor is generated locally and the spatial resolution is correspondingly high, approximating to the tip size.

To confirm the $FcTMA^{2+}$ reaction with illuminated thylakoid membranes, the herbicide, 3-(3,4-dichlorophenyl)-1,1-dimenthylurea (DCMU), which blocks the linear electron transport pathway[36] was added. As observed in Figure 3.5 (panels D and E), the addition of 10 μM DCMU essentially entirely eliminated the light-mediated response. This confirms that $FcTMA^{2+}$ is reduced by a component of the photosynthetic electron transport pathway. Interestingly, we can exclude the possibility that $FcTMA^{2+}$ accepts electrons directly from PSII, as is the case, for example, with silicomolybdate because DCMU inhibits the electron transport pathway after this point.[36]

3.3.4 Thylakoid Membrane Imaging

A DCE in G/C mode was used to image a single thylakoid membrane. The probe (generator electrode major axis ca. 1700 nm and collector major axis ca. 700 nm) was placed directly above a single thylakoid membrane at a distance where the maximum collection current was detected (as above) and then scanned laterally across the sample at a constant height in the G/C mode. The sample was illuminated (470 nm, at 3.5 x 10^{16} photons s^{-1} cm^{-2}) during the scan to activate the

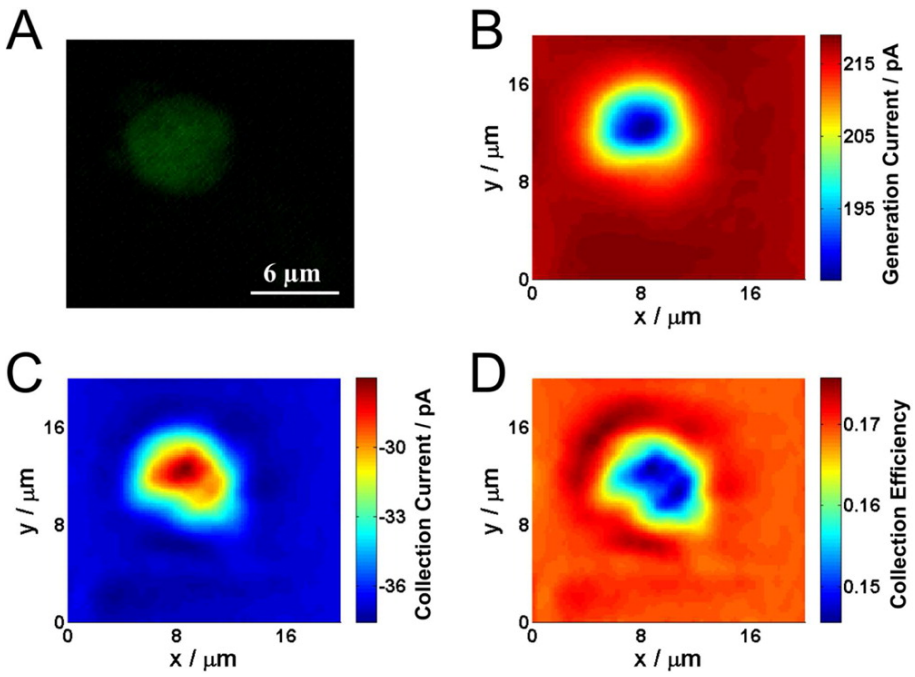

Figure 3.6: (A) Fluorescence image of a single thylakoid membrane. (B) Generation current ($FcTMA^+$ oxidation) image of the thylakoid membrane. (C) Collection current ($FcTMA^{2+}$ reduction) image of the thylakoid membrane. (D) Collection efficiency image of the thylakoid membrane. The electrochemical images were acquired over a period of 400 s.

photosynthetic response at the membrane.

A fluorescence image of the thylakoid membrane, due to the autofluorescence of chlorophyll, is shown in Figure 3.6A. This matches well with the electrochemical images of the thylakoid membrane, one from the generation current (Figure 3.6B) and one from the collection current (Figure 3.6C) obtained in a single image scan with a DCE. The decrease in generation current over the thylakoid membrane is predominantly the result of local topography features, which is expected as thylakoid membranes are typically 24 μm in height. The collection current also decreases over the thylakoid membrane. However, the collection effi-

ciency (Figure 3.6D) decreases over the thylakoid membrane. This is only possible over an active surface, as shown in the approach curves in Figure 3.4 and indicates that the thylakoid membranes are actively consuming the electrogenerated $FcTMA^{2+}$. The effect is very subtle and would be difficult to detect from a single probe SECM feedback measurement, not the least because of the convolution of activity and topography in such measurements and the fact that the activity of a single thylakoid membrane is low. Although the substrate generation/tip collection mode might allow the processes to be probed, this would require $FcTMA^{2+}$ in bulk solution and this mode is characterized generally by a significant loss of spatial resolution.[40, 44] In contrast, we see the degree of activity very readily in the collection efficiency image. Although a simple constant height SECM imaging technique was presented here a further important aspect of these probes is that one could use the response of one electrode to sense topography and the other to sense substrate activity.[22]

3.3.5 Platinization of Carbon Nanoelectrodes

Finally, we consider preliminary experiments that show DCEs can be easily and selectively modified, though with the selective deposition of Pt on one electrode while leaving the other one unmodified. Figure 3.7 in (panels A and B) shows CVs of 1 mM ferrocenemethanol oxidation in aerated solution, for the individual electrodes of a probe, before and after the selective deposition of Pt on one of the electrodes. The deposition of Pt dramatically changes the catalytic properties of the electrode toward oxygen reduction, as can be seen by the additional oxygen reduction current observed in the negative potential region of Figure 3.7B. However,

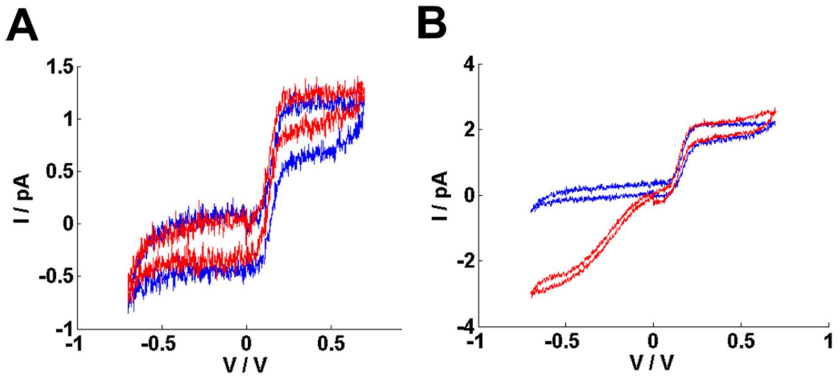

Figure 3.7: (A) CV for the oxidation of ferrocenemethanol at the first electrode in a DCE before (blue) and after (red) deposition of Pt on the second electrode. (B). CV at the second electrode in a DCE before (blue) and after (red) deposition of platinum on this electrode. Only the oxidation of ferrocenemethanol occurs on the carbon electrode, whereas an additional oxygen reduction wave is seen after Pt electrodeposition.

the deposition of Pt does not appreciably change the size of the electrode, as the ferrocenemethanol oxidation limiting current does not change noticeably with the Pt deposition. This highlights the possibility of using DCEs for electrochemical sensing which, with further developments, may allow multicomponent chemical analysis at the nanoscale.

3.4 Conclusions

DCEs are simple and quick to fabricate with a wide range of tunable electrode sizes. The probes are well suited to SECM experiments because of the relatively small total size of the end of the probe enabling close positioning to an interface, while the small interelectrode distance leads to high sensitivity.

For nanoscale DCEs, a FEM model was developed to assist in characterizing the probe size based on simple steady-state limiting current measurements. The electrode sizes were calculated from either single barrel $FcTMA^+$ oxidation currents or the G/C currents. This allowed us to estimate the apparent probe geometry from two different measurements and compare them. However, as highlighted in the approach curve measurements, the FEM model does not capture subtle geometric imperfections, such as protruding or recessed electrodes or slight misalignment of the probe. Nonetheless, these initial studies highlight that the probes can be used in a semiquantitative fashion and, if required, the morphology of approach curves could be further analyzed to provide additional information on these imperfections.

We have demonstrated that DCEs can be used to interrogate interfaces and surfaces with high sensitivity. DCEs were used to assess local changes in the $FcTMA^+$ and $FcTMA^{2+}$ flux during illumination of thylakoid membranes and in 2D imaging of a single thylakoid membrane. In both cases, subtle interactions of electrogenerated electron acceptors with the active surface were determined readily through the G/C response.

Further work to extract the geometry from current-based measurements could expand the quantitative capabilities of these probes. In addition, we have shown that individual probes within the DCE can be functionalized, as exemplified by selective deposition of Pt on one electrode while leaving the other one unmodified. Platinized nanoelectrodes have been shown to be promising probes for intracellular measurements.[47] DCEs may thus find applications as single-cell chemical sensors and other modifications are evidently realizable.

3.5 References

[1] Mirkin, M. V.; Fan, F.-R. F.; Bard, A. J. *J. Electroanal. Chem.* **1992**, 328, 4762.

[2] Mirkin, M. V.; Bard, A. J. *Anal. Chem.* **1992**, 64, 22932302.

[3] Bard, A. J.; Mirkin, M. V.; Unwin, P. R.; Wipf, D. O. *J. Phys. Chem.* **1992**, 96, 18611868.

[4] Zhou, J.; Zu, Y.; Bard, A. J. *J. Electroanal. Chem.* **2000**, 491, 22 29.

[5] Rodrguez-Lopez, J.; Alpuche-Aviles, M. A.; Bard, A. J. *J. Am. Chem. Soc.* **2008**, 130, 1698516995.

[6] Ahmed, S.; Shan, J.; Petrik, L.; Linkov, V. A. *Anal. Sci.* **2004**, 20, 12831287.

[7] Takahashi, Y.; Shevchuk, A. I.; Novak, P.; Murakami, Y.; Shiku, H.; Korchev, Y. E.; Matsue, T. *J. Am. Chem. Soc.* **2010**, 132, 10118 10126.

[8] Takahashi, Y.; Shevchuk, A. I.; Novak, P.; Babakinejad, B.; Macpherson, J. V.; Unwin, P. R.; Shiku, H.; Gorelik, J.; Klenerman, D.; Korchev, Y. E.; Matsue, T. *Proc. Natl. Acad. Sci. U.S.A.* **2012**, 109, 1154011545.

[9] Holt, K. B.; Bard, A. J. *Biochemistry* **2005**, 44, 1321413223.

[10] Pierce, D. T.; Unwin, P. R.; Bard, A. J. *Anal. Chem.* **1992**, 64, 17951804.

[11] Tsionsky, M.; Zhou, J.; Amemiya, S.; Fan, F.-R. F.; Bard, A. J.; Dryfe, R. A. W. *Anal. Chem.* **1999**, 71, 43004305.

[12] Amemiya, S.; Bard, A. J. *Anal. Chem.* **2000**, 72, 49404948.

[13] Kueng, A.; Kranz, C.; Mizaikoff, B. *Biosens. Bioelectron.* **2005**, 21, 346353.

[14] Matysik, F.-M. *Electrochim. Acta* **1997**, 42, 31133116.

[15] Barnes, E. O.; Lewis, G. E. M.; Dale, S. E. C.; Marken, F.; Compton, R. G. *Analyst* **2012**, 137, 10681081.

[16] Albery, W. J.; Hitchman, M. L. *Ring-Disc Electrodes*; Clarendon Press: Oxford, 1971.

[17] Slowinska, K.; Feldberg, S. W.; Majda, M. J. *Electroanal. Chem.* **2003**, 554555, 6169.

[18] Zhong, M.; Zhou, J.; Lunte, S. M.; Zhao, G.; Giolando, D. M.; Kirchhoff, J. R. *Anal. Chem.* **1996**, 68, 203207.

[19] Liljeroth, P.; Johans, C.; Slevin, C. J.; Quinn, B. M.; Kontturi, K. *Electrochem. Commun.* **2002**, 4, 6771.

[20] Fushimi, K.; Matsushita, K.; Hasegawa, Y. *Electrochim. Acta* **2011**, 56, 96029608.

[21] Yasukawa, T.; Kaya, T.; Matsue, T. *Anal. Chem.* **1999**, 71, 46374641.

[22] Isik, S.; Etienne, M.; Oni, J.; Blochl, A.; Reiter, S.; Schuhmann, W. *Anal. Chem.* **2004**, 76, 63896394.

[23] Gao, N.; Lin, X.; Jia, W.; Zhang, X.; Jin, W. *Talanta* **2007**, 73, 589593.

[24] Yang, C.; Sun, P. *Anal. Chem.* **2009**, 81, 74967500.

[25] Takahashi, Y.; Shevchuk, A. I.; Novak, P.; Zhang, Y.; Ebejer, N.; Macpherson, J. V.; Unwin, P. R.; Pollard, A. J.; Roy, D. D.; Clifford, C. A.; Shiku, H.; Matsue, T.; Klenerman, D.; Korchev, Y. E. *Angew. Chem., Int. Ed.* **2011**, 50, 96389642.

[26] Matsue, T.; Koike, S.; Abe, T.; Itabashi, T.; Uchida, I. *Biochim. Biophys. Acta* **1992**, 1101, 6972.

[27] Wong, D. K. Y.; Xu, L. Y. F. *Anal. Chem.* **1995**, 67, 40864090.

[28] Morton, K. C.; Morris, C. A.; Derylo, M. A.; Thakar, R.; Baker, L. A. *Anal. Chem.* **2011**, 83, 54475452.

[29] Nogala, W.; Velmurugan, J.; Mirkin, M. V. *Anal. Chem.* **2012**, 84, 51925197.

[30] Li, Y.; Bergman, D.; Zhang, B. *Anal. Chem.* **2009**, 81, 5496 5502.

[31] Cox, J. T.; Zhang, B. *Ann. Rev. Anal. Chem.* **2012**, 5, 253272.

[32] McKelvey, K.; Edwards, M. A.; Unwin, P. R. *Anal. Chem.* **2010**, 82, 63346337.

[33] McKelvey, K.; Snowden, M. E.; Peruffo, M.; Unwin, P. R. *Anal. Chem.* **2011**, 83, 64476454.

[34] McGeouch, C.-A.; Peruffo, M.; Edwards, M. A.; Bindley, L. A.; Lazenby, R. A.; Mbogoro, M. M.; McKelvey, K.; Unwin, P. R. J. *Phys. Chem. C* **2012**, 116, 1489214899.

[35] Patten, H. V.; Meadows, K. E.; Hutton, L. A.; Iacobini, J. G.; Battistel, D.; McKelvey, K.; Colburn, A. W.; Newton, M. E.; Macpherson, J. V.; Unwin, P. R. *Angew. Chem., Int. Ed.* **2012**, 51, 70027006.

[36] Hall, D. O.; Rao, K. K. *Photosynthesis*; Cambridge University Press: Cambridge, U.K., 1999.

[37] Shevela, D.; Messinger, J. *Biochim. Biophys. Acta* **2012**, 1817, 120812.

[38] Snowden, M. E.; Guell, A. G.; Lai, S. C. S.; McKelvey, K.; Ebejer, N.; OConnell, M. A.; Colburn, A. W.; Unwin, P. R. *Anal. Chem.* **2012**, 84, 24832491.

[39] Mirkin, M. V.; Nogala, W.; Velmurugan, J.; Wang, Y. P*hys. Chem. Chem. Phys.* **2011**, 13, 2119621212.

[40] Sun, P.; Laforge, F. O.; Mirkin, M. V. *Phys. Chem. Chem. Phys.* **2007**, 9, 802823.

[41] Sun, P.; Mirkin, M. V. *Anal. Chem.* **2007**, 79, 58095816.

[42] Wightman, R. M.; Wipf, D. O. In *Electroanalytical Chemistry;* Bard, A. J., Ed.; Marcel Dekker: New York, 1988; Vol. 15, pp 268 353.

[43] Bruckenstein, S.; Janiszewska, J. *J. Electroanal. Chem.* **2002**, 538539, 312.

[44] Lazenby, R. A.; McKelvey, K.; Unwin, P. R. *Anal. Chem.* **2013**, 85, 29372944.

[45] Kwak, J.; Bard, A. J. *Anal. Chem.* **1989**, 61, 12211227.

[46] Satpati, A. K.; Bard, A. J. *Anal. Chem.* **2012**, 84, 9498504.

[47] Wang, Y.; Noel, J.-M.; Velmurugan, J.; Nogala, W.; Mirkin, M. V.; Lu, C.; Guille Collignon, M.; Lematre, F.;Amatore, C. *Proc. Natl.Acad. Sci. U.S.A.* **2012**, 109, 1153411539.

Chapter 4

Fabrication and Characterization of Dual Function Nanoscale pH-Scanning Ion Conductance Microscopy (SICM) Probes for High Resolution pH Mapping

The easy fabrication and use of nanoscale dual function pH-scanning ion conductance microscopy (SICM) probes is reported. These probes incorporate an iridium oxide coated carbon electrode for pH measurement and an SICM barrel for distance control, enabling simultaneous pH and topography mapping. These pH-SICM probes were fabricated rapidly from laser pulled theta quartz pipets, with the pH electrode prepared by in situ carbon filling of one of the barrels by the pyrolytic decomposition of butane, followed by electrodeposition of a thin layer of hydrous iridium oxide. The other barrel was filled with an electrolyte solution and Ag/AgCl electrode as part of a conductance cell for SICM. The fabricated probes, with pH and SICM sensing elements typically on the 100 nm scale, were characterized by scanning electron microscopy, energy-dispersive X-ray spectroscopy, and various

electrochemical measurements. They showed a linear super-Nernstian pH response over a range of pH (pH 2-10). The capability of the pH-SICM probe was demonstrated by detecting both pH and topographical changes during the dissolution of a calcite microcrystal in aqueous solution. This system illustrates the quantitative nature of pH-SICM imaging, because the dissolution process changes the crystal height and interfacial pH (compared to bulk), and each is sensitive to the rate. Both measurements reveal similar dissolution rates, which are in agreement with previously reported literature values measured by classical bulk methods.

4.1 Introduction

The measurement of local pH is hugely valuable in explaining complex interfacial reactions, such as corrosion,[1, 2] metal deposition,[3, 4] and acid-base dissolution,[5, 6] all of which produce or consume protons and alter the pH near an interface. Additionally, many biological processes result in either intracellular[7, 8] or extracellular[9] pH changes, and the quantitative measurement of these pH changes with high spatial resolution would aid in understanding the mechanisms involved.

While local pH can be visualized using optical techniques such as wide field fluorescence microscopy[9] and laser scanning confocal microscopy,[10] pH is commonly measured with electrodes. When deployed as the tip in scanning electrochemical microscopy (SECM), these electrodes have enabled the measurement of pH with high spatial resolution at interfaces.[11-14] The scale on which pH electrodes can be made has advanced in recent years to the micro[15, 16] and nano scale.[17, 18]

SECM pH probes employing a variety of metal/metal oxides have been reported previously.[15, 19-21] Iridium oxide based pH ultramicroelectrodes have proven particularly popular for spatially resolved pH measurements in SECM, owing to their fast response time; long term stability over a wide range of pHs, temperatures, and pressures; all-solid format; and capability for miniaturization.[15, 22, 23] Iridium oxide pH electrodes have been prepared by either electrochemical oxidation,[22] thermal decomposition,[24] and sputter deposition[25] of iridium metal or by the electrodeposition of iridium oxide from alkaline solutions of iridium salts.[23, 26] Wipf et al. used a microscopic pH electrode produced by the deposition of iridium oxide onto carbon fiber microelectrode (5.9 μm radius) to map pH changes near a platinum electrode during hydrogen evolution and for monitoring the pH change

associated with the oxidation of glucose by glucose oxidase immobilized onto a carbon microelectrode.[15]

Hitherto, pH probes used in SECM have typically been on the several micrometers scale or larger, and consequently, constant height (conventional) SECM scanning protocols have been used (i.e., without positional feedback). For high resolution pH mapping, nanoscale probes are mandatory, and these need to be placed close to the interface of interest.[27] This demands the use of positional feedback SECM, particularly for samples with large topographical features.

Scanning ion conductance microscopy (SICM) has proven particularly powerful for topographical imaging of intricate surface geometries, including living cells.[27, 28] SICM uses a nanopipet filled with an electrolyte, containing a quasi-reference counter electrode, QRCE (e.g., Ag/AgCl), as the scanning probe. A potential is applied between this electrode and an external QRCE, placed in the bulk solution, and the resulting ionic conductance current provides a (feedback) signal for distance control. Various SICM-based positioning strategies have been developed over the years to expand the range of substrates open to study. Moreover, the technique has been combined with complementary techniques including SECM[29-32] and near field scanning optical microscopy to enhance the information content.[33]

Herein, we present an extremely quick and simple method to fabricate a hybrid pH-SICM probe, with an iridium oxide coated electrode for pH sensing and an SICM barrel for distance control. This report advances combined SECM-SICM[29] from amperometry/voltammetry to potentiometric imaging. pH-SICM probes were fabricated by the pyrolytic deposition of carbon into one of the barrels of a laser-pulled, sharp-point quartz theta pipet, followed by electrodeposition

of hydrous iridium oxide to make it pH sensitive, with the open barrel forming part of the conductance cell for SICM measurement. The electrode size could be tuned by altering the pipet pulling parameters, but pH electrodes employed herein were typically on the 100 nm scale. The pH-SICM probes were employed for simultaneous mapping of pH and topography of a calcite microcrystal during dissolution to demonstrate their suitability for quantitative high spatial resolution measurements at surfaces and interfaces. This is an interesting system because the crystal size changes during dissolution, which can be traced by the topographical response, while also determining the local interfacial pH. This provides two routes to determine the dissolution kinetics, which we show are consistent with each other. Furthermore, measurements of an entire microcrystal is topographically demanding, and for this study we implemented pH-SICM in both a hopping mode[30, 34] and a constant separation mode,[31] to demonstrate the versatility of the technique.

4.2 Materials and Methods

Materials and reagents and the method for the preparation of calcite microcrystals, together with instrumentation details, employed for this study were described in chapter 2.

4.2.1 Fabrication and Characterization of pH-SICM Probes

The pH-SICM probes were fabricated by a two-step process. Briefly, in the first step, a quartz theta pipet (o.d. 1.2 mm, i.d. 0.90 mm, Intracel) was pulled in a laser puller (P-2000, Sutter Instruments) to a sharp point. One of the pipet barrels

was closed by using Blu-Tack (Bostik) and butane was passed through the other barrel, via tubing, under an argon atmosphere.[29] The tip of the probe was heated with a butane torch, typically for 35 s, to pyrolytically deposit carbon from the butane, as illustrated in Figure 4.1A, producing an extensive filling of one barrel as shown in Figure 4.1B.

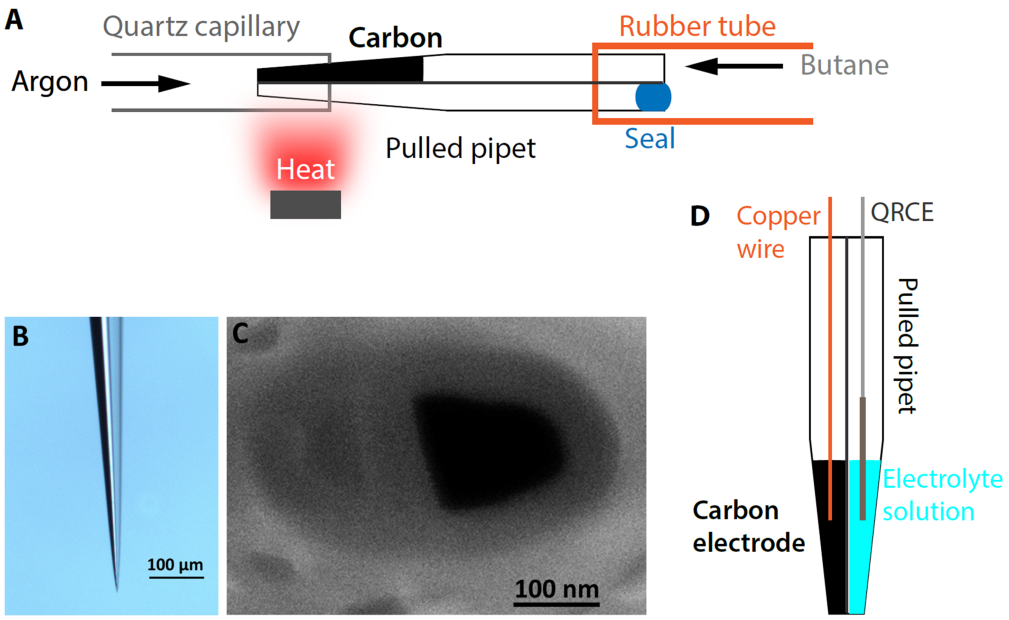

Figure 4.1: (A) Schematic of the carbon deposition step for the fabrication of pH-SICM probes. One barrel of a pulled theta pipet was closed using Blu-Tack, and butane was passed through the other open barrel and pyrolyzed using a hand-held butane torch under an argon atmosphere.[29] (B) Optical micrograph (side view) of a typical nanoscale pH-SICM probe after carbon deposition in one barrel. The carbon deposited barrel (left) is seen in black, along with the transparent open channel (right). (C) SEM micrograph (end view) of the tip of a typical nanoscale SICM-pH probe before electrodeposition of iridium oxide, with the carbon-filled barrel on the left and the open channel on the right. (D) Schematic representation of a pH-SICM probe.

Field-emission scanning electron microscopy (FE-SEM, Supra 55-VP, Zeiss) of a typical pH-SICM probe after carbon deposition is shown in Figure 4.1C. A range of electrode sizes, between 40 nm and 10 μm radius (overall of the entire probe), were easily constructed by changing the laser pulling parameters during fabrication. Herein, we focus on probes with a size of ca. 100 nm diameter for each barrel (SECM and SICM). An electrical connection was established by inserting a copper wire through the top end of the pipet barrel to make a back contact with the carbon layer (Figure 4.1D).

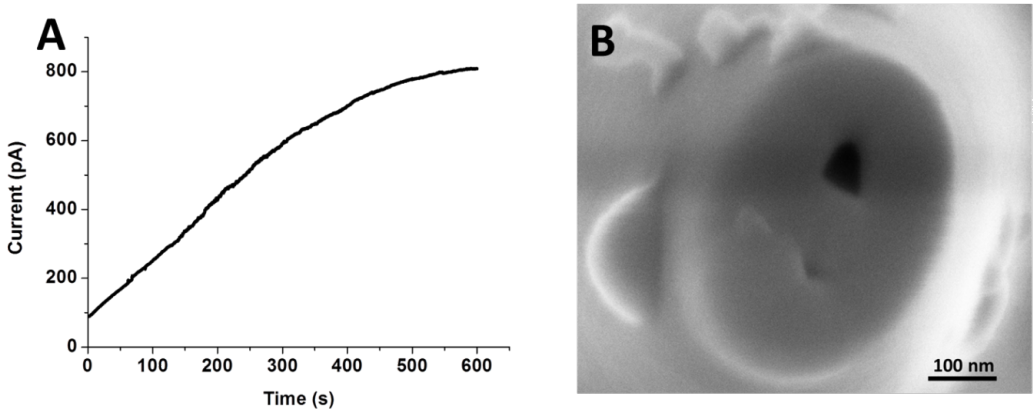

Figure 4.2: Electrodeposition and characterization of an iridium oxide pH nanoelectrode in the pH-SICM probe. (A) Current-time curve for the anodic electrodeposition of iridium oxide on a carbon nanoelectrode. (B) FE-SEM micrograph of the end of a tip of a typical nanoscale pH-SICM probe after electrodeposition; the light region in the bottom half of the solid electrode.

In the second step, electrodeposition of an iridium oxide film onto the deposited carbon layer was performed using the deposition solution described in Chapter 2.[26, 35] A potential of 0.68 V versus an Ag/AgCl (0.1 M KCl) QRCE was applied for 600 s to produce a hydrated iridium oxide film. Figure 4.2A shows

a typical current-time plot for anodic electrodeposition of iridium oxide. An FE-SEM micrograph of the end of a tip of a typical nanoscale pH-SICM probe after electrodeposition is shown in Figure 4.2B. The presence of iridium oxide after electrodeposition was confirmed by energy-dispersive X-ray spectroscopy (EDX) using a Zeiss Supra55VP field emission (FE)-SEM as well as by cyclic voltammetry. The fabricated pH electrodes were initially calibrated in various pH solutions by measuring the open-circuit potential at the pH electrode versus an Ag/AgCl QRCE, using a home-built voltage follower. The home-built voltage follower incorporated a unity gain input buffer stage using an AD549L amplifier (Analog Devices Inc.) mounted on PTFE spacers to minimize leakage currents. For ultrasmall potentiometric sensors, it is important to minimize the input bias current,(36, 37) and in the measurement device we used, the input bias of the buffer stage was ca. 40 fA with an input resistance of 1 x $10^{15}\Omega$. Stable continuous imaging over at least 3 h was achievable. To validate the calibration, the response of the pH-SICM probes was checked after each scan by titrating the solution of interest with 1 M HCl and comparing the potential response of the pH-SICM probe directly to that of a commercial glass pH electrode (Metler Toledo International Inc.). For imaging measurements the unfilled SICM barrel was filled with 0.01 M KCl solution, and a single Ag/AgCl QRCE was inserted into it.

4.2.2 pH-SICM Measurement Protocol

A 350 mV bias was typically applied between the Ag/AgCl electrode inside the SICM barrel and the QRCE in the bulk solution, and a sinusoidal wave to create a 60 nm peakpeak amplitude (280 Hz) was applied to the z position of the probe.

The resulting AC magnitude, i_{AC}, measured via the lock-in amplifier, was used to achieve close positioning of the probe to the sample and to maintain the height of the electrode from the surface as is standard in SICM;[29, 30, 38] this was set on the basis of the probe size. For the probe sizes mentioned herein, an i_{AC} of 9 pA was used as the set point for constant distance(31) and hopping,[29, 30, 34] pH-SICM imaging.

4.2.3 Simulations and Modeling

The dissolution of calcite is strongly pH dependent and this process increases the local pH, at the calcite water interface.[39-40] Plummer et al[41] proposed that the following three reactions occur simultaneously on the calcite surface[39,41]

$$CaCO_{3(s)} + H^{+}{}_{(aq)} \rightleftharpoons Ca^{2+}{}_{(aq)} + HCO_3^{-}{}_{(aq)} \quad (1)$$

$$CaCO_{3\ (s)} + H_2CO_{3\ (aq)} \rightleftharpoons Ca^{2+}{}_{(aq)} + 2HCO_3^{-}{}_{(aq)} \quad (2)$$

$$CaCO_{3\ (s)} + H_2O_{\ (l)} \rightleftharpoons Ca^{2+}{}_{(aq)} + HCO_3^{-}{}_{(aq)} + OH^{-}{}_{(aq)} \quad (3)$$

A three-dimensional finite element method (FEM) model, relevant to the calcite microcrystal and dissolution conditions used in the study, was developed to estimate the surface pH and dissolution rate. This mass transport model prescribed the calcite microcrystal geometry in an aqueous solution under dissolution conditions (undersaturated solution).

The calcium carbonate aqueous solutions, which are open to the atmosphere, in the presence of a calcite crystal can be described by the equilibria in Table 4.1. A mass transport model was designed that mimicked the calcite micro-

crystal geometry in an aqueous solution, implementing these equilibria. Under the conditions of our experiment, the process described by equation (3) dominates.

Table 4.1: Equilibria data for the calcite-H_2O system open to the atmosphere.[42]

Equation No	**Reactions**	**pK**
4	$CO_2 + H_2O \rightleftharpoons H_2CO_3$	1.466
5	$H_2CO_3 \rightleftharpoons H^+ + HCO_3^-$	6.351
6	$HCO_3^- \rightleftharpoons H^+ + CO_3^{2-}$	10.330
7	$CaHCO_3^+ \rightleftharpoons Ca^{2+} + HCO_3^-$	1.015
8	$CaCO_{3\ (aq)} \rightleftharpoons Ca_2^+ + CO_32^-$	3.2
9	$H_2O \rightleftharpoons OH^- + H^+$	13.997

The basic geometry for the model is shown in Figure 4.3. Simulations were carried out with ca. 1,000,000 tetrahedral mesh elements. The mesh resolution was defined to be finest near the surface of the crystal, which are boundaries 7- 11. Simulations of varying mesh density were also performed (not reported) to ensure a fine enough mesh was used for the model. Mass transport occurs predominantly by diffusion, for which the following equation was solved:

$$D_\mathrm{j} \nabla\ c_\mathrm{j} + R_\mathrm{j} = 0 \qquad (10)$$

where D_j is the diffusion coefficient and c_j is the concentration of species j, R_j is a kinetic term representing the loss or formation of species j defined by the equilibriation reactions, as described by activity corrected mass action rate equations.[43] The equilibrium constant values used herein are illustrated in Table 4.1 (before activity correction). The diffusion coefficients of the individual species

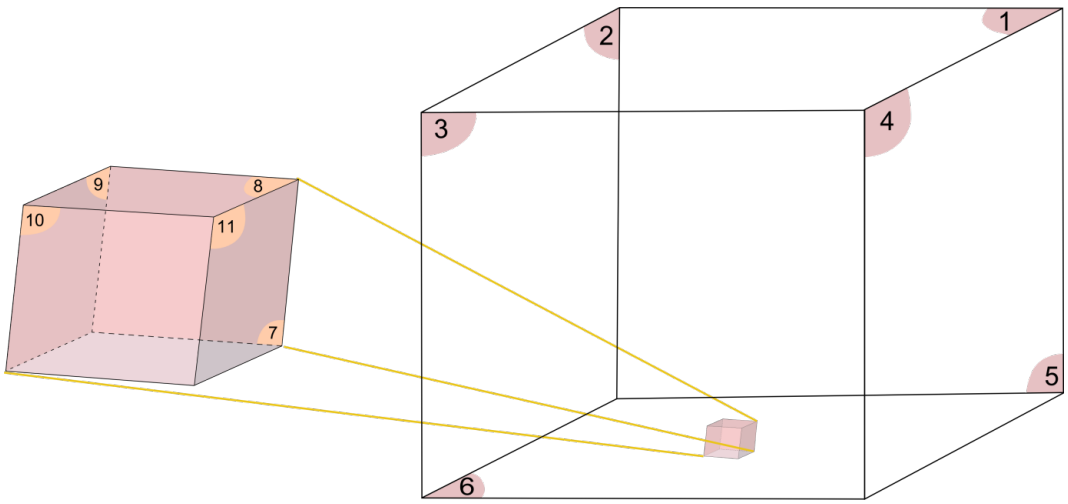

Figure 4.3: A schematic of the FEM model showing the calcite crystal (left). The bulk solution consists of a cube with a dimension of $30l$. The boundaries are numbered according to the constraints listed in text. The crystal dimensions are length of the crystal l, width of the crystal w, height of the crystal h.

can be considered to be constant over the spatial domain investigated; these values are presented in Table 4.2.

The boundary conditions applied to the model, as illustrated in Figure 4.2, are as follows. Boundaries 1-5 are at a considerable distance away from the crystal (30 x the largest dimension of the crystal), so they can reasonably be considered as bulk solution. Thus, they are constrained by a bulk concentration condition. Boundaries 1-5:

$$c_j = c_{j,\,bulk}\ 0 \tag{11}$$

where $c_{j,\,bulk}$is the bulk concentration governed by the equilibrium.[12] The equilibrium concentrations were calculated using CO_2 partial pressure $P_{CO_2} = 0.039\%$ atm, and the solution pH = 6.85, which was measured experimentally. Boundary

Table 4.2: Diffusion coefficient values of various species used in the FEM model.[44]

Species	Diffusion coefficient ($10^{-9}m^2s^{-1}$)
Ca^{2+}	0.792
H^+	9.311
OH^-	5.273
K^+	1.957
Cl^-	2.032
$CaHCO_3^+$	1.083
HCO_3^-	1.185
H_2CO_3	1.185
CO_3^{2-}	0.923

6 is constrained by a no-flux condition, to represent the unreactive surface of the glass substrate.

Boundary 6:

$$n.(D_j \nabla c_j) = 0 \tag{12}$$

where n is the inward unit vector normal to the boundary. Boundaries labelled 7-11 represent the dissolving crystal faces on which a flux of protons, calcium and bicarbonate ions were imposed; the equations satisfied on these boundaries are as follows:

Boundaries 7 - 11:

$$n.(DCa^{2+} \nabla cCa^{2+}) = J_{surf} \tag{13}$$

$$n.(D_{HCO_3^-} \nabla c_{HCO_3^-}) = J_{surf} \quad (14)$$

$$n.(D_{OH^-} \nabla c_{OH^-}) = J_{surf} \quad (15)$$

where J_{surf} is the dissolution flux at the crystal surface.

A plot of average surface pH obtained from FEM simulations using different J_{surf} values (Figure 4.4), was used to calculate the dissolution rate associated with the average surface pH recorded on the calcite microcrystal during dissolution.

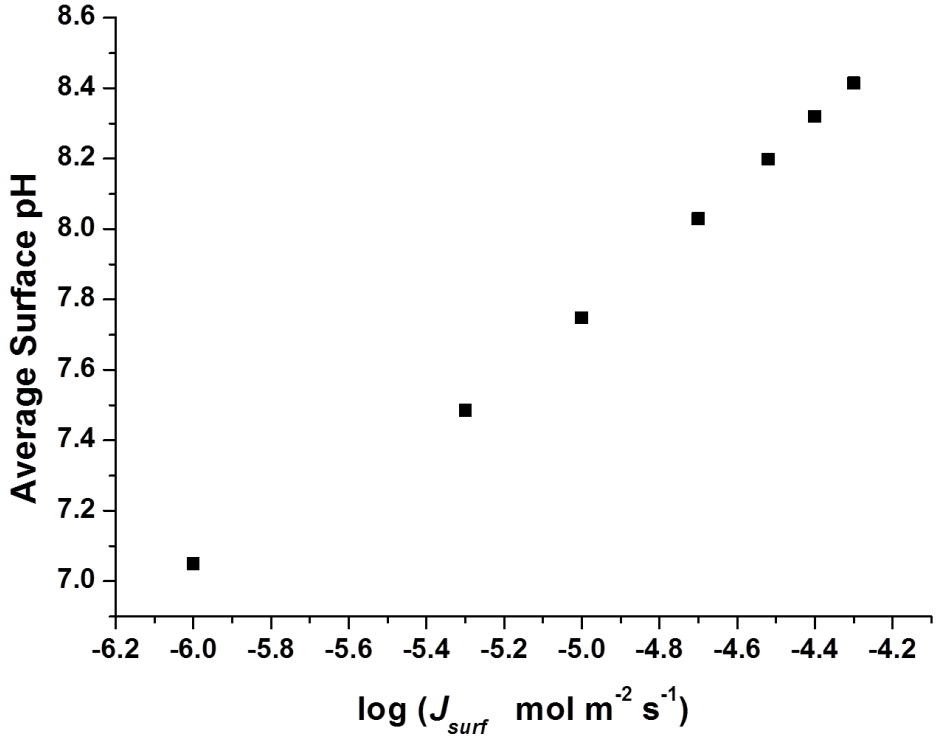

Figure 4.4: Relationship between the average interfacial pH (100 nm from the calcite microcrystal surface) and $\log(J_{surf})$ calculated by the FEM simulation.

All FEM modelings were performed using Comsol Multiphysics 4.3a (Com-

sol AB, Sweden) using a PC running 64 bit Windows 7.

4.3 Results and Discussion

4.3.1 Fabrication and Characterization of pH-SICM Probes

The pH-SICM probes were quickly and easily fabricated with a high success rate (80%, based on approximately 150 probes) on the day of use. The anodic electrodeposition of iridium oxide films onto the carbon nanoelectrode was achieved amperometrically using a constant-potential of 0.68 V; Figure 4.2A shows a typical current-time (*i*-*t*) curve. The deposition reaction responsible for iridium oxide formation on the electrode is[26, 35]

$$[Ir(COO)_2(OH)_4]^{2-}{}_{(aq)} + 2OH^- \rightarrow [IrO_2(OH)_2\ .2H_2O]_{(s)} + 2CO_2 + 2e^- \qquad (16)$$

Assuming 100% faradaic efficiency, the total amount of iridium oxide electrogenerated can be calculated by integrating the area under the *i*-*t* curve and was found to be ca. 1.3 pmol or, equivalently, 0.30 ng. Figure 4.2B shows the FE-SEM image of a pH-SICM electrode after electrodeposition. No new geometrical features are observed, compared to Figure 4.1C, suggesting that not all of the iridium oxide electrogenerated is retained on the carbon electrode.

However an energy-dispersive X-ray (EDX) spectrum recorded on the tip of a pH-SICM probe, after electrodeposition of iridium oxide showed a characteristic X-ray emission with 0.198 keV energy (Figure 4.5) confirming the successful electrodeposition of iridium onto the pH-SICM probe.

Further confirmation of the successful deposition of iridium oxide came from cyclic voltammetry (CV) of the pH probe, such as the response shown in Figure

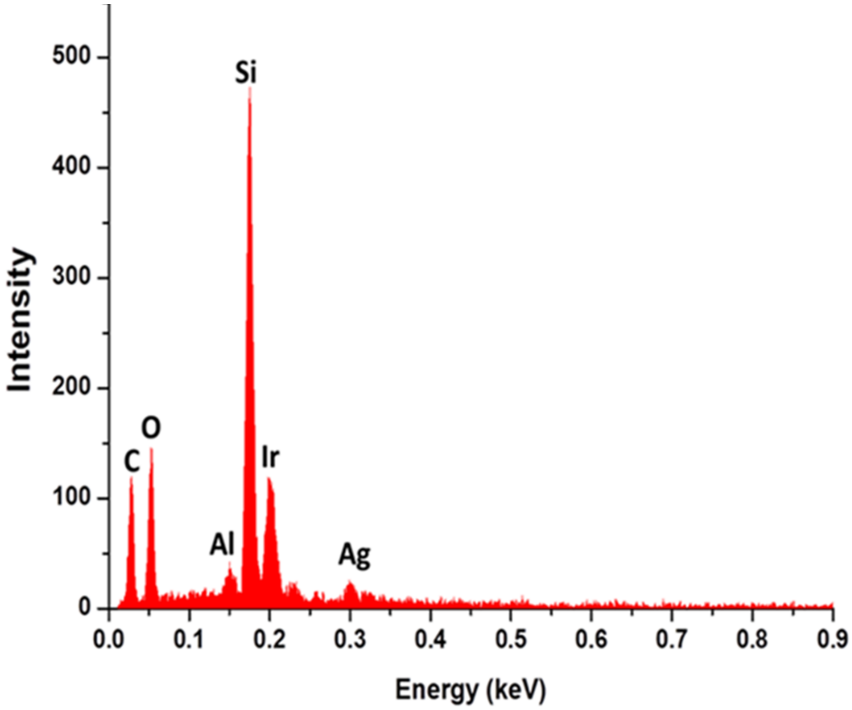

Figure 4.5: Energy-dispersive X-ray spectrum of a pH-SICM probe showing the characteristic iridium emission at 0.198 ekV.

4.6A, recorded between -0.4 V and 1 V in 0.5 M H_2SO_4 at a scan rate of 0.1 V s^{-1}. An anodic peak corresponding to the oxidation of Ir(III) to Ir(IV) and a cathodic peak corresponding to the reduction of Ir(IV) back to Ir(III) were observed in the CV with a similar peak potential, ca. 0.45 V on the forward and reverse waves, as reported previously,[15, 26] confirming the presence of iridium oxide. The quantity of electroactive iridium oxide on the carbon electrodes was estimated from the time integral of the cathodic peak. For the case in Figure 4.5A, this was ca. 0.1 pg (8 x 10^{-15} cm^3), suggesting the formation of a thin layer of iridium oxide on top of the carbon electrode.Iridium oxide potentiometric electrodes are known to exhibit a super-Nernstian pH response, with slopes varying from -59 to -90 mV per pH

unit at room temperature.[23] This has been attributed to a rather complex redox process governing the potentiometric response:[15, 26]

$$2[IrO_2(OH)_{2-x}\ (2+x)H_2O]^{(2-x)-} + (3-2x)H^+ + 2e^- \rightleftharpoons [Ir_2O_3(OH)_3\ \ 3H_2O] + 3H_2O \qquad (17)$$

Figure 4.6B shows a typical calibration curve for a nanoscale pH probe, where a slope of 79 ± 2 mV/pH was obtained over pH range 2-11, which is within the range seen with larger electrodes.[15, 23, 26] This was typical of more than 70% of ca. 120 nanoscale electrodes that were fabricated and tested. The pH-SICM probes produced a stable response over at least 3 h of continuous imaging, but their long-term stability was not addressed in this study since probes were fabricated on the day of use.

4.3.2 pH Mapping of Calcite Dissolution

The dissolution of calcite is strongly pH-dependent, and this process increases the local pH at the calcite/water interface.[39-41] The pH-SICM probe was used to map the interfacial pH and changes in crystal size that occurred during calcite microcrystal dissolution. This served to illustrate the dual capability of these probes: topography mapping combined with simultaneous local pH measurements.

For mapping of an entire calcite microcrystal during dissolution, we implemented a hopping mode similar to that reported previously for SICM.[30, 33] Thus, a series of approach curves that stopped upon reaching a specific ac set point, signifying a particular (close) distance from the surface was used to create an image. Briefly, the probe was approached to the calcite microcrystal at a speed of

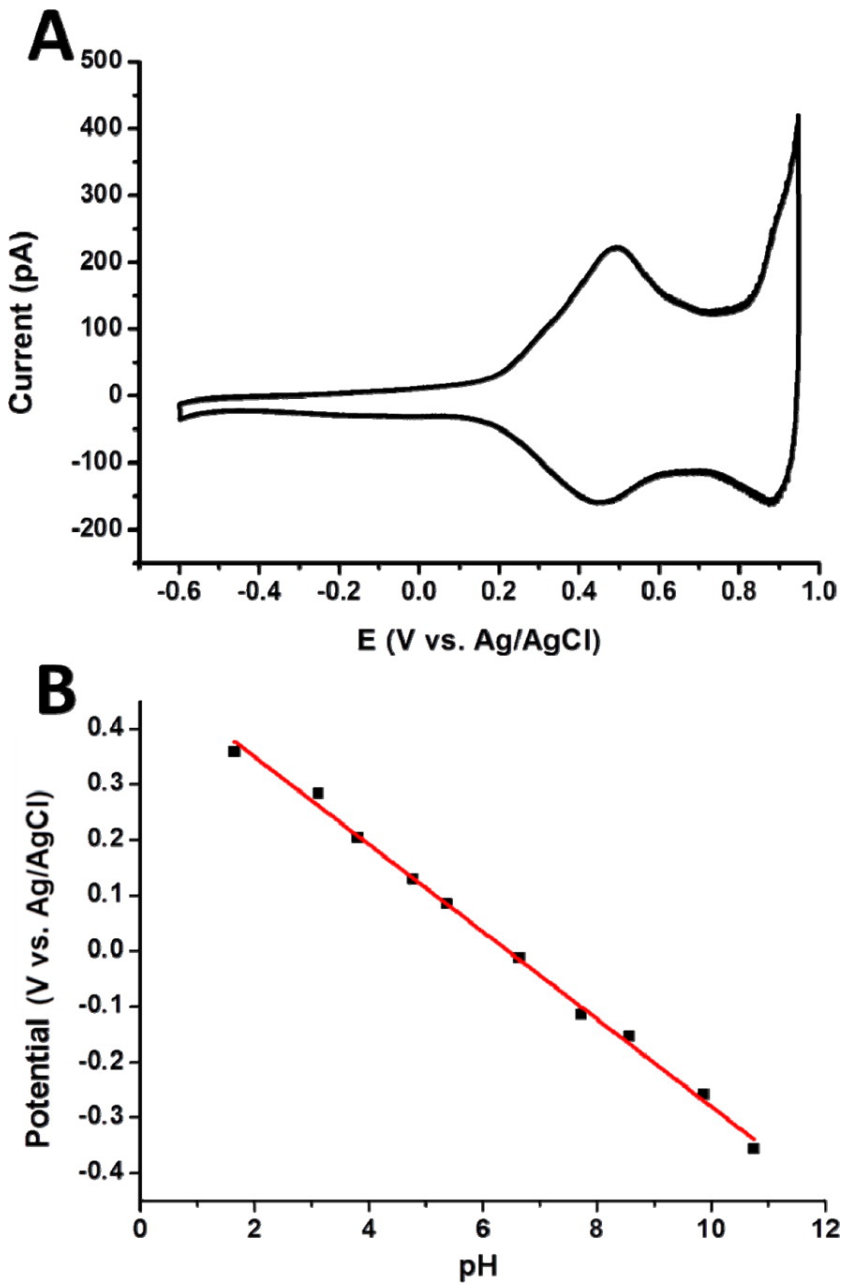

Figure 4.6: Characterization of the iridium oxide sensing element in a pH-SICM probe. (A) Cyclic voltammogram of the iridium oxide film after electrodeposition on the carbon electrode of a nanoscale pH-SICM probe; 0.5 M H_2SOtextsubscript4, scan rate 0.1 V s^{-1}. (B) Potential-pH calibration of a typical nanoscale pH-SICM probe.

0.2 μm s^{-1} while the ac component of ionic current, i_{AC}, was monitored during the approach. The pH was recorded simultaneously as a function of z-position (normal to the substrate). As soon as the value of i_{AC}exceeded the set point, the probe was quickly withdrawn to 25 μm, moved to a new x-y pixel (in the plane of the substrate) to start a new measurement cycle. For the data reported herein, the separation between x-y pixels was 10 μm over an area of 90 μm x 90 μm.

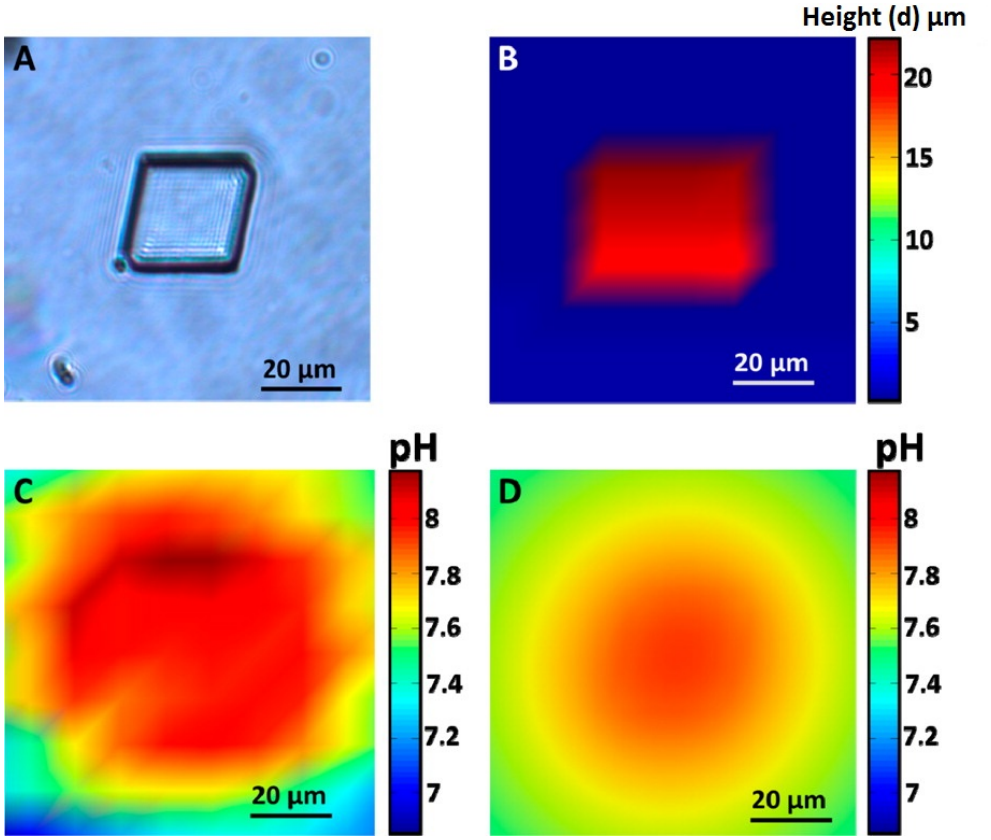

Figure 4.7: Topography and pH mapping of a calcite microcrystal. (A) Optical micrograph of the calcite microcrystal. (B) SICM topography image of calcite microcrystal. (C) pH map close to (100 nm from) the calcite microcrystal and glass surface recorded simultaneously with topography (bulk pH 6.85). (D) FEM model of the pH distribution close to (100 nm from) the calcite microcrystal and supporting glass substrate for a dissolution flux of 1.6 x 10^{-9} mol cm^{-2} s^{-1}.

An optical micrograph of a typical calcite microcrystal, in 0.01 M KCl, obtained directly on the experimental setup, is shown in Figure 4.7A, and the corresponding 3-D topography map recorded by the pH-SICM probe is shown in Figure 4.7B. This SICM image is seen to match very well with the optical image, with the advantage that the SICM image provides information of the crystal height as well as the lateral dimensions. The pH map corresponding to the distance of closest approach from the surface (estimated as 100 nm, from the magnitude of i_{AC}[38]) is shown in Figure 4.7C. As expected under dissolution conditions, a dramatic increase in pH was observed near the microcrystal, with the pH reaching values of ca. 7.9 $\pm$ 0.1 close to the microcrystal surface compared to a bulk value of ca. 6.85 in this particular case.

A three-dimensional FEM model, describing calcite microcrystal dissolution, was used to predict the pH on the crystal surface for different dissolution fluxes. The pH image over the calcite microcrystal and surrounding surface shown in Figure 4.7D corresponds to dissolution with an interfacial flux of 1.6 x 10^{-9} mol cm^{-2} s^{-1} at the calcite/solution interface; yielding a pH 7.94, in good agreement with the surface pH recorded during the scan.

High resolution images in constant distance mode were recorded as a series of line scans over a scan area of 20 μm x 20 μm with a line scan every 1 μm, each line comprising 1559 points (each the average of 512 potential measurements). The scan rate employed was 1 μm s^{-1}, and the tip/crystal distance for the probe size used was ca. 100 nm, corresponding to the set-point employed.[36] Surface features resembling the edge of a calcite hillock[48, 49] were observed in the topographical map, demonstrating the feasibility of high resolution topography imaging using these pH-SICM probes. To quantify the dissolution rate, two successive scans

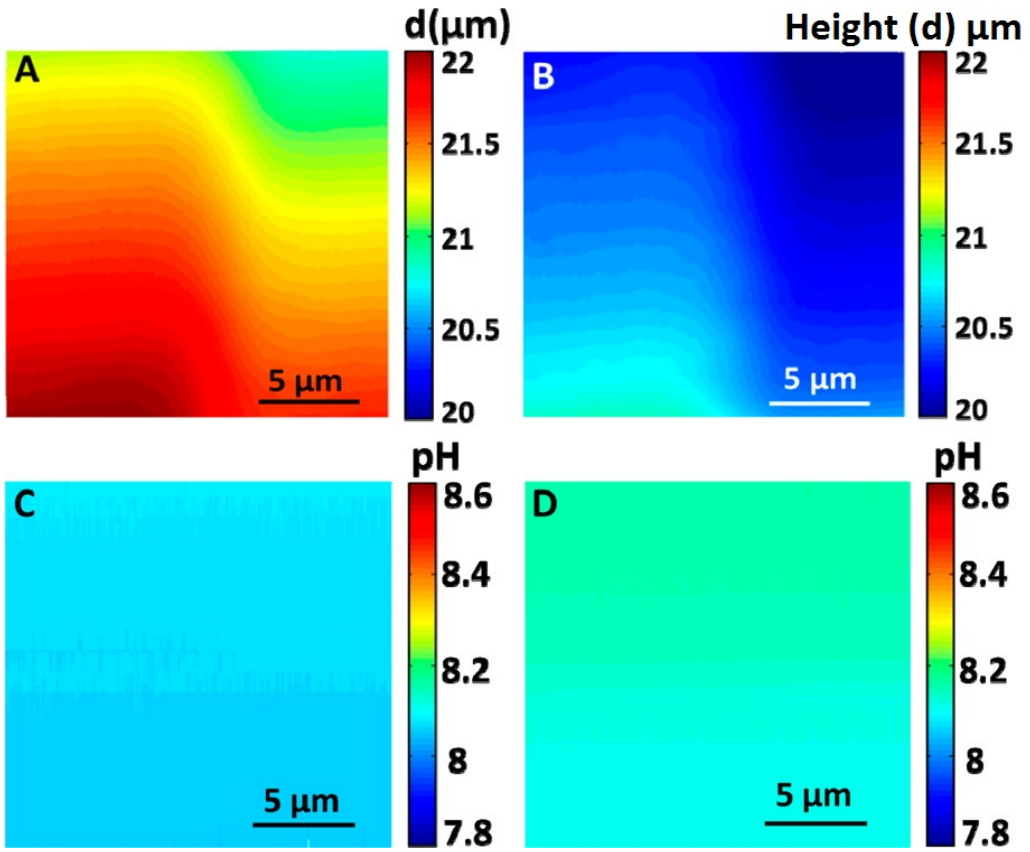

Figure 4.8: Simultaneous topography (A and B) and pH (C and D) images of calcite crystal surface recorded during two constant height electrochemical scans (bulk pH 6.85). Images B and D were recorded 20 min after images A and C.

were performed on the calcite microcrystal surface, and the change in crystal height between each (Figure 4.8, panels A and B) was determined. The two scans were performed in the same area with each of the lines in the second scan carried out 1200 s after those in the first scan. Between the two consecutive scans, an average height difference of 1.1 ± 0.1 μm was observed (for the scanning conditions employed, the effect of thermal drift on topography measurement[47] was less than 0.1 μm, determined by repetitively imaging a glass surface) for an area of 400 μm^2

of the crystal surface, suggesting a dissolution rate of 2.6(± 0.2) x 10^{-9} mol cm^{-2} s^{-1}at pH 6.85.

Figure 4.8 (panels C and D) shows the respective, simultaneous pH map recorded on the surface of the calcite microcrystal. As expected the average surface pH on the calcite microcrystal surface was higher than in the bulk electrolyte, and found to be 8.05 ± 0.06. This yields a dissolution flux of 1.9(± 0.2) x^{-9} mol cm^{-2} s^{-1} (using Figure 4.4), which is in good agreement with the value found above from the direct measurement of the crystal plane. Moreover, these values are in good agreement with those expected and on earlier bulk measurements.[48, 49]

4.4 Conclusions

A fast and inexpensive method to fabricate nanoscale iridium oxide based pH-SICM probes has been presented. These probes incorporate SICM-based distance feedback control and are suitable for simultaneous topography and pH imaging. The capability of these probes for generating spatially resolved pH maps of surfaces and interfaces has been demonstrated through studies of topographically challenging calcite microcrystals. Both the pH distribution and height change yield rates that are consistent with expected values based on known dissolution kinetics, highlighting the promise of these probes for high resolution quantitative pH mapping in the future.

4.5 References

[1] Zhao, M. C.; Liu, M.; Song, G. L.; Atrens, A. *Corros. Sci.* **2008**, 50, 3168-3178.

[2] Tanabe, H.; Togashi, K.; Misawa, T.; Mudali, U. K. J. *Mater. Sci. Lett.* **1998**, 17, 551-553.

[3] Zhang, J. M.; Lin, C. J.; Feng, Z. D.; Tian, Z. W. J. *Electroanal. Chem.* **1998**, 452, 235-240.

[4] Natter, H.; Hempelmann, R. J. *Phys. Chem.* **1996**, 100, 19525- 19532.

[5] Compton, R. G.; Unwin, P. R. Philos. *Trans. R. Soc., A* **1990**, 330, 1-45.

[6] Orton, R.; Unwin, P. R. J. Chem. Soc., *Faraday Trans.* **1993**, 89, 3947-3954.

[7] Shen, S. S.; Steinhardt, R. A. *Nature* **1978**, 272, 253-254.

[8] Hess, S. T.; Huang, S.; Heikal, A. A.; Webb, W. W. *Biochemistry* **2002**, 41 [3], 697-705.

[9] Miesenbock, G.; De Angelis, D. A.; Rothman, J. E. *Nature* **1998**, 394, 192-195.

[10] Rudd, N. C.; Cannan, S.; Bitziou, E.; Ciani, L.; Whitworth, A. L.; Unwin, P. R. *Anal. Chem.* **2005**, 77, 6205-6217.

[11] Bard, A. J.; Fan, F. R. F.; Kwak, J.; Lev, O. *Anal. Chem.* **1989**, 61, 132-138.

[12] Bard, A. J.; Mirkin, M. V. *Scanning Electrochemical Microscopy*, 2nd ed., CRC Press: Boca Raton, FL, 2012.

[13] Kueng, A.; Kranz, C .; Lugstein, A.; Bertagnolli, E.; Mizaikoff, B. *Angew. Chem., Int. Ed.* **2005**, 44, 3419-3422.

[14] Horrocks, B. R.; Mirkin, M. V.; Pierce, D. T.; Bard, A. J.; Nagy, G.; Toth, K. *Anal. Chem.* **1993**, 65, 1213-1224.

[15] Wipf, D. O.; Ge, F. Y.; Spaine, T. W.; Bauer, J. E. *Anal. Chem.***2000**, 72,

4921-4927.

[16] Bezbaruah, A. N.; Zhang, T. C. *Anal. Chem.* **2002**, 74, 4428- 4432.

[17] Zhang, X.; Ogorevca, B.; Wang, J. *Anal. Chim. Acta* **2002**, 31, 1-10.

[18] Yamamoto, K.; Shi, G. Y.; Zhou, T. S.; Xu, F.; Zhu, M.; Liu, M.;Kato, T.; Jin, J. Y.; Jin, J. Y. *Anal. Chim. Acta* **2003**, 480, 109-117.

[19] Hitchman, M. L.; Ramanathan, S. *Analyst* **1988**, 113, 35-39.

[20] Kreider, K. G.; Tarlov, M. J.; Cline, J. P. *Sens. Actuators*, B **1995**, 28, 167-172.

[21] Marzouk, S. A. M.; Ufer, S.; Buck, R. P.; Johnson, T. A.; Dunlap, L. A.; Cascio, W. E. *Anal. Chem.* **1998**, 70, 5054-5061.

[22] Wang, M.; Yao, S.; Madou, M. *Sens. Actuators*, B **2002**, 81, 313-315.

[23] Elsen, H. A.; Monson, C. F.; Majda, M. J. *Electrochem. Soc.* **2009**, 156, F1-F6.

[24] Lodi, G.; Debattisti, A.; Bordin, G.; Deasmundis, C.; Benedetti, A. J. *Electroanal. Chem.* **1990**, 277, 139-150.

[25] Katsube, T.; Lauks, I.; Zemel, J. N. *Sens. Actuators* **1982**, 2, 399-410.

[26] Bitziou, E.; OHare, D.; Patel, B. A. *Anal. Chem.* **2008**, 80, 8733-8740.

[27] Hansma, P. K.; Drake, B.; Marti, O.; Gould, S. A.; Shiku, H.; Prater, C. B. Science **1989**, 243, 641-643.

[28] Novak, P.; Li, C.; Shevchuk, A. I.; Stepanyn, R.; Caldwell, M.; Hughes, S.; Smart, T. G.; Gorelik, J.; Ostanin, V. P.; Lab, M. J.; Moss, G. W. J.; Frolenkov, G. I.; Klenerman, D.; Korchev, Y. E. *Nat. Methods* **2009**, 6, 279-281.

[29] Takahashi, Y.; Shevchuk, A. I.; Novak, P.; Zhang, Y.; Ebejer, N.; Macpherson, J. V.; Unwin, P. R; Pollard, A. J.; Roy, D.; Clifford, C. A.; Shiku, H.; Matsue, T.; Klenerman, D.; Korchev, Y. E. *Angew. Chem., Int. Ed.* **2011**, 50, 9638-9642.

[30] Takahashi, Y.; Shevchuk, A. I.; Novak, P.; Murakami, Y.; Shiku, H.; Korchev, Y. E.; Matsue, T. *J. Am. Chem. Soc.* **2010**, 132, 10118- 10126.

[31] Comstock, D. J.; Elam, J. W.; Pellin, M. J.; Hersam, M. C. *Anal. Chem.* **2010**, 84, 1270-1276.

[32] Wei, C.; Bard, A. J. *Anal. Chem.* **1995**, 67, 1346-1356.

[33] Korchev, Y. E.; Raval, M.; Lab, M. J.; Gorelik, J.; Edwards, C. R. W.; Rayment, T.; Klenerman, D. *Biophys. J.* **2000**, 78, 2675-2679.

[34] Lazenby, R. A.; McKelvey, K.; Unwin, P. R. *Anal. Chem.* **2013**, 85, 2937-2944.

[35] Yamanaka, K. Jpn. J. *Appl. Phys. 1* **1991**, 30, 1285-1289.

[36] Yoon, Y. H.; Shin, T.; Shin, E. Y.; Kang, H.; Yoo, J. S.; Park, S. M. *Electrochim. Acta* **2007**, 52, 4614-4621.

[37] Yoon, Y. H.; Woo, D. H.; Shin, T.; Chung, T. D.; Kang, H. *J. Phys. Chem. C* **2011**, 115, 17384-17391.

[38] Edwards, M. A.; Williams, C. G.; Whitworth, A. L.; Unwin, P. R. *Anal. Chem.* 2009, 81, 4482-4492.

[39] Stumm, W.; Morgan, J. *Aquatic Chemistry: Chemical Equilibria and Rates in Natural Waters*, 3rd ed., John Wiley Sons: New York, 1995.

[40] Cravotta, C. A.; Trahan, M. K. *Appl. Geochem.* **1999**, 14, 581-606.

[41] Plummer, L. N.; Mackenzie, F. T. *Am. J. Sci.* **1974**, 274, 61-83.

[42] Haynes, W. M.; Lide, D. R.; Bruno T .J. CRC Handbook of Chemistry and Physics 2009-2010.CRC Press, Boca Raton, Fla., 2012

[43] Grime, J. M. A.; Edwards, M. A.; Rudd, N. C.; Unwin, P. R. P. Natl. Acad. Sci. USA. 2008, 105, 14277-14282.

[44] McGeouch, C.-A.; Peruffo, M.; Edwards, M. A.; Bindley, L. A.; Lazenby, R.

A.; Mbogoro, M. M.; McKelvey, K.; Unwin, P. R. J. Phys. Chem. C. 2012, 116, 14892-14899.

[45] Kim, I. W.; Giocondi, J. L.; Orme, C.; Collino, S.; Evans, J. *Cryst. Growth Des.* **2008**, 8, 1154-1160.

[46] Dobson, P. S.; Bindley, L. A.; Macpherson, J. V.; Unwin, P. R. *Langmuir* **2012**, 21, 1255-1260.

[47] Kim, J.; Shen, M.; Nioradze, N.; Amemiya, S. *Anal. Chem.* **2012**, 84, 3489-3492.

[48] Rickard, D.; Sjoberg, E. L. *Am. J. Sci.* **1983**, 283, 815-830.

[49] Plummer, L. N.; Busenberg, E. *Geochim. Cosmochim. Acta* **1982**, 46, 1011-1040.

Chapter 5

Quad-Barrel Multifunctional Electrochemical and Ion Conductance Probe for Voltammetric Analysis and Imaging

The fabrication and use of a multifunctional electrochemical probe incorporating two independent carbon working electrodes and two electrolyte-filled barrels, equipped with quasi-reference counter electrodes (QRCEs), in the end of a tapered micron-scale pipet is described. This quad-probe (4-channel probe) was fabricated by depositing carbon pyrolytically into two diagonally opposite barrels of a laser-pulled quartz quadruple-barrelled pipet. After filling the open channels with electrolyte solution, a meniscus forms at the end of the probe and covers the two working electrodes. The two carbon electrodes can be used to drive local electrochemical reactions within the meniscus while a bias between the QRCEs in the electrolyte channels provides an ion conductance signal that is used to control and position the meniscus on a surface of interest. When brought into contact with a surface,

localized high resolution amperometric imaging can be achieved with the two carbon working electrodes with a spatial resolution defined by the meniscus contact area. The substrate can be an insulating material or (semi)conductor, but herein we focus mainly on conducting substrates that can be connected as a third working electrode. Studies using both aqueous and ionic liquid electrolytes in the probe, together with gold and individual single walled carbon nanotube samples, demonstrate the utility of the technique. Substrate generation-dual tip collection measurements are shown to be characterized by high collection efficiencies (approaching 100%). This hybrid configuration of scanning electrochemical microscopy (SECM) and scanning electrochemical cell microscopy (SECCM) should be powerful for future applications in electrode mapping, as well as in studies of insulating materials as demonstrated by transient spot redox-titration measurements at an electrostatically charged Teflon surface and at a pristine calcite surface, where a functionalized probe is used to follow the immediate pH change due to dissolution.

5.1 Introduction

The localized investigation of interfaces is of importance towards understanding the behavior of heterogeneous surfaces such as electrodes, catalysts and biological membranes.[1-5] Furthermore, since such interfaces are often (electro)chemically dynamic, the ability to probe reactive fluxes locally is particularly beneficial for developing microscopic models of interfacial reactivity. In this context, electrochemical scanning probe microscopy techniques, especially scanning electrochemical microscopy (SECM)[6-8] and scanning droplet-based electrochemical techniques,[9-11] have revealed considerable quantitative information on surface and interfacial processes.

SECM employs a mobile ultramicroelectrode (UME) placed close to a sample bathed in solution, the response of which depends on the (electro)chemical properties and topography of the sample.[12-14] In contrast, scanning droplet electrochemical techniques use a liquid droplet formed at the end of a probe to assemble an electrochemical cell on a sample surface, and hence confine electrochemical reactions to the contact area between the droplet and the surface.[15,16] Probes of this type have tended to have large footprints and have been used for the characterization of a variety of substrates and surface properties.[17,18] More recently, scanning droplet techniques have evolved to allow the imaging of electrochemical activity with higher spatial resolution.[19]

Among scanning droplet techniques, scanning electrochemical cell microscopy (SECCM) has been developed by us as a means of achieving high control over meniscus contact with a surface.[20] In this approach, a tapered theta pipet filled with electrolyte solution serves as the probe and the ion current measured between

the quasi-reference counter electrodes (QRCEs), one in each of the two barrels, provides a feedback signal for positioning the probe close to the surface, making it possible to maintain a constant probe-surface distance irrespective of the surface topography.[17] This type of technique has been employed to deposit biomolecules[21] and reagents on surfaces[22,23] and for simultaneous electrochemical and topography imaging of surfaces in aqueous[17,24,25] and non-aqueous environments.[5]

In droplet-based techniques the sample surface wetted by the meniscus can be an insulator or, if a (semi)conductor, can act as a working electrode where the electrochemical activity can be measured.[9,20] However, by incorporating additional working electrodes into the end of the probe it is possible to enhance the capability of these types of techniques. Fountain pen probes,[26] incorporating a microfluidic channel with integrated working and counter/reference electrodes, employ just such a scheme. Microfluidic push-pull probes[27,28] that incorporate a working electrode into a droplet at the end of a probe, have also been reported for performing electrochemical measurements in a constantly renewed electrolyte droplet. At present, such probes operate with quite large footprints to enable a large area of sample to be investigated.[17]

Herein, we present a simple and quick method for fabricating a new type of probe comprising two open barrels that are filled with electrolyte and equipped with QRCEs and two carbon working electrodes. We call this a quad-probe, and used it for high resolution electrochemical characterization of surfaces. The probe combines the merits of SECM and SECCM by creating a droplet cell incorporating two independent working electrodes directly into a micron-scale droplet which can be moved and positioned on a substrate enabling multifunctional surface imaging and the localized investigation of processes at surfaces and interfaces. The

capability of this technique for amperometric surface imaging is demonstrated by mapping the surface electrochemical activity of a gold band electrode on glass and an individual single-walled carbon nanotube (SWNT) on an insulating surface. In the latter case, we employed a room temperature ionic liquid (RTIL) as the supporting electrolyte in the quad-probe to demonstrate the wide range of electrolytes open to study. In addition, the versatility of this quad-probe was further demonstrated by employing them to investigate a redox reaction at an insulating surface charged by contact electrification and by monitoring the pH change accompanying the dissolution of calcite.

5.2 Experimental

Details of standard materials, reagents and sample preparation methods employed for this study were described in chapter 2.

5.2.1 Quad-probe fabrication

The quad-probes were fabricated from quartz quadruple-barrelled capillaries (MBT-015-062-4Q, Friedrich & Dimmock, Inc.), pulled to a sharp point by a laser puller (P-2000, Sutter Instruments) using a custom-developed two line program (Line 1:HEAT-925, FILAMENT-4, VELOCITY-40, DELAY-130, PULL-40; Line 2:HEAT-875, FILAMENT-4, VELOCITY-60, DELAY-126, PULL-35). Two diagonally opposite barrels were filled with carbon to form the electrodes by adapting a carbon electrode fabrication process described previously.[29-31] Briefly, the top ends of two diagonally opposite barrels were closed by using Blu-Tack (Bostik, UK) and butane was passed through the other two barrels, via tubing, with the end held under

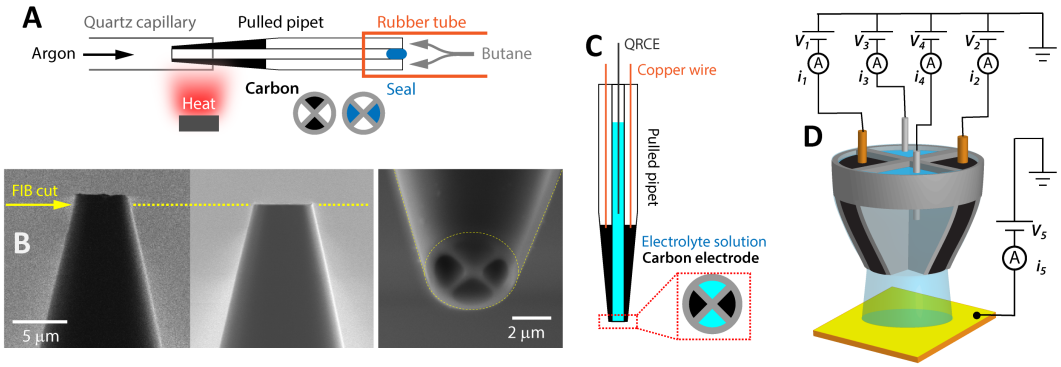

Figure 5.1: (A) Schematic of the carbon deposition step for the fabrication of a quad-probe. Two diagonally opposite barrels were closed by using Blu-Tack (Bostik, UK), and butane was passed through the other two barrels. The tip of the pipet was heated with a butane torch under an argon atmosphere to pyrolytically deposit carbon from the butane.[29-31] (B) FIB-SEM micrograph (side view) of the quad-probe before (left) and after (middle) FIB cutting. On the right is an SEM micrograph of the end of a typical quad-probe showing carbon electrodes (top and bottom) and open barrels (left and right). (C) Schematic of the fabricated quad-probe. (D) Schematic of the five electrode configuration: two carbon working electrodes in the barrel of the probe, two open barrels filled with electrolyte and AgCl coated Ag wire QRCEs, and a substrate electrode. The voltage of each electrode, with respect to ground, was controlled separately ($V_{1\text{-}5}$), and the currents at each electrode ($i_{1\text{-}5}$) were recorded separately.

an argon atmosphere. The tip of the pipet was heated with a butane torch, for 35 s, to deposit carbon pyrolytically from the butane, thus forming the electrodes, as illustrated in Figure 5.1A. Field-emission scanning electron microscopy (FE-SEM, Supra 55-VP, Zeiss) of a typical quad-probe is shown in Figure 5.1B. A range of probe sizes, between 200 nm and 10 μm across each barrel, were easily fabricated by changing the laser pulling parameters during fabrication, but herein we focus on probes with a size of ca. 1 μm across each barrel.

At this stage, the probes were useable but some were further optimized by focused ion beam (FIB) cutting, which is a powerful method for tailoring carbon

nanoelectrodes.32 We used FIB-SEM (JEOL 4500, JEOL), at an accelerating voltage of 5 kV, with gallium ions (Ga^+). Figure 1B shows the lateral view of a typical quad-probe before and after FIB cutting. An electrical connection was established to each carbon electrode by inserting a copper wire through the top end of the pipet barrel to make a back contact. The open barrels were filled with the solution of interest and a AgCl-coated Ag wire, acting as a QRCE, was inserted into each. A liquid meniscus naturally formed at the end of the probe, covering the carbon electrodes to make a multifunctional droplet-based electrochemical cell.

5.2.2 Electrochemical Configuration

A four or five electrode configuration was used, comprising the two carbon working electrodes in the probe and two Ag/AgCl QRCEs in the open (electrolyte-filled) barrels of the probe and, when in contact with a substrate electrode, this was a third working electrode. This configuration is illustrated in Figure 1D. The potential was controlled with respect to ground ($V_{1\text{-}4}$ in Figure 5.1D), and current was measured ($i_{1\text{-}4}$ in Figure 5.1D) at each electrode in the probe independently using a custom-built quadpotentiostat. An additional custom-built current to voltage convertor was employed at the substrate to measure the substrate current (i_5 in Figure 5.1D). The potential of the substrate was also controlled with respect to ground (V_5) and could be defined with respect to the QRCEs. For transient pH measurements, the potential of the pH electrode was measured with respect to one of the QRCEs (held at 0.0 V with respect to ground) using a custom-built voltage follower.[31]

5.2.3 Electrochemical Imaging

Electrochemical imaging was performed using the Warwick Electrochemical-Scanning Probe Microscopy (WEC-SPM) platform described in chapter 2. To position the probe close to the substrate, an ion current-based feedback control scheme was used.[20] Briefly, a 100 mV bias was applied between the QRCEs to induce an ion current between the open barrels of the probe. The probe was oscillated (60 nm peak-peak amplitude, 280 Hz frequency) normal to the surface, generating an alternating current (i_{AC})when the meniscus was in contact with the sample. This i_{AC} was measured via the lock-in amplifier, and the magnitude of i_{AC} was used as a feedback signal to detect contact between the liquid meniscus and the surface and to control the separation between the tip of the probe and the surface as in conventional SECCM.[20] Two-dimensional electrochemical images of the substrate surface were constructed from a series of line scans, during which the probe was moved laterally, with i_{AC} magnitude feedback control that maintained a constant tip-substrate separation, via a feedback loop.

5.2.4 Transient Spot Measurements: Electrostatic Charged Insulators and pH Evolution

Surface charging of Teflon was achieved by rubbing the Teflon surface with a poly(methyl methacrylate) (PMMA) block for 30 s. The quad-probe (3 μm total diameter) was filled with 0.1 mM solution of ruthenium(III) hexamine ($Ru(NH_3)_6{}^{3+}$) and was brought into contact with the Teflon surface at a speed of 200 nm/s while oscillating (60 nm peak to peak amplitude, 288 Hz) the probe normal to the surface. An increase in i_{AC} to 10 pA was used for feedback to detect substrate contact.

Upon initial meniscus contact the probe was held at the surface for ca. 15 seconds while recording currents at the carbon electrodes for the diffusion limited oxidation of $Ru(NH_3)_6{}^{2+}$ produced at the Teflon surface.

For Transient pH measurements, the quad-probe was modified by electrodepositing a thin layer of hydrous iridium oxide onto the carbon electrodes of the quad-probe by using a method described previously.[31] Briefly, a potential of + 0.68 V (versus Ag/AgCl) was applied to the carbon electrodes immersed in the deposition solution made from iridium tetrachloride for 10 s. The functionalized electrodes were calibrated in various pH solutions by measuring the open circuit potential at the pH electrode and one the QRCEs in the open channels (held at 0 V with respect to ground, not shown) using a home-built voltage follower.[31] Each probe was calibrated before and after the experiments and the responses were compared directly to that of a commercial glass pH electrode. For pH measurement during calcite dissolution, a 0.01 M KCl solution (pH 6.8) was used to fill the open barrels of the functionalized quad-probes. A potential difference of 0.1 V was applied between the two QRCEs in the probe (while keeping the potential of one of the QRCEs at 0 V with respect to ground), to induce an ion current between the QRCEs for positional control and probe was oscillated (60 nm peak-peak amplitude, 280 Hz) normal to the surface generating an alternating current (i_{AC}) when the meniscus was in contact with the surface. The quad-probes were approached towards the crystal surface using the increase in i_{AC} as feedback for substrate contact (See main text, Figure 5.54D). Upon initial contact the probe was held at the crystal surface for ca. 4 seconds while recording the open circuit potential at the pH electrodes with respect to one of the QRCEs in the open barrels of the probe held at 0 V (with respect to ground).

5.3 Results and Discussion

5.3.1 Fabrication and Characterization of Quad-Probes

A typical quad-probe (Figure 5.1C) consists of four quadrant shaped sectors, of which two diagonally opposite sectors were filled with carbon to form the working electrodes (top and bottom in Figure 5.1B) and the other two sectors were left open (left and right in Figure 5.1B). The size of the sectors and the thickness of the side walls were dependent on the laser pulling parameters employed. Herein, sectors with characteristic dimensions ca. 1 μm were used.

When the two open barrels of the quad-probes were filled with solution, a liquid meniscus (droplet) was formed at the end of the probe. This meniscus covered both the carbon electrodes forming a small electrochemical droplet cell. With the probes in air (Figure 5.2A), linear sweep voltammograms (LSVs) of individual carbon electrodes within quad-probes were recorded for the one-electron oxidation of ferrocenylmethyl trimethylammonium ($FcTMA^+$ to $FcTMA^{2+}$). The potential, V_1 for electrode 1 or V_2 for electrode 2 (see Figure 5.1D), was swept at 50 mV/s over defined values with respect to ground (with the other working electrode unconnected), while the potential of the QRCEs was held at ground. Responses of the two electrodes in a typical probe are shown as dashed lines in Figure 5.2B.

As expected of a microscale electrode for moderate time scales,[33] the LSVs at each electrode shows a sigmoidal response. The magnitude of the limiting current for each electrode was slightly different, because the sizes and positions of the electrodes are different, which is common for probes fabricated by this type of method.[30] The magnitude of the limiting current depends on the mass transport

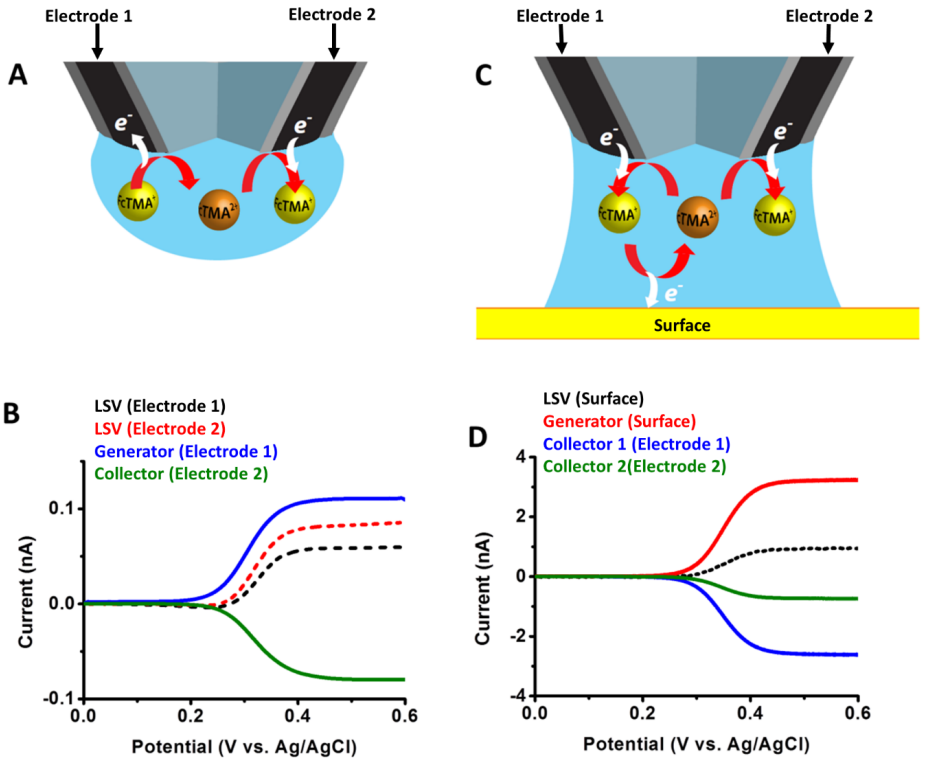

Figure 5.2: (A) Schematic of the quad-probe in tip generation-tip collection mode, with the probe away from a surface and $FcTMA^{+/2+}$ couple as the redox mediator. One electrode (left) oxidizes $FcTMA^{+}$ to $FcTMA^{2+}$, while the other (right) reduces $FcTMA^{2+}$ to $FcTMA^{+}$. The QRCES in the open channels (not shown) act as the reference/counter electrodes. (B) LSVs for the oxidation of $FcTMA^{+}$ $FcTMA^{2+}$ at two electrodes in the quad-probe. Each was swept with the other working electrode unconnected (black and red dotted lines), and voltammetric responses for the $FcTMA^{+/2+}$ couple as the potential of the generator electrode was swept between 0 and 0.6 V; the collector electrode current was held constant at 0 V for the same probe (blue and green solid lines). (C) Schematic of the quad-probe in substrate generation/tip-tip collection mode. The substrate electrode oxidizes $FcTMA^{+}$ to $FcTMA^{2+}$, while the probe electrode reduces $FcTMA^{2+}$ to $FcTMA^{+}$. The QRCEs in the open barrels in the probe act as the reference/counter electrodes. (D) LSVs for the oxidation of $FcTMA^{+}$ to $FcTMA^{2+}$ at the substrate while the other electrodes were unconnected (black dotted line) and LSVs for the generation and collection currents in surface generation/tip-tip collection mode for the $FcTMA^{+/2+}$ couple as the redox mediator for the same probe. The potential of the generator electrode was swept from 0 to 0.6 V, and the potential of the collector electrodes was held constant at 0 V.

to the electrode which, in the droplet configuration with only one active working electrode, is limited to diffusion of the electroactive species ($FcTMA^+$) down the two open barrels of the probe.[34]

Next, the same probe was used in air in a generation/collection (G/C) mode using $FcTMA^{+/2+}$as the redox couple (Figure 5.2A). For this, the potential of one of the carbon electrodes (designated as the generator electrode) was swept for the one-electron oxidation of $FcTMA^+$to $FcTMA^{2+}$(from V_1 = 0.0 to 0.6 V with respect to ground) while keeping the potential of the other electrode (designated as the collector electrode) at 0.0 V for the diffusion-limited reduction of $FcTMA^{2+}$back to $FcTMA^+$. The two QRCEs were held at ground. A schematic of this configuration is shown in Figure 5.2A. The resulting generation voltammogram and collection response are shown in Figure 5.2B, where the potential refers to that of the generator electrode. The diffusion-limited collection efficiency, defined as the ratio of the collection current to generation current, was ca. 80% in this case, which is higher than the collection efficiencies previously reported for dual carbon probes in a bulk solution.[30] The droplet configuration confines the diffusional mass transport to the meniscus, and as a result, a large proportion of the $FcTMA^{2+}$produced at the generator electrode reaches the collector electrode where it is reduced back to $FcTMA^+$(with only a small amount escaping up the two open barrels of the probe). Note that the estimation of collection efficiency in this way does not account for the oxidized and reduced forms of the redox mediator ($FcTMA^{+/2+}$) having slightly different diffusion coefficients,[35] although this would only have a minor effect and, in any case, does not influence the steady-state current ratio under quantitative (100%) collection. The regeneration of $FcTMA^+$at the collector electrode increases its flux to the generator electrode, evident as an

increase in the generation current (compared to the response of the individual electrode with the second carbon electrode unconnected; see Figure 5.2B).

In subsequent experiments, a quad-probe was mounted onto a piezo-electric positioner and was brought close to a gold electrode to bring the meniscus into surface contact. The area of the gold surface wetted by the meniscus forms a third working electrode (Figure 5.2C). LSVs were recorded at the substrate electrode for the oxidation of $FcTMA^+$, while the two carbon electrodes were disconnected, and the QRCEs were held at ground. This configuration is similar to that of SECCM, and the typical voltammetric response shown as the black dotted line in Figure 5.2D is that of steady-state diffusion.[34] A full five electrode configuration was then used with the substrate acting as the generator electrode and the two carbon electrodes in the probe as the collector electrodes (substrate generation/tip-tip collection mode, by analogy to SECM[6, 36]). A schematic of this configuration is shown in Figure 5.2C. Figure 5.2D shows an LSV recorded for the oxidation of $FcTMA^+$to $FcTMA^{2+}$at the substrate and the collection of $FcTMA^{2+}$at the two tip electrodes. Both the generation current and the collection currents showed a sigmoidal shape as a function of the generator electrode potential. Notably, the generation current was approximately three times larger with the collector electrodes switched on than without. This increase in generation current is due to the regeneration of $FcTMA^+$at the collector electrodes which enhances the flux of $FcTMA^+$to the generator electrode. Individual collection efficiencies of ca. 76% and ca. 23% were observed for the two carbon electrodes. The variation in collection efficiencies between individual electrodes within the quad-probe can be attributed to the differences in size of the electrodes coupled with the differences in electrode recession and different probe to surface distance.[30] Importantly, the total

collection efficiency of ca. 99% observed for the probe in substrate generation/tip-tip collection means that practically all the $FcTMA^{2+}$generated at the substrate was collected at the probe electrodes. Although the two carbon electrodes in the probes are not identical, as reflected by differences in their collection efficiencies, it is still possible to realize complete collection of the substrate-generated product. At the next level, we have outlined elsewhere that deeper knowledge of the geometry of dual carbon probe electrodes and methods for characterization (e.g., via collection efficiencies) can open up detailed finite element simulations of mass transport to individual electrodes, if required.[30]

5.3.2 Electrochemical Imaging

The ion current between the two QRCEs was used as a signal to detect the engagement of the meniscus with the surface, allowing the probe to be laterally scanned across a surface following the contours of the surface as in SECCM.[20] To test the suitability of this quad-probe for continuous surface electrochemical measurements in an aqueous environment, line scan profiles were obtained across a gold band (ca. 50 μm) substrate on glass, using an ion current-based feedback control similar to SECCM[20] For this, the gold band was held at a potential (V_5) of 0.45 V while keeping the potential of the two carbon electrodes in the quad-probe (V_1 and V_2) at 0 V and QRCEs around zero (V_3 = -0.05 V, V_4 = 0.05 V). This allowed the oxidation of $FcTMA^+$ to $FcTMA^+$ at the gold band in contact with the meniscus, along with the collection of $FcTMA^+$ at the two probe electrodes as outlined in the diagram in Figure 5.3A. The probe was oscillated (60 nm peak to peak amplitude, 280 Hz) normal to the surface, generating an alternating current (i_{AC}) when the

meniscus was in contact with the sample.

This i_{AC} was measured via the lock-in amplifier and the magnitude of i_{AC} was used as a feedback signal to detect the contact between the liquid meniscus and the surface, and to control the separation between the tip of the probe and the surface. Examples of profiles of the generation current recorded at the gold band substrate and collection currents recorded at the probe electrodes as the probe was moving across the substrate from glass to a gold band and back to glass are shown in Figure 5.3 B.

When the meniscus from the probe was on the insulating glass surface, no current was observed on either the generator or collector electrodes. The current at both the generation and collection electrodes increased sharply as the meniscus came into contact with the gold band and decreased back to zero after the meniscus lost contact with the gold band. The generator current increased to ca. 7 nA as the probe moved across the gold band and dropped to zero after the meniscus lost contact with the gold band. A ca. 1.3 nA increase in collection current at one electrode and ca. 5.2 nA in the other electrode was observed. An average collection efficiency of ca. 92% was detected during the line scan over the gold part of the substrate. The width of both the generation and collection current peaks (ca. 60 μm), is governed by the width of the gold band and the meniscus size, and was consistent with the size of the gold band used (ca. 50 μm) and the meniscus size expected (ca. 5 μm) for the probe employed, suggesting that a well-defined electrochemical cell can be assembled and maintained close to target substrates with this quad-probe for localized electrochemical imaging.

In order to demonstrate the feasibility of using quad-probes for high resolution electrochemical imaging with nonaqueous electrolytes, electrochemical ac-

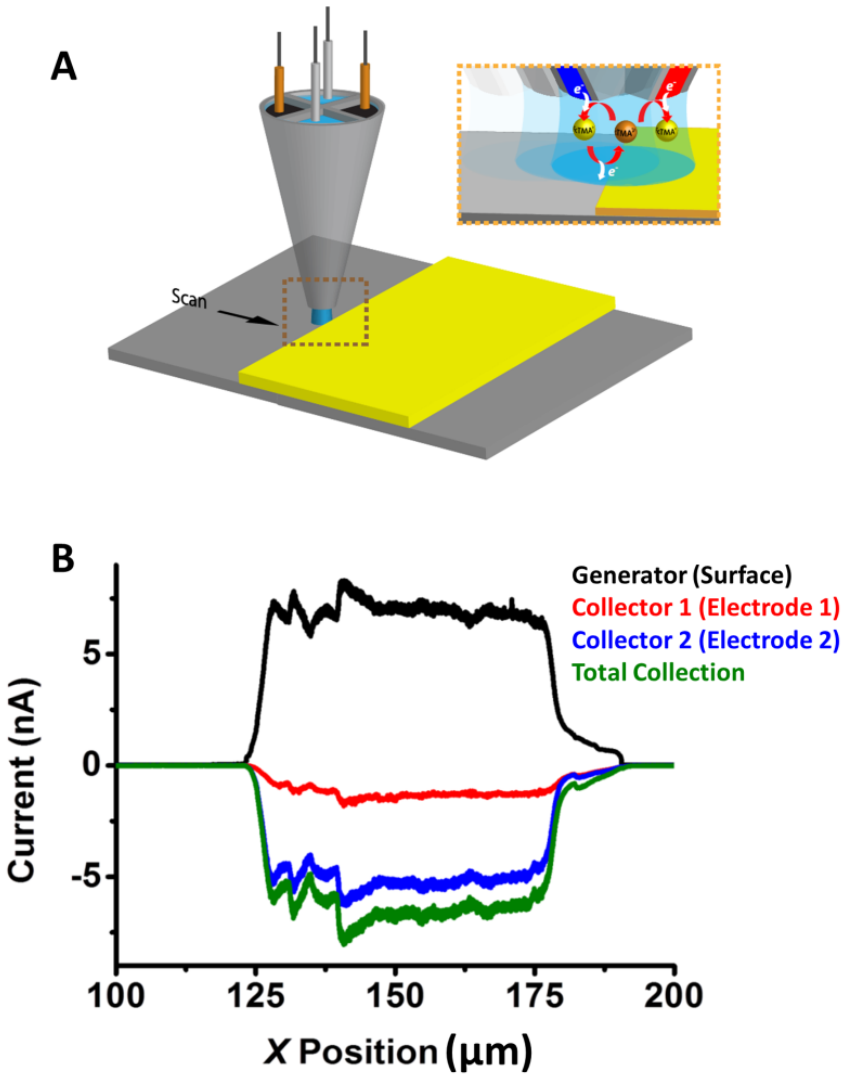

Figure 5.3: Currents measured during a line scan recorded over a gold band on glass substrate using the quad-probe in surface generation/ tip-tip collection mode. (A) Schematic of the line scan configuration in substrate generation/tip-tip collection mode. The gold substrate was held at a potential that generated $FcTMA^{2+}$ (from $FcTMA^{+}$ in the bulk solution) and the two carbon working electrodes in the probe were held at a potential to collect any $FcTMA^{2+}$, when the substrate was in contact with the meniscus. (B) Generation (black line) and collection (red and blue lines) and total collection (green line) currents recorded on the gold band and at the two probe electrodes.

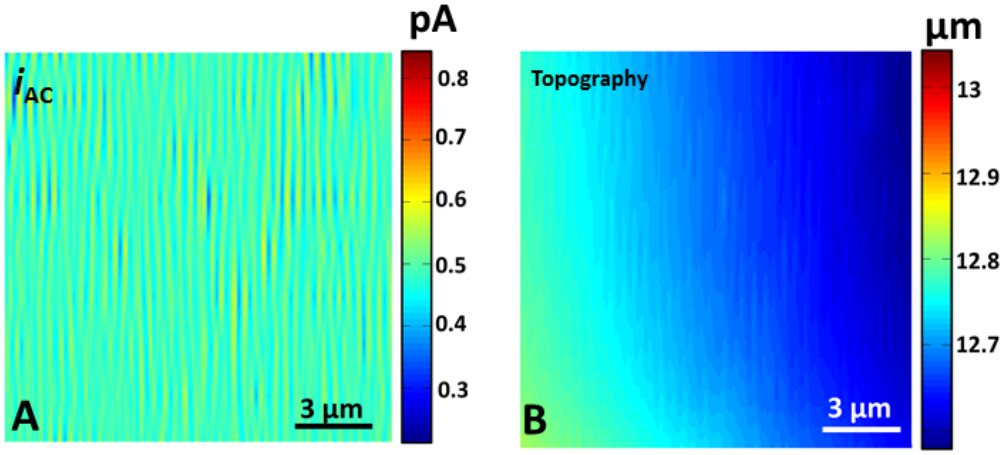

Figure 5.4: i_{AC} map (A) and topography map (B) recorded during the amperometic imaging of SWNT using the quad-probe in substrate generation/ tip-tip collection mode.

tivity maps of an individual SWNT on an insulating (Si/SiO2) substrate were recorded by operating in a surface generation/tip-tip collection configuration using the $FcTMA^{+/2+}$redox couple in a RTIL (Figure 5.4A). A potential difference of 0.1 V was applied between the two QRCEs in the probe (V_3 = -0.05 V, V_4 = 0.05 V) to induce an ion current between the QRCEs and the quad-probe was oscillated (60 nm peak-peak amplitude, 280 Hz) normal to the surface generating an alternating current (i_{AC}) when the meniscus was in contact with the surface. This i_{AC} was used as the feedback signal to maintain constant contact with the surface.

For the data shown herein, an i_{AC} set-point of 0.5 pA was used. Figure 5.4A shows the i_{AC} map recorded during the scan. The values of i_{AC} were consistent with the set-point employed, indicating that surface contact was maintained throughout the scan. Furthermore, Figure 5.4 B shows the topography map

recorded during the scan. There are no specific topographical features, except a slope on the Si/SiO2 sample and possibly some effect of thermal drift.

Electrical connection to the SWNT was established through a palladium side contact with the potential (V_5) held at 0.45 V while keeping the potential of the two carbon electrodes in the quad-probe (V_1 and V_2) at 0.0 V, allowing the oxidation of $FcTMA^+$to $FcTMA^{2+}$at the SWNT in contact with the meniscus along with the diffusion-limited collection of $FcTMA^{2+}$at the two probe electrodes as outlined in the diagram in Figure 5.5A. The electrochemical images were recorded as a series of lines scans over a scan area of 15 μm by 15 μm, with a line scan every 2 μm at a scan rate of 1 μm/s.

Amperometric maps recorded during a typical surface generation/tip-tip collection scan are shown in Figure 5.5 (Panels B to D) including the line profiles of electrochemical currents recorded at the SWNT substrate (Panels B and C) and generation current, individual electrode collection currents, and overall collection efficiency maps (Panel D), respectively. No current was observed either at the probe electrodes or at the substrate while the tip was scanning over the insulating (Si/SiO2) substrate as no $FcTMA^{2+}$could be produced at the surface. As the probe encountered the SWNT, the generation current at the SWNT gradually increased, reaching a maximum value when the center of the probe was directly over the SWNT. This is a consequence of the large length of SWNT in contact with the meniscus and the maximum recycling of the $FcTMA^{2+}$into $FcTMA^+$by the probe electrodes, since the SWNT is located between both electrodes. An average generation current of ca. 2.3 $\pm$ 0.5 pA was recorded at the SWNT at this maximum point. Average collection currents of ca. 1.5 $\pm$ 0.3 pA at electrode 1 and 0.65 $\pm$ 0.2 pA at electrode 2 were detected while the meniscus was scanning

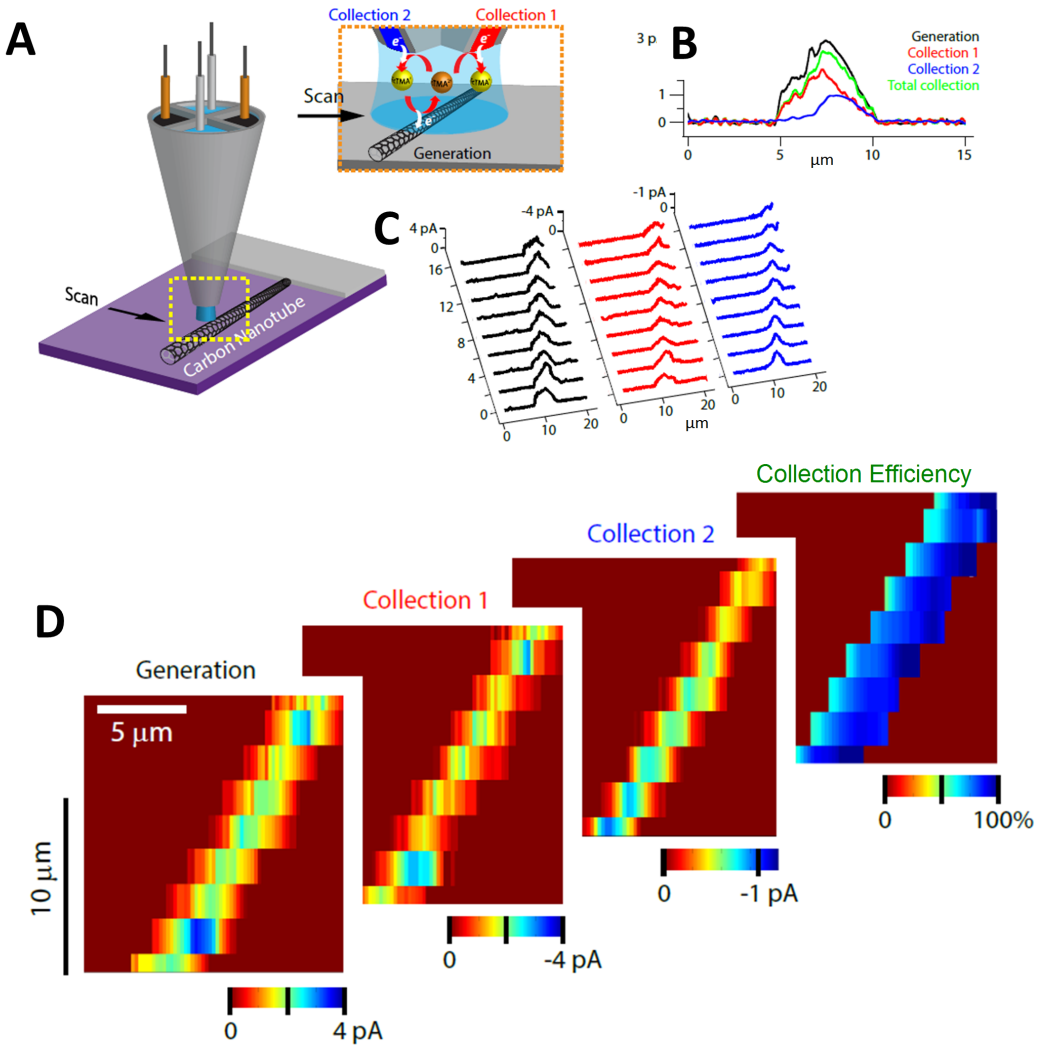

Figure 5.5: Schematic of imaging in surface generation/tip-tip collection mode with a five electrode configuration. The substrate (SWNT) was held at a potential that generated $FcTMA^{2+}$, while the two carbon electrodes in the probe were held at a potential to collect any $FcTMA^{2+}$ produced. (B) Line profiles of generation (black) and collection (red and blue) currents recorded as the probe was scanned over a SWNT. (C) Current profiles (magnitude) recorded during a single line scan illustrating the induction of electrochemical currents at each electrode, as the meniscus passed over the SWNT. (D) Generator, collector 1, collector 2, and collection efficiency maps recorded on a SWNT.

across the SWNT, with an overall collection efficiency of ca. 92 ± 8%. The width of the electroactive area in both the generation current and collection efficiency maps as the quad-probe traverses the SWNT (ca. 5 μm) gives a good guide as to the meniscus size and is similar to that of the probe employed. This highlights that multifunctional and electrochemical imaging can be carried out with these new quad-probes with a spatial resolution similar to the probe size.

5.3.3 Transient Spot Measurements: Electrostatic Charged Insulators and pH Evolution

A key advantage of the droplet-based quad-probe is the capability to measure the electrochemical current at the tip working electrodes due to substrate-generated products (including at insulators) upon initial meniscus contact. As an example, we measured the excess negative charge present on a Teflon surface after contact electrification.[37] Teflon surfaces were negatively charged by rubbing them with poly(methyl methacrylate) (PMMA). The resulting charge has been shown to drive the reduction of metals ions to metals as well as several redox mediators.[8] Herein, we used $Ru(NH_3)_6^{3+/2+}$ redox couple to electrochemically detect the amount of negative charge present on a Teflon surface following contact electrification as illustrated in Figure 5.6A. The probe, containing aqueous electrolyte with 0.1 mM $Ru(NH_3)_6^{3+}$ and with the carbon electrodes held at 0.0 V (vs Ag/AgCl QRCE) to detect any $Ru(NH_3)_6^{2+}$ that might be produced, was approached toward the charged Teflon surface (using i_{AC} feedback), halted immediately following initial meniscus contact, and held for ca. 15 s at the substrate.

Figure 5.6B shows the electrochemical current over time throughout this

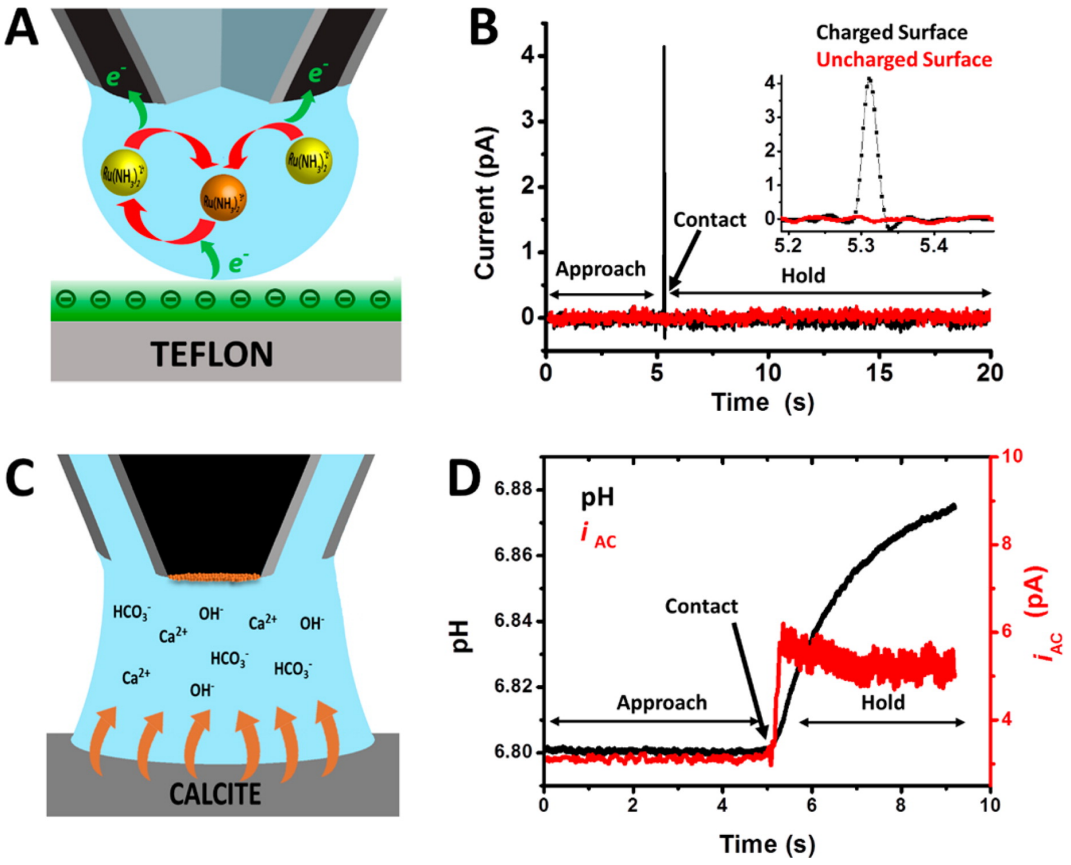

Figure 5.6: (A) Schematic of electrostatic electrochemistry using a $Ru(NH_3)_6^{3+}$/ $Ru(NH_3)_6^{2+}$ redox couple at a negatively charged Teflon surface. The negative surface charge on the Teflon reduces $Ru(NH_3)_6^{3+}$to $Ru(NH_3)_6^{2+}$, which then diffuses toward the probe electrodes where it is oxidized (and measured) to $Ru(NH_3)_6^{3+}$. The QRCEs in the open channels (not shown) act as the reference/counter electrodes. (B) Approach curves showing the electrochemical current measured at the quad-probe working electrodes upon contact with a negatively charged Teflon surface (black line) and an uncharged Teflon surface (red line). (Inset: zoom-in showing individual data points during transient current measurement). (C) Schematic of the dissolution of calcite when the quad-probe meniscus is in contact with the calcite surface. The open circuit potential was measured between the pH electrode and one of the QRCEs in the open channels (held at 0 V with respect to ground, not shown) using a home-built voltage follower.[31] (D) pH and i_{AC} recorded at the quad-probe during approach to a pristine calcite surface showing feedback control(i_{AC}) and an increase in pH after the meniscus came into contact with the calcite surface.

entire process. A transient electrochemical current was observed immediately following meniscus contact, which is due to the flux of $Ru(NH_3)_6^{2+}$ from the charged Teflon surface, which is oxidized back to $Ru(NH_3)_6^{3+}$ at the carbon electrodes. From the charge of the current transient recorded at the tip electrode (black line, Figure 5.6B), the charge at the Teflon substrate was found to be ca. 14 nC cm^{-2}(3 μm diameter meniscus footprint), consistent with the values found using bulk measurements using a Faraday cup.[39] Control measurements at an uncharged Teflon surface (red line, Figure 5.6B) did not show any detectable change in the electrochemical current upon contact. The local point measurements shown here could be extended in the future for surface mapping of charged insulators, particularly as charge heterogeneities might be expected across the surface as implied from heterogeneous metal deposits.[39] Technologically, such measurements could be valuable as Teflon substrates that exhibit micro-nanoscale surface roughness are being explored for energy harvesting with impinging water droplets.[40]

In addition, the carbon working electrodes were functionalized with hydrous iridium oxide (IrOx) to create a pH responsive electrode[31] to follow the local pH change during the initial dissolution of a pristine calcite crystal surface. For this measurement, a functionalized quad-probe was filled with 10 mM KCl solution (pH 6.8) and brought into contact with a freshly cleaved calcite surface to form a thin layer electrochemical cell between the probe and crystal surface (Figure 5.6C). Instantaneous meniscus contact (using i_{AC} feedback (Figure 5.6D)) prompted dissolution of calcite causing the pH to increase. The pH response of these probes is fast, and the transient is not associated with the electrode response time but, rather, highlights the surface kinetics, for example, the nucleation and expansion of nanopits,[41] to create a surface where the dissolution attains a steady-state

(plateau of pH). pH responses of this type could be analyzed to reveal the kinetics of dissolution with further study. Figure 4D shows that a pH change (ca. 0.08 pH units) at the surface was detected following contact and highlights the significant prospect of a quad-barrel approach in crystal dissolution studies where it is challenging to measure such transient and subtle processes at pristine surfaces (rather than partially reactive as with other techniques[41]) with subsecond resolution. Additionally, in cases where surface fouling is a concern, such as in corrosion and other processes, this approach of transient meniscus contact offers a tremendous opportunity for functional mapping.

5.4 Conclusions

The rapid fabrication of multifunctional quad-probes has been described. When key features of SECM and SECCM are merged, these probes incorporate two working electrodes immersed in a liquid meniscus that can be operated in various generation-collection modes. As an imaging tool, the quad-probe enables localized high resolution electrochemical imaging of surfaces and interfaces and is particularly attractive given the high collection efficiencies inherent in this configuration. The capability of these probes for the localized electrochemical investigation of surfaces was demonstrated by employing them for electrochemical imaging of an individual SWNT substrate. Moreover, the suitability of these probes for electrochemical measurements in nonaqueous environments was also demonstrated by using a RTIL as the supporting electrolyte. This is particularly noteworthy, as studies of RTILs with SECM are recognized to be difficult with the low diffusion coefficients and often large differences of the diffusion coefficients of oxi-

dized and reduced species, making steady-state feedback measurements difficult with micrometer sized probes[42-44] and hitherto necessitating the use of extremely high redox concentrations with smaller probes.[45] Further, the capability of these probes for transient current measurements on insulating and reactive surfaces was demonstrated. This aspect opens up the prospect of surface titrations and adsorption/modification measurements on a wide range of surfaces.

In general, quad-probes permit simultaneous detection of multiple targets in a confined droplet, which may allow many interesting and difficult substrates to be investigated in the future. Moreover, these probes could easily be modified to integrate with other electrochemical techniques such as scanning ion conductance microscopy (SICM)[29] where multiple electrodes and detection of multiple species could be highly valuable especially for biological applications. In this context, as well as for meniscus-based imaging, it should be mentioned that the carbon electrodes can be sensitized to expand the range of species that can be detected amperometrically[46] and potentiometrically. [31] Beyond electrochemistry, micropipettes and nanopipettes find increasing use in analytical science from fluidic systems to electrospray techniques, and the ability to incorporate multiple sensor electrodes into such devices could be beneficial in future applications.

5.5 References

[1] Kosmulski, M. *Chemical properties of material surfaces*; Marcel Dekker: New York, 2001.

[2] Wang, G.; Zhang, L.; Zhang. *J. Chem. Soc. Rev.* **2012**, 41, 797- 828.

[3] Mauzeroll, J.; Bard, A. J. *Proc. Natl. Acad. Sci. U.S.A.* **2004**, 101, 7862-7867.

[4] Amemiya, S.; Bard, A. J. *Anal. Chem.* **2000**, 72, 4940-4948.

[5] Aaronson, B. D. B.; Lai, S. C. S.; Unwin, P. R. *Langmuir* **2014**, 30, 1915-1919.

[6] Bard, A. J., Mirkin, M. V., Eds. *Scanning electrochemical microscopy*; 2nd ed.; CRC Press: Boca Raton, FL, 2012.

[7] Bard, A. J.; Fan, F. R. F.; Kwak, J.; Lev, O. A. *Anal. Chem.* **1989**, 61, 132-138.

[8] Bard, A. J.; Denuault, G.; Lee, C.; Mandler, D.; Wipf, D. O. *Acc. Chem. Res.* **1990**, 23, 357-363.

[9] Lohrengel, M. M.; Moehring, A.; Pilaski, M. Fresenius J. *Anal. Chem.* **2000**, 367, 334-339.

[10] Gasiorowski, J.; Kollender, J. P.; Hingerl, K.; Sariciftci, N. S.; Mardare, A. I.; Hassel, A. W. *Phys. Chem. Chem. Phys.* **2014**, 16, 3739- 3748.

[11] Clausmeyer, J.; Henig, J.; Schuhmann, W.; Plumere, N. *ChemPhysChem* **2014**, 15, 151-156.

[12] Amemiya, S.; Bard, A. J.; Fan, F.-R. F.; Mirkin, M. V.; Unwin, P. R. *Annu. Rev. Anal. Chem.* **2008**, 1, 95-131.

[13] Zhou, J.; Zu, Y.; Bard, A. J. *J. Electroanal. Chem.* **2000**, 491, 22- 29.

[14] Kranz, C. *Analyst* 2014, 139, 336-352.

[15] Lohrengel, M. M.; Moehring, A.; Pilaski, M. *Electrochim. Acta* **2001**, 47,

137-141.

[16] Arjmand, F.; Adriaens, A. *J. Solid State Electrochem.* **2014**, 18, 1779-1788.

[17] Ebejer, N.; Guell, A. G.; Lai, S. C. S.; McKelvey, K.; Snowden, M. E.; Unwin, P. R. *Annu. Rev. Anal. Chem.* **2013**, 6, 329-351.

[18] Cortes-Salazar, F.; Momotenko, D.; Girault, H. H.; Lesch, A.; Wittstock, G. *Anal. Chem.* **2011**, 83, 1493-1499.

[19] Williams, C. G.; Edwards, M. A.; Colley, A. L.; Macpherson, J. V.; Unwin, P. R. *Anal. Chem.* **2009**, 81, 2486-2495.

[20] Ebejer, N.; Schnippering, M.; Colburn, A. W.; Edwards, M. A.; Unwin, P. R. *Anal. Chem.* **2010**, 82, 9141-9145.

[21] Rodolfa, K. T.; Bruckbauer, A.; Zhou, D. J.; Korchev, Y. E.; Klenerman, D. *Angew. Chem., Int. Ed.* **2005**, 44, 6854-6859.

[22] Rodolfa, K. T.; Bruckbauer, A.; Zhou, D. J.; Schevchuk, A. I.; Korchev, Y. E.; Klenerman, D. *Nano Lett.* **2006**, 6, 252-257.

[23] OConnell, M. A.; Snowden, M. E.; McKelvey, K.; Gayet, F.; Shirley, I.; Haddleton, D. M.; Unwin, P. R. *Langmuir* **2014**, 30, 10011-10018.

[24] Guell, A. G.; Ebejer, N.; Snowden, M. E.; Macpherson, J. V.; Unwin, P. R. *J. Am. Chem. Soc.* **2012**, 134, 7258-7261.

[25] Guell, A. G.; Meadows, K. E.; Dudin, P. V.; Ebejer, N.; Macpherson, J. V.; Unwin, P. R. *Nano Lett.* **2014**, 14, 220-224.

[26] Cortes-Salazar, F.; Lesch, A.; Momotenko, D.; Busnel, J.-M.; Wittstock, G.; Girault, H. H. *Anal. Methods* **2010**, 2, 817-823.

[27] Momotenko, D.; Cortes-Salazar, F.; Lesch, A.; Wittstock, G.; Girault, H. H. *Anal. Chem.* **2011**, 83, 5275-5282.

[28] Momotenko, D.; Qiao, L.; Cortes-Salazar, F.; Lesch, A.; Wittstock, G.; Gi-

rault, H. H. *Anal. Chem.* **2012**, 84, 6630-6637.

[29] Takahashi, Y.; Shevchuk, A. I.; Novak, P.; Zhang, Y.; Ebejer, N.; Macpherson, J. V.; Unwin, P. R.; Pollard, A. J.; Roy, D.; Clifford, C. A.; Shiku, H.; Matsue, T.; Klenerman, D.; Korchev, Y. E. *Angew. Chem., Int. Ed.* **2011**, 50, 9638-9642.

[30] McKelvey, K.; Nadappuram, B. P.; Actis, P.; Takahashi, Y.; Korchev, Y. E.; Matsue, T.; Robinson, C.; Unwin, P. R. *Anal. Chem.* **2013**, 85, 7519-7526.

[31] Nadappuram, B. P.; McKelvey, K.; Al Botros, R.; Colburn, A. W.; Unwin, P. R. *Anal. Chem.* **2013**, 85, 8070-8074.

[32] Thakar, R.; Weber, A. E.; Morris, C. A.; Baker, L. A. *Analyst* **2013**, 138, 5973-5982.

[33] Macpherson, J. V.; Simjee, N.; Unwin, P. R. *Electrochim. Acta* **2001**, 47, 29-45.

[34] Snowden, M. E.; Guell, A. G.; Lai, S. C. S.; McKelvey, K.; Ebejer, N.; OConnell, M. A.; Colburn, A. W.; Unwin, P. R. *Anal. Chem.* **2012**, 84, 2483-2491.

[35] Lazenby, R. A.; McKelvey, K.; Peruffo, M.; Baghdadi, M.; Unwin, P. R. *J. Solid State Electrochem.* **2013**, 17, 2979-2987.

[36] Sun, P.; Laforge, F. O.; Mirkin, M. V. *Phys. Chem. Chem. Phys.* **2007**, 9, 802-823.

[37] Liu, C.; Bard, A. J. *Nat. Mater.* **2008**, 7, 506-509.

[38] Liu, C.; Bard, A. J. *J. Am. Chem. Soc.* **2009**, 131, 6397-6401.

[39] Baytekin, B.; Baytekin, T. H.; Grzybowski, B. A. *J. Am. Chem. Soc.* **2012**, 134, 7223-7226.

[40] Lin, Z.; Cheng, G.; Lee, S.; Pradel, K. C.; Wang, Z. L. *Adv. Mater.* **2014**, 26, 4690-4696.

[41] Jones, C. E.; Unwin, P. R.; Macpherson, J. V. *ChemPhysChem* **2003**, 4, 139-

146.

[42] Martin, R. D.; Unwin, P. R. *J. Electroanal. Chem.* **1997**, 439, 123-136.

[43] Ghilane, J.; Lagrost, C.; Hapiot, P. *Anal. Chem.* **2007**, 79, 7383- 7391.

[44] Carano, M.; Bond, A. M. *Aust. J. Chem.* **2007**, 60, 29-34.

[45] Laforge, F. O.; Velmurugan, J.; Wang, Y.; Mirkin, M. V. *Anal. Chem.* **2009**, 81, 3143-3150.

[46] Actis, P.; Tokar, S.; Clausmeyer, J.; Babakinejad, B.; Mikhaleva, S.; Cornut, R.; Takahashi, Y.; Cordoba, A. L.; Novak, P.; Shevchuck, A. I.; Dougan, J. A.; Kazarian, S. G.; Gorelkin, P. V.; Erofeev, A. S.; Yaminsky, I. V.; Unwin, P. R.; Schuhmann, W.; Klenerman, D.;Rusakov, D. A.; Sviderskaya, E. V.; Korchev, Y. E. *ACS Nano* **2014**, 8, 875-884.

Chapter 6

Single Molecule Electrochemical Detection

Single molecule electrochemical detection (SMED) is an extremely challenging aspect of electroanalytical chemistry, requiring unconventional electrochemical cells and measurements. This chapter describes a new method of SMED using a quad-probe (4-channel probe) pipet cell, fabricated by depositing carbon pyrolytically into two diagonally opposite barrels of a laser-pulled quartz quadruple-barreled pipet and filling the open channels with electrolyte solution, and quasi-reference counter electrodes. A meniscus forms at the end of the probe covering the two working electrodes, and is brought into contact with a substrate working electrode surface. In this way, a nanogap cell is produced whereby the two carbon electrodes in the pipet can be used to promote redox cycling of an individual molecule with the substrate. Anti-correlated currents generated at the substrate and tip electrodes, at particular distances (typically 10s of nanometers) are consistent with the detection of single molecules. The low background noise realized in this droplet format opens up new opportunities in single molecule electrochemistry, including the use of ionic liquids, as well as aqueous solution, and the quantitative assessment and analysis of factors influencing redox cycling currents, due to a precisely known gap size.

6.1 Introduction

The detection and investigation of a single molecule diffusing freely in solution is at the forefront of emerging electro-chemical and optical analytical detection techniques.[1,2] However, while optical methods have evolved into spectroscopic techniques,[3] electrochemical methods on the other hand have remained much more limited. A major challenge in these systems is the spatial localization of a single molecule for sufficient time to permit interrogation.[4] Single molecule electrochemical detection (SMED) offers significant opportunity for fundamental studies of homogeneous and heterogeneous charge transfer, with implications for sensing, energy conversion and storage, and biological processes. Yet, with few methods available for isolating an individual molecule and measuring charge transfer at an electrode, the number of examples of SMED is small despite two decades of effort.[1,58]

To measure the electrochemical current produced by an individual molecule, it is necessary to amplify the signal through redox cycling.[5] In this process, a single redox active molecule is isolated between two closely spaced electrodes (several tens of nanometers or less) where one electrode is held at an oxidizing potential and the other at a reducing potential with respect to a redox couple of interest. The same single molecule moves rapidly back and forth between the two electrodes undergoing tens of thousands (or more) charge transfer events per second, thereby generating a tiny, but measureable, current. Initial demonstrations of SMED used a tip ultramicroelectrode (UME) that was held at a potential to oxidize a probe molecule and positioned close (estimated to be $\sim$ 10 nm) to a substrate electrode using a scanning electrochemical microscopy (SECM) format. The substrate was

held at a reducing potential to promote redox cycling between the tip and substrate electrodes.[5] Intermittent peaks in electrochemical current at the tip were attributed to an individual molecule that became temporarily located, and shuttled, between the UME and substrate electrodes. In this configuration, measurements were limited to the tip electrode as the background noise level was too large to measure the redox cycling current at the substrate working electrode. These measurements were recognized to be extremely challenging,[9] and more recently, Lemay and coworkers[1,8] used a microfabricated thin layer cell, which contained two high surface area electrodes separated by a fixed distance, typically 40 - 70 nm, through which dilute solutions of a redox mediator were flowed, allowing for the detection of individual molecules, or small groups of molecules, as they occasionally entered into the cell and underwent redox cycling. A significant attribute of these latter studies was that the electrochemical current was measured separately at each electrode. This allowed for the measurement of the anti-correlated current (oxidation and reduction) at each electrode, confirming the occurrence of redox cycling of a single molecule. For this experimental arrangement it was found that adsorption of the probe molecule at the electrodes played a significant role and dramatically reduced the expected redox cycling efficiency, demonstrating that single molecule measurements could also act as local probes of their environment. However, these electrochemical cells are non-trivial to fabricate and use, and, to date, single molecule measurements have relied exclusively on the use of noble metals such as Pt or Au as working electrodes and solvents where the diffusion coefficient is high.[1,58]

In this work, we use a simple new cell design for SMED that employs an easily prepared four channel micropipet, referred to as a quad-probe[10] that is ap-

proximately 3 μm in total diameter and used to form a droplet electrochemical cell that can be brought into contact with any working electrode substrate, greatly expanding the range of SMED systems that can be explored. The individual channels within the quad-probe were approximately 1 μm or less in size, depending on the overall probe diameter. Two of the four channels were filled with electrolyte solution and Ag/AgCl quasi-reference counter electrodes (QRCEs). The other two channels were filled with pyrolyzed carbon[11-13] to create two further working microelectrodes that could be used to promote redox cycling with a substrate working electrode (Figure 6.1A). The low surface area of the carbon microelectrodes greatly enhances the electrochemical signal to noise ratio. By further confining the volume of our measurements to a droplet formed at the end of the pipet we achieve unprecedented low noise levels of only a few fA at each of the working electrodes. This makes possible the correlation of the electrochemical current generated at the tip and substrate and allows for the creation of nano-gap electrochemical cells with highly controllable and variable height that can be used to trap and detect individual molecules. As a consequence of the exceptionally low noise levels achieved herein, we show for the first time the ability to detect and analyze the redox cycling of an individual molecule in a viscous ionic liquid, opening up new prospects in SMED.

6.2 Materials and Methods

6.2.1 Materials and Reagents

Ferrocenylmethyltrimethylammonium ($FcTMA^+$) hexafluorophosphate was prepared in house from the metathesis of ferrocenyltrimethylammonium iodide (Strem Chemicals) and silver hexafluorophosphate (Strem Chemicals).[14] Phosphate buffer solution (PBS) (pH 7.2, Sigma Aldrich), potassium chloride (AR grade, Sigma Aldrich), hexaammineruthenium (III) ($Ru(NH_3)_6{}^{3+}$) chloride (98%, Acros Organics), and 1-butyl-3-methylimidazolium tetrafluoroborate [BMIM][BF_4] (HPLC grade, Sigma Aldrich) were used as received. Multibore quartz quadruple-barreled capillaries (30 cm length, 1.57 mm outer diameter, 0.381 mm inner diameter) were cut into 4 equal length parts (MBT-015-062-4Q, Friedrich and Dimmock, Inc.).

6.2.2 Quad Probe Fabrication

Two types of quad probe electrodes were used in this work including, a quad-barrel probe with coplanar carbon electrodes (Figure 6.1B) and a modified probe where the carbon electrodes protruded slightly from the end of the pipet (Figure 6.1C). A quartz quadruple-barreled capillary was pulled to a small tip diameter ($\sim$ 2-3 μm) using a laser puller (P-2000, Sutter Instruments) to produce a quad-probe with four open barrels that were each approximately 1 μm across. Two of the four barrels (diagonally opposed) of the pulled pipet were filled with pyrolytic carbon using butane gas as a carbon source.[10-13] Gallium ions (Ga^+) were used to mill the end of the pipet by a focused ion beam (FIB) (JEOL 4500, JEOL), resulting in 2 electrodes, that could be used for single molecule redox cycling with the substrate

electrode. Focused ion beam milling could also be used to control the extent of carbon protrusion at the ends of the quad-probe tips, as it was found that quartz was removed at a faster rate than carbon, allowing for the formation of probes where carbon protruded from the ends (Figure 6.1C).

6.2.3 Electrochemical Measurements

All electrochemical measurements were performed using the WEC-SM platform described on Chapter 2. A four electrode configuration (Figure 1a) was used comprising a tip working electrode formed by connecting the two carbon electrodes in series (copper wire) and measuring the total current at them. This was done to increase the overall electrode area for detection of the electrochemical current generated by redox cycling, but in future work these electrodes could be individually addresable.[10] The two open barrels were filled with a solution of interest along with two QRCEs (either Ag/AgCl or Ag wire). A small offset potential (typically 20 - 100 mV) was applied between the QRCEs, using a custom-built potentiostat. The potential between the two QRCEs in the barrels (V_1 and V_2) was controlled using a custom-built potentiostat. The resulting ion current was used as a feedback signal, [15,16] to detect meniscus contact with the working electrode substrate surface. The working electrode substrate surface was either a SPI-1 grade HOPG substrate (SPI supplies) or a Pt-coated glass slide. The potentials at the tip and substrate electrodes were precisely controlled via V_3 and V_4, as well as V_1 and V_2 (Figure 6.1A) and the working electrode currents (i_3 and i_4 in Figure 6.1A) were measured independently using custom-built electrometers. Initial current-to-voltage conversion took place in electrometer head units placed approximately 5

cm from the tip and substrate electrodes in order to minimize noise pick-up and input capacitance.

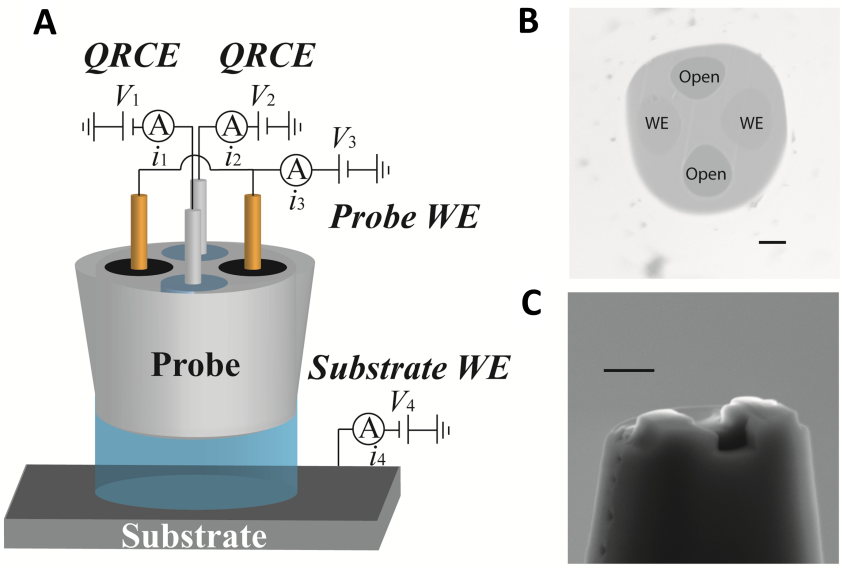

Figure 6.1: (A) Schematic of the electrode configuration: the carbon working electrodes in the barrel of the probe; two open barrels filled with electrolyte and AgCl-coated Ag wire QRCEs; and the substrate working electrode. The potentials of the two QRCEs (V_1 and V_2), were controlled using a custom-potentiostat, while the potential at the tip and substrate working electrodes, was controlled separately (V_3 and V_4 using independent electrometers. (B) SEM image (plan view) of a flat quad-probe, containing two carbon-filled and two open channels, that was milled with a focused ion beam. (C) SEM images of quad-probes where quartz was preferentially milled away to reveal protruding carbon electrodes. Scale bar in (B) and (C) is 500 nm.

The remote electrometer head units (each accurate to $\pm$ 10%) were connected to auto-ranging gain/control units capable of switching automatically over four decade ranges from 1 fA/V to 1 pA/V. Each gain/control unit incorporated a variable first-order low-pass filter to control higher frequency noise. Further noise

control was achieved using custom-built low-pass variable frequency eighth-order or sixteen-order brick wall filter units optimized for transient response and phase coherency. The time constants of the two filters were 100 ms and 50 ms.

Micro-positioners (M-461, Newport) were used for initial positioning of the pipette in combination with a picomotor piezo linear actuator (New Focus). The picomotor (30 nm resolution) was used for coarse approach and the LISA linear actuator used for fine positioning of the pipette. To bring the tip and the substrate into meniscus contact, the tip position was oscillated sinusoidally in the normal direction (80 nm peak-to-peak, 288 Hz), as the tip was translated towards the substrate, and an ac ion current based feedback control scheme was used.[15,16] Once meniscus contact was achieved, the AC oscillation and DC offset potential were switched off, as the tip continued to be slowly approached to the substrate until contact or until a desired distance, was achieved, so that the gap dimensions were known with high accuracy. An FPGA card (PCIe-7852R, National Instruments) with 16 bit analog input resolution was used for instrument control and data acquisition through a Labview interface. Fine positioning of the pipet perpendicular to the surface utilized a LISA linear actuator (P-753.1CD, PI) and controller (E665, PI) with a 15 μm extended travel providing a step resolution of 0.46 nm. The faraday cage in which the apparatus was placed contained vacuum insulated panels (Kevothermal) and aluminum heat sinks (Hamilton Sundstrand) for thermal insulation to minimize any drift of the z-piezo position. [17]

6.2.4 Random walk simulation

A three dimensional (3D) random walk simulation was used to determine the position of a single molecule within the droplet (molecule trapped in the thin meniscus between the tip and surface). For the random walk simulation it was assumed that the molecule could move in the ± x, ± y, or the ± z direction with equal probability for each step. A reflecting boundary, defined by the pipette diameter, substrate surface, and probe end was used to constrain the position of the molecule within the droplet, such that if the molecule position attempted to exceed these dimensions it was reflected back from the boundary. A step size of dr = 4.05 nm was used in the random walk simulation. This step is smaller than the tip-substrate separation (30 nm) for single molecule measurements and is significantly smaller than the diameter of an individual carbon microelectrode ($\sim$ 1 μm) or substrate ($\sim$ 3 μm) to allow adequate sampling of the nanogap geometry. The corresponding temporal step size was defined using dt = $(dr)^2/2D$, where D is the diffusion coefficient of $Ru(NH_3)_6^{2/3+}$ (8.2×10^{-6} cm^2 s^{-1}), giving dt = 10 ns. The temporal step size is 7 orders of magnitude smaller than the time constant of the electrometer (100 ms). Using these parameters, it was possible to accurately sample the 3D position of the molecule with sufficient spatial and temporal resolution over a reasonably long time period (100 ms) for comparison with experimental data.

A charge transfer event occurred each time an oxidized (reduced) molecule collided with the reducing (oxidizing) electrode. The active area of each disk electrode was defined by the diameter of the carbon UME (1 μm) for the oxidizing electrode, and the total probe diameter (3 μm) for the reducing electrode.

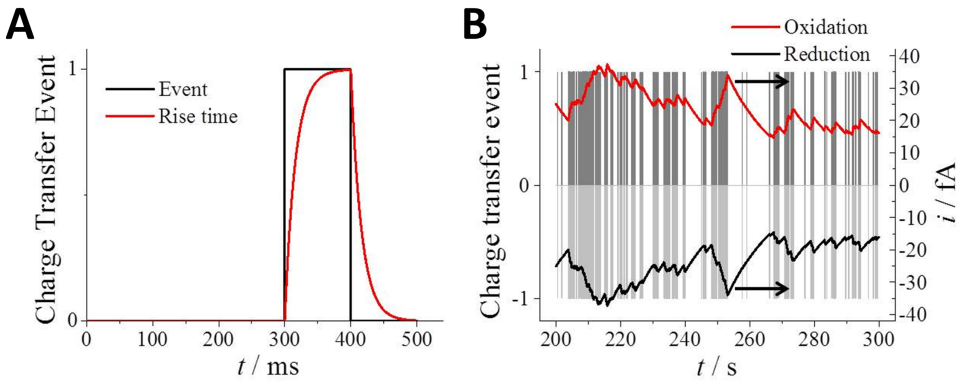

Figure 6.2: (A) Plot of charge transfer event (defined as 1 when an oxidized (reduced) molecule collides with the active area of the reducing (oxidizing) electrode, and zero otherwise) as a function of time (black line) and its convolution with the impulse function used to represent the rise time (100 ms) of electrometer (red line). (B) Charge transfer event (oxidation (dark gray) and reduction (light gray)) and corresponding electrochemical currents based on a 3D random walk.

For each charge transfer event the associated current was calculated as iredox = eD/z^2, where e is the charge of an electron, convolved with an instrument response function to generate the electrochemical current (Figure 6.2A). The following expression was used to represent the instrument response, $(2\pi/\tau)\exp(-2\pi/\tau)$, where τ is the time constant of the electrometer (100 ms), and was found to be a reasonable approximation for the 100 ms rise time. [4] This led to transients (current-time profiles) such as that shown in Figure 6.5C. Figure 6.2 shows an example of the impact of the instrument response for an individual event (Figure 6.2A) and current transients (Figure 6.2B) obtained by convolving the occupancy plot with the electrometer response. It can be seen from Figure 6.4 and Figure 6.2 B that the current magnitude and current-time course for a molecule trapped in the meniscus

is similar to that seen experimentally.

6.3 Results and Discussion

Figure 6.3 shows the evolution of the tip and substrate current (electrode potential of 0.000 vs. Ag wire QRCE) as a pipet (working electrode potential of + 0.500 vs Ag wire QRCE) containing a blank (BMIM)(BF_4) ionic liquid solvent was approached towards the surface after meniscus contact. The pipet probe was initially located ca. 150 nm from the Pt substrate electrode and approached towards the substrate at a constant velocity (7.5 nm s^{-1}) until a large jump in current was observed, corresponding to physical contact (short-circuit) between the probe and substrate. The simultaneously recorded tip/substrate currents (Figure 6.3A) and z-piezo position (Figure 6.3B) are both plotted as a function of time. A z-piezo position of zero is defined by the onset of physical contact between the probe and substrate. Knowledge of the exact position of tip-substrate contact was used to determine with high accuracy the inter-electrode separation distance for single molecule events. Figure 6.3C shows a zoom-in of the tip and substrate currents (Figure 6.3A) for a separation of less than 30 nm. The currents show extremely small background noise levels (ca. 1 fA) which are not correlated in time up until the onset of physical contact. The baseline noise level ($\sim$ 1 fA) represents an order of magnitude improvement compared to state-of-the-art microfabricated devices[1,8] ($\sim$ 10 fA) and a 2 order of magnitude improvement compared to SECM[57] (hundreds of fA).

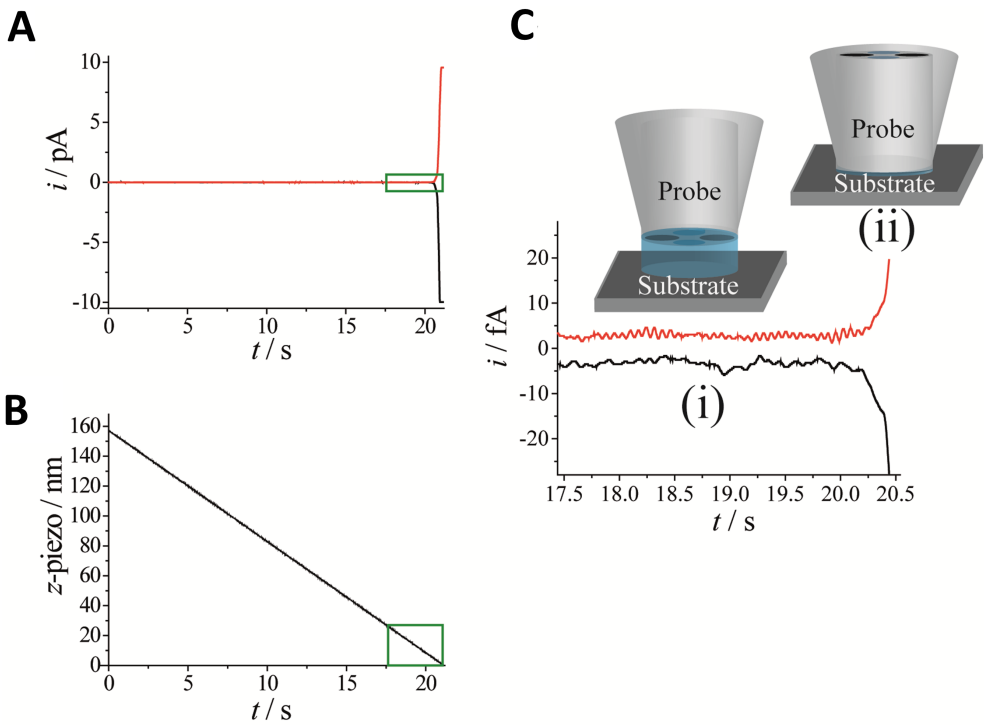

Figure 6.3: Approach curves for simultaneously acquired (A) tip (red line)/substrate (black line) current and (B) z-piezo position as a function of time. Approach rate was 7.5 nm sec^{-1}. The probe (working electrode potential of + 0.500 vs Ag wire QRCE) containing a blank (BMIM)(BF_4) ionic liquid solvent was approached towards the Pt substrate until a sharp rise in current was observed following physical contact of the tip and substrate (electrode potential of 0.000 vs. Ag wire QRCE). A z-piezo position of zero is defined by the onset of physical contact between the probe and substrate. (C) A zoom-in, highlighted by a green box in (A) and (B), illustrating the nanogap geometry formed (region i) for tip-substrate separations less than 30 nm and up until physical contact between the probe and substrate (region ii). For the blank (BMIM)(BF_4) the currents were uncorrelated and showed a low background noise of ca. 1 fA.

As a consequence of the small background noise, for regions very close to the substrate (less than 50 nm from contact), and using probes filled with sufficiently dilute concentrations of a redox couple, it was possible to detect the anti-correlated currents due to redox cycling of an individual molecule as shown further below.

SMED was realized separately in aqueous solution and in an ionic liquid solvent. The redox probe molecule used in aqueous solution was $Ru(NH_3)_6^{3+}$, which undergoes a simple one electron reduction. The supporting electrolyte was 25 mM KCl in 50 mM PBS. The HOPG substrate was used to generate $Ru(NH_3)_6^{2+}$ by holding the potential at a value (-0.450 V vs Ag/AgCl QRCE) that corresponded to the limiting current of $Ru(NH_3)_6^{3+}$ reduction, while the tip was held at 0.000 V and used for collection (oxidation of $Ru(NH_3)_6^{2+}$ to $Ru(NH_3)_6^{3+}$). Figure 6.4 shows the results of two different approaches that were used to detect an individual molecule. In the first case (Figure 6.4A), the probe was held at a known fixed distance (18 nm) above the substrate until redox cycling was detected at the tip and substrate electrodes. In the second case, redox cycling was observed after the tip was brought into contact with the substrate and then continuously retracted while a molecule was trapped within the droplet. In the upper panel of Figure 6.4, the current is plotted as a function of time while the z piezo position is plotted over the same period of time in the lower panel. A z piezo position of zero corresponds to initial tip-substrate contact as defined by the point where the current at both electrodes saturates and corresponds to the onset of their physical contact (Figure 6.3).

In Figure 6.4A, the solution in the probe contained 10 nM $Ru(NH_3)_6^{3+}$ in 25 mM KCl and PBS. The average number of molecules, N, expected for an 18 nm tip-substrate separation would be 0.76 leading to stochastic fluctuations in the

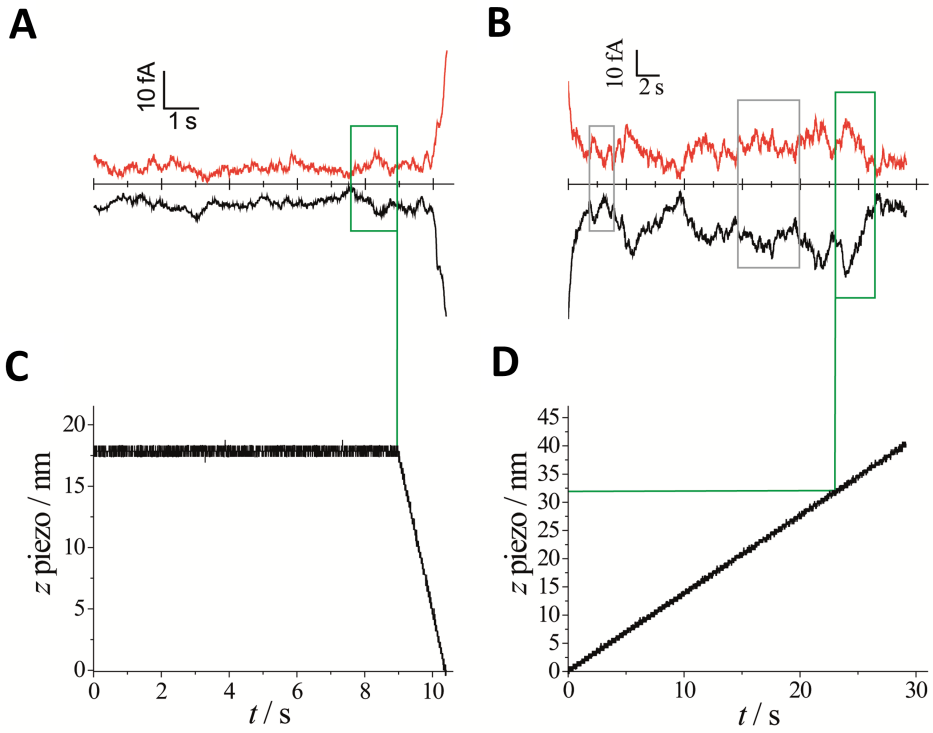

Figure 6.4: Single molecule measurements for a 10 nM aqueous solution of $Ru(NH_3)6^{3+}$ in 50 mM phosphate buffer solution and 25 mM KCl. The upper panels display the current and the lower panels display the corresponding z piezo position plotted as a function of time. The HOPG substrate was held at a reducing potential of - 0.450 V (vs Ag/AgCl QRCE) and the tip electrode was held at 0.000 V (vs Ag/AgCl QRCE) and used for oxidation. (A) The redox cycling of a $Ru(NH_3)_6^{3+/2+}$ molecule can be seen ca. 18 nm away from the tip-substrate contact point (highlighted in green dashed box) while the z piezo position was constant. Following the redox cycling event, the tip was approached towards the substrate (translation rate 12.5 nm s^{-1}) until contact to determine the exact tip-substrate separation. (B) Anti-correlated current spikes were observed at both substrate and tip (grey and green dashed boxes) with maximal current values of ca. 30 fA as the tip was retracted from the substrate surface at a constant velocity (translation rate 1.25 nm s^{-1}).

measured electrochemical current. [4,18] Evidently a single molecule enters into the droplet at ca. 7 seconds. Up until this time, the measured current, which showed small fluctuations, was uncorrelated. However, at times longer than 7 seconds, the tip and substrate display anti-correlated currents, with the substrate (-0.450 V vs Ag/AgCl QRCE) showing transient increases in cathodic current and the tip (+ 0.000 V vs Ag/AgCl QRCE) showing corresponding increases in the anodic current that are anti-correlated in magnitude and time, consistent with redox cycling.1,8 Following the detection of this event, the tip was approached towards the substrate (approach rate 12.5 nm s^{-1}) and stopped as soon as tip-substrate contact was detected to determine precisely the exact tip-substrate separation for the single molecule event highlighted. Subsequently, the tip was retracted (retract rate 1.25 nm s^{-1}) from the substrate and the corresponding current transients are shown in Figure 6.4B as the tip moved away from the substrate at a constant velocity. Again, the current shows anti-correlated behaviour with several distinct peaks observed whose duration was much longer than the time constant of the electrometer (100 ms). These features can be attributed to the cycling of an individual molecule between the tip and substrate with a few events occurring for a sufficient time to be clearly resolved, as highlighted by the green box in Figure 6.4B. The duration of this current enhancement was approximately one second, during which the current peaked and plateaued with a magnitude of ca. 30 fA, compared to the baseline at larger tip-substrate separations.

For a 30 nm tip-substrate separation, we would have expected to observe 146 fA per molecule (assuming the current $i_{\mathrm{redox}} = eD/z^2$ where e is the charge of an electron, D the diffusion coefficient, which is 8.2 x 10^{-6} cm^2 s^{-1} for $Ru(NH_3)_6^{3+/2+}$ in water,[19] and z is the tip-substrate separation). The reduced magnitude of the

measured currents for single molecule redox cycling has been previously attributed to adsorption of the molecule at the electrodes.[20,21] However, for the studies herein, we also have to consider inactive regions across the tip surface, as discussed further below. For such small current measurements the electrometer response function also attenuates the signal. Overall, the measured current values are consistent with recent reports of single molecule cycling in a nanogap thin layer cell where a comparable diminution in current magnitude was observed in aqueous conditions.[1]

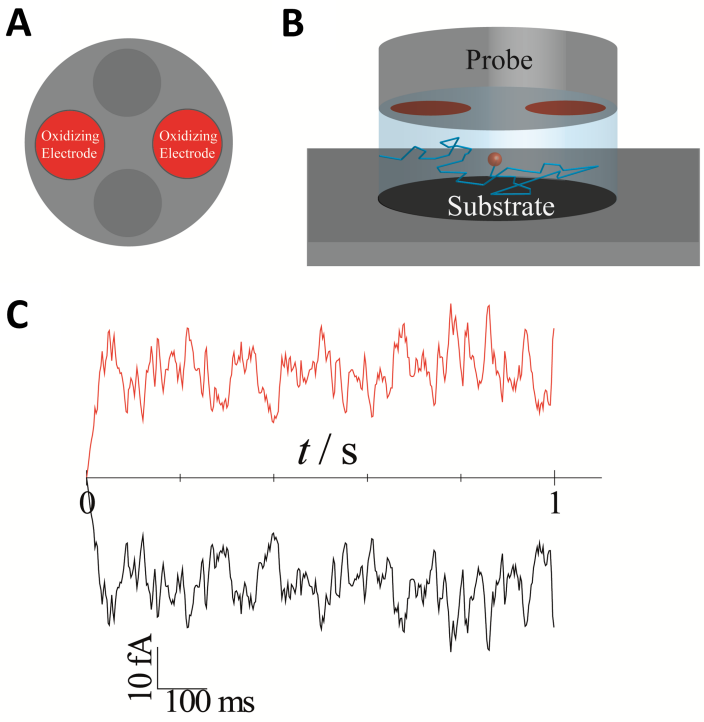

Figure 6.5: (A) 2D Schematic of the probe electrode illustrating the active oxidizing electrode (red) and inactive (gray) areas. (B) 3D geometry for the random walk simulation where a single molecule was positioned in the center of the droplet at t = 0. Red areas (probe) correspond to the oxidizing electrode and black area (substrate) corresponds to the reducing electrode. (C) Current transients based on 3D random walk simulation for a tip-substrate separation of 30 nm.

For tip-substrate separations of less than 40 nm many sharp distinct anti-correlated events can be resolved, which, due to the low background noise level ($\sim$ few fA) obtainable in this configuration, provides an order of magnitude increase in the signal-to-noise ratio compared with previous measurements.[1,58] Several events are highlighted in Figure 6.4B with gray and green dashed boxes. Events highlighted in gray boxes correspond to cases where the molecule rapidly cycles between the two active electrodes for short periods of time before leaving the active region briefly and then returning due to the random walk of the molecule in the meniscus droplet. While the HOPG substrate is uniformly active, the tip contains some areas where cycling does not occur such as the glass outer diameter and inner septum as well as the open barrels (Figure 6.5A). A three dimensional random walk simulation (Figure 6.5) was used to map the movement of a molecule confined within a closed system[22] (i.e. the molecule could not escape up the open barrels) within the droplet that takes into account a reduced active area at the probe. For the simulation, the substrate was assumed to be uniformly active while only the carbon UMEs were assumed to be active for the probe end (Figure 6.5A). A charge transfer event occurred for each instance that an oxidized molecule reached the substrate working electrode boundary, and, similarly, a charge transfer event occurred each time a reduced molecule contacted the active area of one of the carbon UMEs. Figure 6.5C illustrates the electrochemical current generated by a single molecule trapped within the droplet over a 100 ms time period whose profile has been modulated by the electrometer response time. At time t = 0, a single molecule is located directly in the center of the droplet (Figure 6.5B), which then undergoes a random walk for a period of 100 ms. Figure 6.5C shows the evolution of the electrochemical current, where initially it was zero at time t = 0 (molecule

located in the center of the droplet), and then increases as the molecule undergoes a random walk throughout the droplet volume. It can be seen that many brief events occur that are much shorter than the time constant of the electrometer (100 ms), which leads to sharp peaks and variations in current that do not reach the theoretical maximum current for uniformly active electrodes (146 fA for z = 30 nm). Significantly, the associated current profiles and magnitudes (Figure 6.5C) resemble the experimental current transients measured in Figure 6.4.

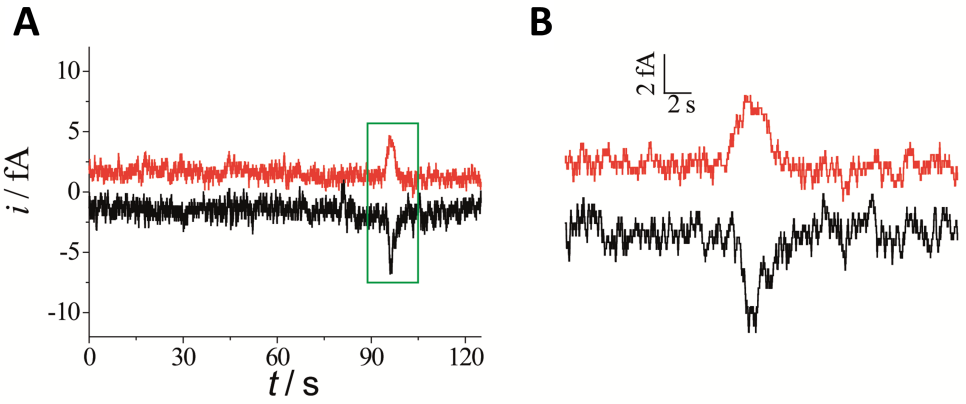

Figure 6.6: (A) Current-time plot for a solution containing 100 nm $FcTMA^+$ in (BMIM)(BF_4) at a constant z piezo position. A redox cycling event highlighted by the green box is shown as a zoom-in (B). The tip electrode was held at + 0.500 V (vs Ag wire QRCE) to generate $FcTMA^{2+}$ and a Pt substrate was held at a reducing potential of 0.000 V (vs Ag wire QRCE) to regenerate $FcTMA^+$.

Single molecule measurements in an ionic liquid have not yet been possible due to the exceptionally low diffusion coefficients realized in such relatively viscous media, [23-25] resulting in current magnitudes that would be too small to be clearly resolved by previous techniques. Using our configuration it was possible to

achieve background noise levels of a femtoampere or less (Figure 6.2D) allowing us to detect events with current magnitude of only a few femtoamperes, which is unprecedented in electrochemistry. Measurements were carried out using the ionic liquid (BMIM)(BF_4), and 100 nM $FcTMA^+$ as a redox probe and a quad-probe containing protruding carbon working electrodes (Figure 1c). The tip working electrode was held at an oxidizing potential (+ 0.500 V vs. Ag wire QRCE) to generate $FcTMA^{2+}$ and approached to a Pt substrate that was held at a reducing potential for collection (0.000 V vs. Ag wire QRCE). For these measurements the tip was brought into contact with the substrate, withdrawn 10 nm from the surface, and then held at a fixed distance while the tip and substrate currents were recorded. Figure 6.6A shows current time plots for the tip and substrate working electrodes over a period of several minutes. These data highlight the very stable and low background currents that prevail over extended periods. A redox cycling event is highlighted by a green box (Figure 6.6A) with a zoom-in shown in Figure 6.6B. At the end of the measurement (within 60 s of the single molecule event), the tip-substrate separation for the highlighted single molecule event (34 nm) was determined by approaching the tip towards the substrate until physical contact was made.

The peak currents at both the tip and substrate working electrodes ($\sim$ 4 fA) could be clearly resolved from the background current ($\sim$ 1 fA) allowing us to detect the redox cycling of a single molecule ($FcTMA^+/FcTMA^{2+}$) in an ionic liquid for the first time. The diffusion coefficient of $FcTMA^+$ was measured using a 25 μm diameter Pt UME in bulk solution and found to be 8 x 10^{-8} cm^2 s^{-1}. In this case, a peak current of 1.1 fA would have been expected for a single molecule randomly diffusing between two electrodes for a tip-substrate separation of 34

nm. The higher current value would suggest that the simple description based on diffusion in a thin layer cell, free from migration, may not fully account for the expected electrochemical current in an ionic liquid for such a confined geometry. Considerable discussion[28-31] has centered around the extent of ion dissociation in ionic liquids following a recent assertion that they should be considered as dilute electrolytes[32] resulting in a diffuse layer that could extend out to 10 nm or more from the electrode/ionic liquid interface. The resulting electric field across the nanogap would result in a larger than expected limiting current due to the small electrode spacing. [33] In fact, it has been shown in aqueous solution that redox cycling without supporting electrolyte can lead to a 2000-fold enhancement of the limiting current as a result of migration due to the electric field between the generator and collector electrodes. [34] The results herein highlight a significant, but more moderate effect, and suggest a diffuse layer effect that impacts mass transport in the nanogap geometry. Considering the large overall electric field that would exist across the gap in the absence of supporting electrolyte ($\sim$ 1.5 GV cm^{-1}), a diffuse layer that extends only a few nm from the surface could have a significant impact in such a confined geometry, making it quite reasonable to expect migration to play a role in this configuration and contribute to the enhanced current observed here.

Scanning electron microscope images of the probe along with the corresponding footprint created on the substrate due to probe contact are shown in Figures 6.7A and 6.7B. The droplet size on the substrate can be assumed to correspond to the size of the footprint during measurement as the low vapor pressure of the ionic liquid at atmospheric pressure and under vacuum (SEM) lead to negligible solvent evaporation.[26,27] The outline of the probe (Figure 6.7A) and droplet

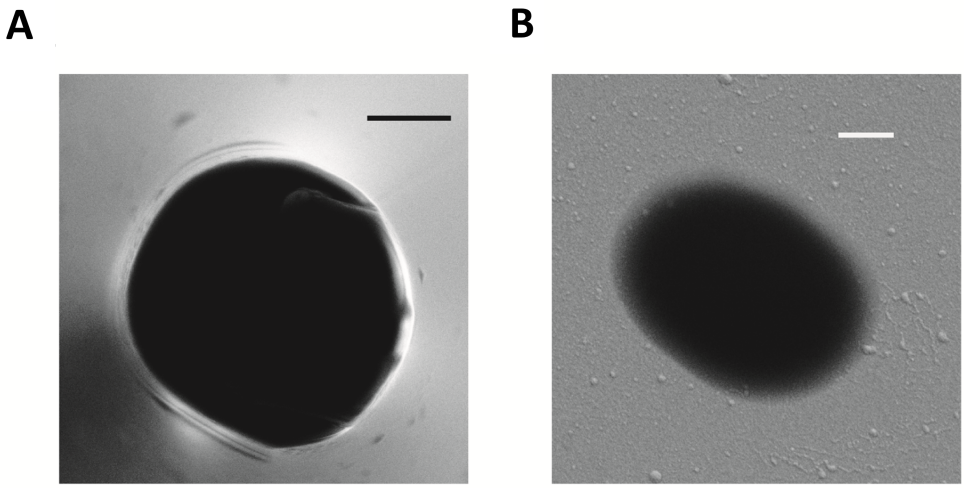

Figure 6.7: Plan-view SEM image of (A) probe used for single molecule measurements in Figure 5 and (B) corresponding footprint left behind by (BMIM)(BF_4) ionic liquid on the Pt substrate. Scale bar is 1 μm in (A) and (B).

(Figure 6.7B) are similar in size and shape with the droplet showing slightly increased dimensions due to a combination of surface wetting and solution spreading as the probe was brought into contact with the substrate. Overall, the droplet size reflects closely that of the probe, highlighting the well-defined geometry realized using this method.

6.4 Conclusions

The detection of single molecules in aqueous and ionic liquid solvents has been demonstrated using a simple droplet based approach. A significant advantage of this method is the ability to characterize the tip-substrate separation and electrode

area directly, instead of relying on the redox electrochemical signal itself, as in some past work, which provides an indirect estimate of these parameters. The currents generated during SMED were supported by a random walk simulation (3D), which indicates that the molecule rapidly explores the entire volume of the droplet. Single molecule measurements, to date, have been carried out using an electrode potential corresponding to the limiting current to maximize signal generation as also used herein.

In the future, by increasing the probe electrode area in combination with the high sensitivity capability realized here, potential dependent measurements could become possible. Moreover, in an alternative configuration where the carbon probe electrodes are not shorted together, but the electrodes are independently addressable, it would become possible to measure the spatial location of a molecule in addition to redox cycling. It is further important to point out that, the carbon pipet electrodes can be readily functionalized via a variety of methods.[10,12,13,35-38]

There are several more opportunities that could be explored further using the set-up for SMED demonstrated here. For example, the ion flux through the electrolyte-filled barrels, which is dependent on the dc bias applied across them,[39,40] can be used to control the flux of charged species within the droplet meniscus and effect the frequency of events occurring similar to a microfluidic configuration where the flow rate can be used for this purpose.[4] Most importantly, the ability to control the tip-substrate distance and measure the anti-correlated currents between the tip and substrate, as a function of tip-substrate separation, offers new opportunities for fundamental studies of the redox cycling of individual molecules under a variety of conditions and at different substrates, as the probe can be used to approach essentially any surface. Given the exceptionally low noise ($\sim$1

fA) combined with the ability to create extremely small gaps this probe electrode configuration should allow the influence of the double layer between two closely spaced electrodes to be investigated, where distance-dependent solvent structure effects may be manifested as revealed using ionic liquids. For these systems it has been found that mass transport perpendicular to the electrodes is enhanced by electric field effects. This opens up opportunities for fundamental studies of this type using the approach outlined here.

6.5 References

[1]Kang, S.; Nieuwenhuis, A. F.; Mathwig, K.; Mampallil, D.; Lemay, S. G. *ACS Nano* **2013**, 7, 10931.

[2] Schlau-Cohen, G. S.; Bockenhauer, S.; Wang, Q.; Moerner, W. E. *Chem. Sci.* **2014**, 5, 2933.

[3] Lord, S. J.; Lee, H. D.; Moerner, W. E. *Anal. Chem.* **2010**, 82, 2192.

[4] Singh, P. S.; Ktelhn, E.; Mathwig, K.; Wolfrum, B.; Lemay, S. G. *ACS Nano* **2012**, 6, 9662.

[5] Fan, F.-R. F.; Bard, A. J. *Science* **1995**, 267, 871.

[6] Fan, F.-R. F.; Kwak, J.; Bard, A. J. *J. Am. Chem. Soc.* 1996, 118, 9669.

[7] Sun, P.; Mirkin, M. V. J. Am. *Chem. Soc.* **2008**, 130, 8241.

[8] Zevenbergen, M. A. G.; Singh, P. S.; Goluch, E. D.; Wolfrum, B. L.; Lemay, S. G. *Nano Lett.* **2011**, 11, 2881.

[9] Lemay, S. G.; Kang, S.; Mathwig, K.; Singh, P. S. *Acc. Chem. Res.* **2013**, 46, 369.

[10] Nadappuram, B. P.; McKelvey, K.; Byers, J. C.; Gell, A. G.; Colburn, A. W.; Lazenby, R. A.; Unwin, P. R. *Anal. Chem.* **2015**, 87, 3566.

[11] Takahashi, Y.; Shevchuk, A. I.; Novak, P.; Zhang, Y.; Ebejer, N.; Macpherson, J. V; Unwin, P. R.; Pollard, A. J.; Roy, D.; Clifford, C. A.; Shiku, H.; Matsue, T.; Klenerman, D.; Korchev, Y. E. *Angew. Chem. Int. Ed. Engl.* **2011**, 50, 9638.

[12] McKelvey, K.; Nadappuram, B. P.; Actis, P.; Takahashi, Y.; Korchev, Y. E.; Matsue, T.; Robinson, C.; Unwin, P. R. *Anal. Chem.* **2013**, 85, 7519.

[13] Nadappuram, B. P.; McKelvey, K.; Al Botros, R.; Colburn, A. W.; Unwin, P. R. *Anal. Chem.* **2013**, 85, 8070.

[14] Bertoncello, P.; Ciani, I.; Li, F.; Unwin, P. R. *Langmuir* **2006**, 22, 10380.

[15] Ebejer, N.; Schnippering, M.; Colburn, A. W.; Edwards, M. A.; Unwin, P. R. *Anal. Chem.* **2010**, 82, 9141.

[16] Ebejer, N.; Gell, A. G.; Lai, S. C. S.; McKelvey, K.; Snowden, M. E.; Unwin, P. R. *Annu. Rev. Anal. Chem.* **2013**, 6, 329.

[17] Kim, J.; Shen, M.; Nioradze, N.; Amemiya, S. *Anal. Chem.* **2012**, 84, 3489.

[18] Bard, A. J.; Fan, F.-R. F. *Acc. Chem. Res.* **1996**, 29, 572.

[19] Gell, A. G.; Ebejer, N.; Snowden, M. E.; McKelvey, K.; Macpherson, J. V; Unwin, P. R. *Proc. Natl. Acad. Sci. U. S. A.* **2012**, 109, 11487.

[20] Ktelhn, E.; Krause, K. J.; Mathwig, K.; Lemay, S. G.; Wolfrum, B. *ACS Nano* **2014**, 8, 4924.

[21] Mampallil, D.; Mathwig, K.; Kang, S.; Lemay, S. G. J. *Phys. Chem. Lett.* **2014**, 5, 636.

[22] Feldberg, S. W.; Edwards, M. A. *Anal. Chem.* **2015**, 87, 3778.

[23] Carano, M.; Bond, A. M. *Aust. J. Chem.* **2007**, 60, 29.

[24] Walsh, D. A.; Lovelock, K. R. J.; Licence, P. *Chem. Soc. Rev.* **2010**, 39, 4185.

[25] Lovelock, K. R. J.; Cowling, F. N.; Taylor, A. W.; Licence, P.; Walsh, D. A. *J. Phys. Chem. B* 2010, 114, 4442.

[26] Armstrong, J. P.; Hurst, C.; Jones, R. G.; Licence, P.; Lovelock, K. R. J.; Satterley, C. J.; Villar-Garcia, I. J. *Phys. Chem. Chem. Phys.* **2007**, 9, 982.

[27] Arimoto, S.; Oyamatsu, D.; Torimoto, T.; Kuwabata, S. *ChemPhysChem* **2008**, 9, 763.

[28] Perkin, S.; Salanne, M.; Madden, P.; Lynden-Bell, R. *Proc. Natl. Acad. Sci. U. S. A.* **2013**, 110, E4121.

[29] Gebbie, M. A.; Valtiner, M.; Banquy, X.; Henderson, W. A.; Israelachvili, J. N. *Proc. Natl. Acad. Sci.* **2013**, 110, E4122.

[30] Yochelis, A. *Phys. Chem. Chem. Phys.* 2014, 16, 2836.

[31] Lee, A. A.; Vella, D.; Perkin, S.; Goriely, A. J. *Phys. Chem. Lett.* **2015**, 6, 159.

[32] Gebbie, M. A.; Valtiner, M.; Banquy, X.; Fox, E. T.; Henderson, W. A.; Israelachvili, J. N. *Proc. Natl. Acad. Sci.* 2013, 110, 9674.

[33] Gebbie, M. A.; Dobbs, H. A.; Valtiner, M.; Israelachvili, J. N. *Proc. Natl. Acad. Sci. U. S. A.* **2015**, 112, 7432.

[34] Ma, C.; Contento, N. M.; Bohn, P. W. *J. Am. Chem. Soc.* **2014**, 136, 7225.

[35] Actis, P.; Tokar, S.; Clausmeyer, J.; Babakinejad, B.; Mikhaleva, S.; Cornut, R.; Takahashi, Y.; Lpez Crdoba, A.; Novak, P.; Shevchuck, A. I.; Dougan, J. A.; Kazarian, S. G.; Gorelkin, P. V; Erofeev, A. S.; Yaminsky, I. V; Unwin, P. R.; Schuhmann, W.; Klenerman, D.; Rusakov, D. A.; Sviderskaya, E. V; Korchev, Y. E. *ACS Nano* **2014**, 8, 875.

[36] Clausmeyer, J.; Actis, P.; Lpez Crdoba, A.; Korchev, Y.; Schuhmann, W. *Electrochem. Commun.* 2014, 40, 28.

[37] Blanger, D.; Pinson, J. *Chem. Soc. Rev.* **2011**, 40, 3995.

[38] Kranz, C. *Analyst* 2014, 139, 336.

[39] Snowden, M. E.; Gell, A. G.; Lai, S. C. S.; McKelvey, K.; Ebejer, N.; OConnell, M. A.; Colburn, A. W.; Unwin, P. R. *Anal. Chem.* **2012**, 84, 2483.

[40] OConnell, M. A.; Snowden, M. E.; McKelvey, K.; Gayet, F.; Shirley, I.; Haddleton, D. M.; Unwin, P. R. *Langmuir* **2014**, 30, 10011.

Chapter 7

A new approach for the fabrication of microscale lipid bilayers at glass pipets: application to quantitative passive permeation visualization

A new method of planar bilayer lipid membrane (BLM) formation is presented that allows stable, solvent-free lipid bilayers exhibiting high seal resistances to be formed rapidly, easily and reproducibly. Using these bilayers the passive permeation of a series of carboxylic acids is investigated, to determine quantitatively the trend in permeability with lipophilicity of the acid. BLMs are formed at the tip openings of pulled theta pipets, and the rate of permeation of each carboxylic acid across the bilayer, from within the pipet into the bulk solution is determined. This is achieved through spatially-resolved measurements of the pH change that occurs upon the permeation of the weak acid, visualized using a pH-sensitive fluorophore with a confocal laser scanning microscope. The extracted fluorescence profiles are matched to finite element method (FEM) simulations, to allow the associated per-

meation coefficient for each weak acid to be determined with high accuracy, since this is the only adjustable parameter used to fit the experimental data. For bilayers formed in this way, the weak acids show increasing permeability with lipophilicity. Furthermore, the arrangement allows the effect of a trans-membrane electric field on permeation to be explored. For both propanoic and hexanoic acid it is found that an applied electric field enhances molecular transport, which is attributed to the formation of pores within the membrane.

7.1 Introduction

Planar lipid bilayers have been used extensively as model cell membranes for the study of passive permeation processes for many years.[1-8] Passive permeation across the cell membrane is of particular interest since most drug compounds are transported via this mechanism, and, as such, planar lipid bilayers are used in both high throughput drug screening[9-11] and more detailed studies to identify trends in permeation rates between molecules,[2,3,5,6] in addition to studies of charge transfer across the membrane.[12,13] Permeation coefficients of small molecules have commonly been analyzed using Overton's rule,[14] which considers the permeation coefficient, P, of a molecule transported across a membrane between two aqueous solutions to be proportional to the product of the partition coefficient, K, and diffusion coefficient, D, of the molecule in the membrane.[15] There has, however, been some debate as to whether this simplistic view of the permeation process is sufficient to describe the permeation of all small molecules, since it does not take into account the amphipathic nature of the phospholipids in a lipid bilayer. Whilst the majority of studies show a positive correlation between lipophilicity and permeation rate, the relationship is often not linear[4,16] and there is considerable variation in the P values reported for the same molecules.[2,3,5,7] Some studies have observed contrasting trends for the same series of molecules, suggesting that permeation processes may be more complex.[1,17] However, several of the existing experimental techniques are limited in the range of permeation coefficients that may be measured accurately. Moreover, the method of bilayer production may affect the properties of the membrane formed, which may in turn influence the permeation process.[18] One of the most widely used procedures, the painting method,[19] produces lipid bilay-

ers which contain residual solvent molecules in the interior of the bilayer, raising questions about the integrity and reliability of such model membranes.[20] Other methods produce bilayers with little or no residual solvent,[21] but these may have comparatively short lifetimes.[22] Improvements in bilayer lipid membrane (BLM) stability have been achieved through the use of gel-phase materials such as agarose which have produced bilayers that are extremely durable.[23-27] However, due to the slow diffusion of analytes through the gel, the temporal responses are very slow.[28] The use of small apertures, over which a bilayer is suspended, can also improve electrical and mechanical stability.[29,30]

Liposomes have also been used, which do not contain any residual solvent molecules in the interior of the membrane, and are typically stable for considerably longer periods than planar lipid bilayers.[31] However, since the interior of the liposome is inaccessible for sampling, measurement of permeation rates can be difficult. Recently confocal laser scanning microscopy (CLSM) has been employed to give increased resolution of the permeation of molecules into a single liposome.[32] Using this technique, it is possible to study not only fluorescent permeants but also weak acids, by means of a pH-sensitive fluorophore, enabling visualization of local pH changes as the molecule permeates either into a liposome[16] or, as originally reported, across a planar lipid bilayer.[1]

Here, we report on the use of dual-barrel theta capillaries for the formation of stable, solvent-free, suspended BLMs. This could be viewed as a modification of the tip-dip method reported previously,[22,33,34] wherein a monolayer is formed at the end of a pipet by moving the pipet out and into a solution that contains a lipid monolayer at the air-water interface, but herein, the monolayer is formed directly from a lipid solution. Long lasting bilayers that are formed simply, quickly and

reproducibly with high success rate (nearly 100%) (exhibit resistances up to 600 GΩ). Using this system, we determine the permeation coefficients of a series of aliphatic carboxylic acids as they passively permeate across a bilayer. By using CLSM with a pH-sensitive fluorophore,[1,16] the movement of these molecules can be tracked by monitoring the local pH changes around the end of the pipet. Combining this with finite element method (FEM) modeling, permeation coefficients for the series of acids can be extracted to determine the effect of permeant lipophilicity on permeability, using just one adjustable parameter (permeation coefficient) to model the data. Significantly, the trends observed are in quantitative agreement with measurements on solvent-free liposomes, confirming the validity of the technique. An attractive aspect of the methodology is that the effect of a potential field on the permeation rate of molecules can also be investigated, simply by positioning quasi-reference counter electrodes (QRCEs) on each side of the bilayer. Experimental investigations of the electric field effect on membrane transport are thus reported.

7.2 Principles

The simple method of BLM fabrication presented herein enables the rapid formation of solvent-free, suspended bilayers with exceptional electrical properties. To form these bilayers, a pulled theta glass pipet is filled with electrolyte solution and a QRCE (Ag/AgCl wire) is inserted into each barrel. A small potential (typically 100 mV) is applied between the two to ensure there is a well-formed meniscus at the end of the pipet before it is immersed into the lipid solution (1 mg ml^{-1} lipid-DPPC or EPC-in chloroform) (Figure 7.1A).

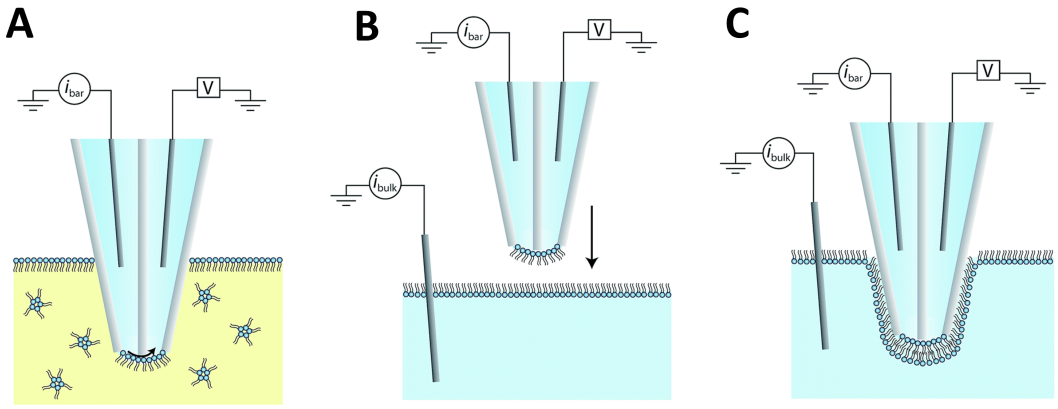

Figure 7.1: Schematic illustration (not to scale) of the bilayer formation process. A theta pipet (outer walls silanized) is lowered into a lipid solution (in chloroform) while applying a small potential between the two QRCEs to ensure the meniscus is well-formed (A). The pipet is held in the solution for approximately one minute before it is retracted, and the cell and solution replaced with an aqueous electrolyte. A small volume of lipid solution (in chloroform) is dropped onto the aqueous electrolyte and the volatile organic solvent allowed to evaporate forming a lipid monolayer (B). The pipet is then slowly lowered until the two monolayers make contact and a bilayer is formed (C).

This concentration is sufficiently high that a monolayer assembles at the oil/water interface. Upon immersion, the resistance between the QRCEs in the pipet barrels increases from ∼3-5 MΩ to ∼2-10 GΩ. The pipet is held in the lipid solution for approximately one minute to allow the monolayer to assemble, after which, it is removed, leaving the monolayer intact on the meniscus of the pipet and allowing any residual volatile solvent molecules to easily evaporate (Figure 7.1B). The pipet is then positioned above an electrolyte solution, onto the surface of which a small amount of lipid solution (10 μl) is dropped, forming a monolayer at the air-water interface. The volume of lipid solution required to ensure full monolayer coverage was determined by recording pressure/area isotherms

for 1,2-dipalmitoyl-sn-glycero-3-phosphocholine (DPPC) monolayers (used for the majority of experiments) using a Langmuir trough, and corresponded to a surface pressure of ca. 50 mN m^{-1}, similar to the pressure of cell membranes.[35]

The pipet is slowly lowered until the two monolayers make contact and a bilayer is formed (Figure 7.1C). Once formed, the current between one of the QRCEs in the pipet and a third QRCE in the bulk solution (i_{bulk} is monitored as the potential is scanned linearly to determine the resistance of the bilayer from the slope of the current-voltage curves produced (Figure 7.3).

Further, to validate the formation of a bilayer on the tip, gramicidin ion-channel incorporated bilayers were formed by the same procedure but using a 1 mg ml^{-1} lipid solution containing 0.5% (w/w) gramicidin. The ion current between the QRCEs in the pipet and bulk solution was monitored while the potential was swept linearly to determine any change in bilayer resistance due to the incorporation of gramicidin ion-channels into the bilayer.

For the measurement of permeation coefficients, the pipets are filled with the weak acid solution which is pH corrected to ensure the protonated form of the weak acid is the dominant species. Since charged species cannot permeate the bilayer to any detectable extent, it is important to ensure the carboxylic acids are in the neutral form.[36] The bulk solution, into which the molecules permeate, contains the pH-sensitive fluorophore fluorescein, and is adjusted to pH 8 so that any permeating weak acid molecules tend to dissociate, changing the pH locally. This pH change can be visualized using the confocal laser scanning microscope and the resulting fluorescence profiles analyzed with FEM simulations to elucidate permeation coefficients, as described herein (Figure 7.8).

7.3 Theory and simulations

Using FEM modeling, the steady-state fluorescence profiles that arise due to the permeating weak acid can be simulated as a function of permeation coefficient, which is the only adjustable parameter when matching simulations to experiment. For each weak acid (HX) studied, the following solution process was considered:

$$HX \rightleftharpoons X^- + H^+ \tag{1}$$

Where X^- is the conjugate anion of the weak acid, the concentration of which is dependent on the local pH and pKa of the weak acid. The bulk electrolyte solution was weakly buffered with 50 μM HEPES and thus the three protonation states of this buffer (neutral, negatively charged and doubly negatively charged) were also included. The protonation state of fluorescein has been shown to have no significant effect at the concentrations used here and was therefore ignored in the calculations.[1] The very fast kinetics of the protonation processes compared to the experimental timescale mean that they could be considered as equilibria controlled by the local pH. To ensure the equilibria were handled correctly, the pKa values for the weak acid and buffer were corrected for ionic activity using the Davies equation.[37]

For each species, i, in the simulation (H^+, X^-, HX, HEPES, $HEPES^-$, $HEPES^{2-}$), a time-independent solution to the following reaction-diffusion equation was sought:

$$D_\mathrm{i}[\frac{\partial^2 c_\mathrm{i}}{dr^2} + \frac{1}{r}\frac{\partial c_\mathrm{i}}{\partial r} + \frac{\partial^2 c_\mathrm{i}}{\partial z^2}] + R_\mathrm{i} = 0 \tag{2}$$

where c_i and D_i are the concentration and diffusion coefficient of species, i, respec-

tively, r and z are the radial and normal coordinates with respect to the center of the pipet (axi-symmetric cylindrical geometry), and R_{i} is the rate of production of species i in the domain (shown in Figure 7.2A).

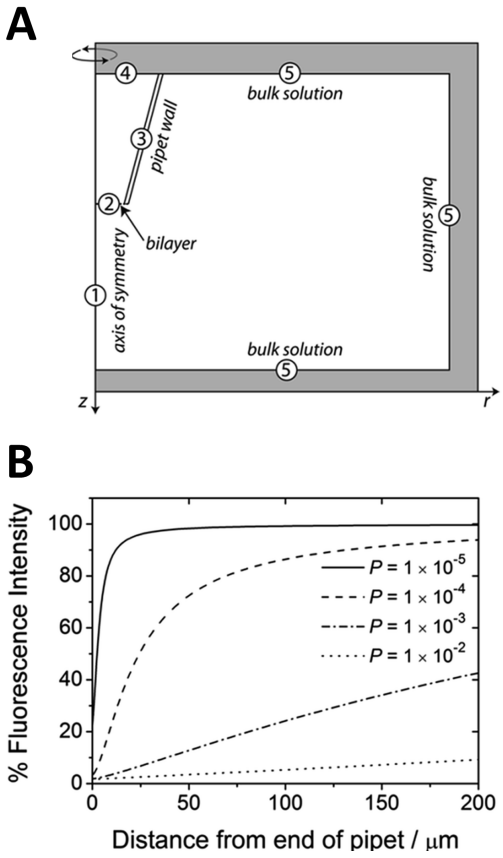

Figure 7.2: (A) Axi-symmetric cylindrical simulation domain for permeation coefficient determination. The pipet geometry is determined from optical microscopy and a range of permeation coefficients for the diffusion of the weak acid across the bilayer are simulated. (B) Series of simulated fluorescence profiles at different P values (units cm s^{-1}) for the permeation of 100 mM propanoic acid (see text for other parameters).

The finite element method was used to determine the steady-state concentration of each of the species by solving equation (2) subject to the boundary

conditions of the system, which are summarized in Table 7.1. Here N_{bilayer} describes the flux of the neutral weak acid across the bilayer (with $c^{\text{out}}i$ and $c^{\text{in}}i$, the concentration of the species on either side of the bilayer; $c^{\text{out}}i$ is the concentration outside the pipet, in the bulk solution, and $c^{\text{out}}i$ is the concentration inside the pipet). The initial bulk concentrations of each of the species, i, inside and outside of the pipet are denoted $c^{\text{in}^*}i$and $c^{\text{out}^*}i$.

Table 7.1: Summary of the boundary conditions used for the simulation of the permeation of a weak acid across a bilayer.

Label in Figure 7.2A	**Boundary**	**Equation**
1	Axis of symmetry	$0 = \nabla c_{\text{i}}\bar{n}$
2	Bilayer	$N_{\text{bilayer}} = P(C^{\text{out}}{}_{\text{HX}}$ - $C^{\text{in}}{}_{\text{HX}}$ $0 = \nabla c_{\text{i}}\bar{n}$, j = all other species
3	Pipet wall	$0 = \nabla c_{\text{i}}\bar{n}$
4	Top of the pipet	$C^{\text{in}}i = C^{\text{in}^*}i$
5	Bulk solution	$C^{\text{out}}i = C^{\text{out}^*}i$

The resulting steady-state profiles for H^+ were converted to pH and subsequently to fluorescence intensity (I) using the empirical relation determined previously in our group for the pH dependency of fluorescein fluorescence intensity, which was found to apply under these conditions.

$$I = 1\text{-}\ \frac{0.983}{1+e^{\text{-}3.36(6.18\text{-pH})}} \tag{3}$$

A series of simulation profiles are shown for a typical acid (propanoic acid) which visibly demonstrates that this methodology is sensitive to permeation rates

over 4 orders of magnitude (Figure 7.2B). Moreover, it is easily tuneable to a particular region by altering the experimental conditions: the pipet geometry, the pH of the internal and external solutions, and the buffer concentrations can all be varied.

7.4 Materials and Methods

Materials and reagents along with the method of determination of Pressure/Area Isotherms of DPPC, employed for this study were described in chapter 2.

7.4.1 Bilayer Formation and Recording Setup

Borosilicate glass theta capillaries (1.5 mm outer diameter, Harvard Apparatus Ltd) were pulled using a laser puller (P-2000, Sutter Instruments, USA) to produce pipets with tapered tip openings 5-10 μm in diameter (measured by optical microscopy). The two pipet barrels were filled with the weak acid solution to approximately half way using a MicroFil (World Precision Instruments, Inc.). The remaining details are given in Section 7.2. Two purpose-built high sensitivity current to voltage converters were used to simultaneously record the currents between the barrels (i_{bar}) and across the bilayer, between the barrel and bulk solution (i_{bulk}); see schematic in Figure 7.1C.

7.4.2 Confocal Laser Scanning Microscopy

CLSM experiments were performed using a Leica TCS SP5 X confocal fluorescence system on a Leica DMI6000 inverted microscope. An Argon laser at 488 nm

was used to excite the fluorescein in solution and the resulting emission was collected between 500 and 540 nm. Samples were mounted on an aluminium sample holder (fabricated in house) and the entire assembly was housed in a Faraday cage mounted on the CLSM stage. For visualization of weak acid permeation, the line scan frequency was 1400 Hz. After bilayer formation, the system was allowed to equilibrate for ∼30 s before a series of images were collected in the plane parallel to the bilayer at 1 μm intervals in the z-direction, to produce a 3D fluorescence image, related to the weak acid diffusion profile .

7.4.3 Analysis of CLSM Profiles

CLSM images were analyzed with MATLAB 2010a (Mathworks Inc., Cambridge, UK) to produce fluorescence profiles normal to the end of the pipet. A polynomial fit was applied to the data to reduce the experimental noise whilst preserving the shape of the profile. These polynomial fits were then matched to simulated profiles produced using COMSOL Multiphysics 4.2a (COMSOL AB, Sweden) to extract a permeation coefficient. For each pipet, the COMSOL model was parameterized from the experimental geometry and typically 135000 mesh elements were used, with the greatest resolution around the end of the pipet. Measurements were made on 2-3 bilayers for each acid and the errors shown on the resulting permeation coefficient are the standard deviation.

7.5 Results and Discussions

7.5.1 Bilayer characterization

After the formation of a lipid bilayer, suspended across the orifice of the pipet, the seal resistance was measured by recording current-voltage(i-V) curves, with the potential applied between the QRCEs on each side of the bilayer. The resistance varied over a fairly narrow range from ∼100 GΩ to ∼600 GΩ, with an average value of 260 ± 140 GΩ based on ∼15 independent measurements on different bilayers. These values are comparable to those previously reported in the literature for bilayers formed on similar sized apertures.[29,38,39]

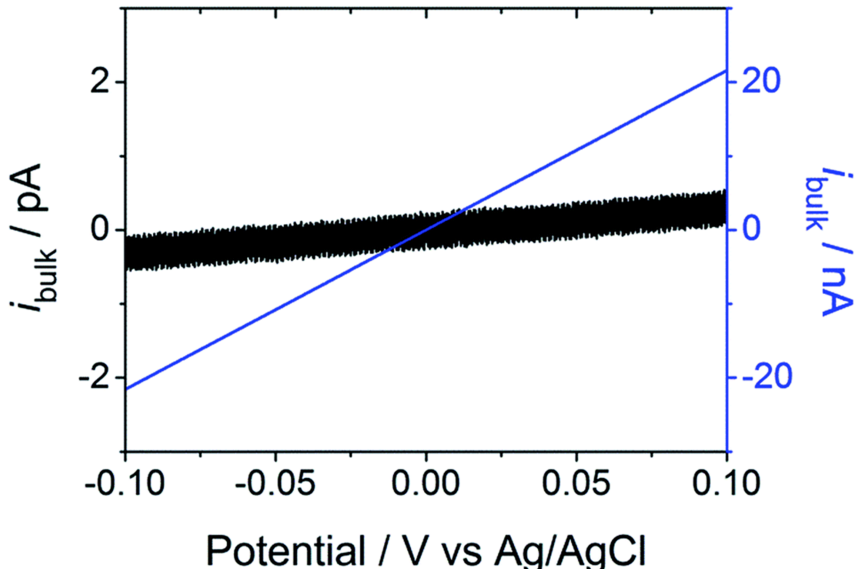

Figure 7.3: Typical current-voltage curves for an 8 μm diameter pipet containing 0.1 M KCl and 5 μM fluorescein in the bulk solution (0.1 M KCl, 50 μM HEPES and 5 μM fluorescein) before (blue line, right y-ordinate) and after (black line, left y-ordinate) DPPC bilayer formation. The open pipet and bilayer seal resistances are 4.6 MΩ and 330 GΩ, respectively.

Figure 7.3 shows typical i-V curves between a QRCE in the pipet and one in the bulk solution, before and after bilayer formation, with a typical increase in resistance of 5 orders of magnitude. For these measurements, as shown in Figure 7.1C, the potential of one of the QRCEs in the pipet was swept (with respect to ground) whilst the current was recorded at the QRCE in the bulk solution (on the other side of the bilayer) held at ground. In order to verify the formation of a bilayer on the pipet tip, i-V curves were recorded between the QRCEs in the pipet and the bulk solution for a gramicidin incorporated bilayer membrane (Figure 7.4).

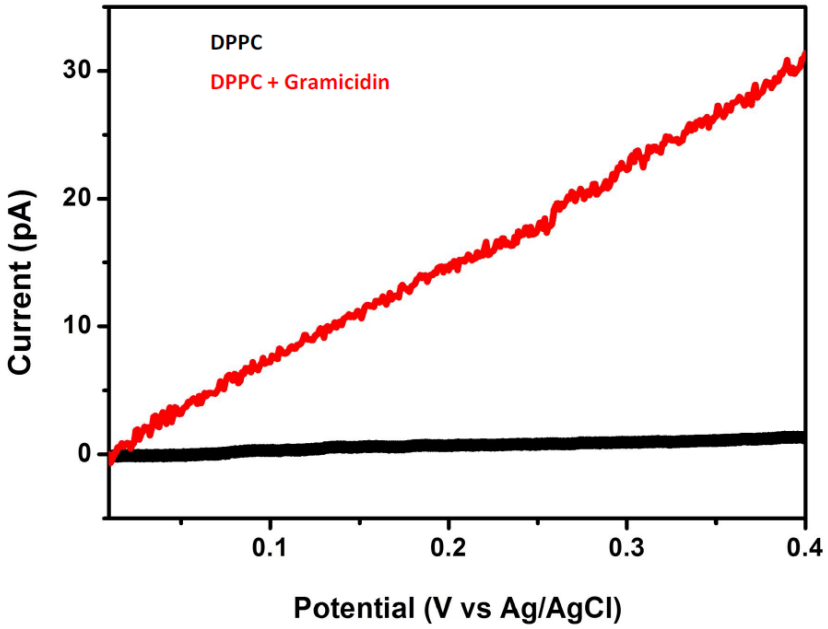

Figure 7.4: Current-voltage (i-V) curves for DPPC (black) and gramicidin incorporated DPPC (red) bilayer membranes. The bilayer seal resistance was found to decrease from ∼150 GΩ to ∼13 GΩ with the incorporation of gramicidin into the bilayer.

In a bilayer membrane, gramicidin acts as an ion-channel allowing transport

of monovalent cations (K^+ in this case), hence decreasing the bilayer membrane resistance. The membrane resistance was found to decrease from ~150 GΩ to ~13 GΩ after the incorporation of gramicidin into the bilayer, which is consistent with decrease in membrane resistances previously reported for supported bilayers confirming the assembly of a bilayer membrane at the pipet tip.[40]

7.5.2 Visualization of Weak Acid Transport

The microscale bilayer system, in which a suspended bilayer is formed at the tip of a tapered pipet, is advantageous compared to many existing permeation systems, since very high mass transport rates can be achieved at tapered micropipets and nanopipets in quiescent solution (without any need of stirring).[41-45] In contrast, in many previous studies permeation coefficients have typically been determined by measuring the flux of a permeant between two adjacent stirred chambers separated by a bilayer.[8] Stirring increases the rate of mass transport of the permeant to the bilayer, however, there is an unstirred region where the rate of transport is dominated by diffusion. In this unstirred layer (USL), which is often difficult to define precisely, a diffusive gradient exists between the bulk concentration of the permeant and the concentration at the bilayer interface.[46] This layer can extend for several hundred microns on either side of the bilayer and cause significant resistance to the rates of permeation that can be measured, since the rate at which a molecule crosses the USL is generally much slower than the rate of permeation across the bilayer itself.[1,47] Failure to correct for the USL can lead to large errors in the calculation of permeation coefficients and this appears to be one factor in explaining the variation in reported permeation coefficients for the same

molecules.[3,48] The method herein of using local pH changes to detect the rate of permeation eliminates any USL problems, since the permeant is delivered directly to the bilayer, and the resulting fluorescence profile is generated in seconds unlike conventional proton titration, bulk pH or tracer molecule studies which can take several hours.[2,5]

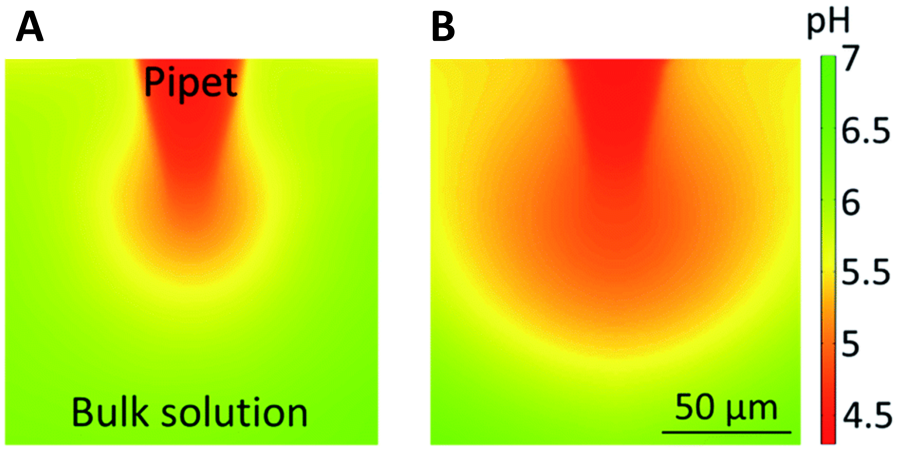

Figure 7.5: CLSM fluorescence intensity images showing the permeation of (A) 10 mM butanoic acid and (B) 10 mM hexanoic acid across DPPC bilayers formed on 8 μm tip diameter pipets.

Figure 7.5 shows example pH profiles for the permeation of 10 mM butanoic and hexanoic acid across DPPC bilayers formed on pipets with 8 μm diameter tip openings. It can clearly be seen that hexanoic acid produces a significantly larger decrease in pH on the trans (bulk solution facing) side of the membrane than butanoic acid, and, since the concentration of the permeant and size of the pipet are consistent, and the pKa values of the acids is similar (Table 7.2), the permeation coefficient must be higher in the hexanoic acid case. In fact, when the fluorescence profiles for the other acids at the same concentration are compared, there is a

clear correlation between the permeation rate and acyl tail length, indicating that permeability increases with lipophilicity (vide infra).

Table 7.2: Diffusion coefficient (D_{HX}), and pKa values for each weak acid studied.

Carboxylic Acid	**pKa**	**D_{HX}(10^{-6} cm^2s^{-1})**
Acetic Acid	4.76	12.71
Propanoic Acid	4.83	9.18
Butanoic Acid	4.83	8.17
Hexanoic Acid	4.85	7.84

7.5.3 Quantitative Determination of Permeation Coefficients

To identify the permeation coefficient, P, for each weak acid, a series of simulated fluorescence profiles was produced from the FEM model to allow the best match to the experimental profile to be determined (see Section 7.3). To correlate experimental data with the simulations, CLSM images were analyzed to produce fluorescence profiles normal to the end of the pipet. To calculate the average fluorescence, a cone of pixels was selected normal to the end of the pipet and the fluorescence intensity was plotted against the absolute distance from the end of the pipet. A polynomial fit was then applied to reduce the experimental noise and this fit was matched to simulated profiles to extract a permeation coefficient. A typical raw fluorescence profile for the permeation of 100 mM propanoic acid is shown in Figure 7.6 along with the polynomial fit which allows for easier comparison with the simulated data, while retaining the main features of the profile.

Figure 7.7A shows experimental fluorescence data for the case where a bi-

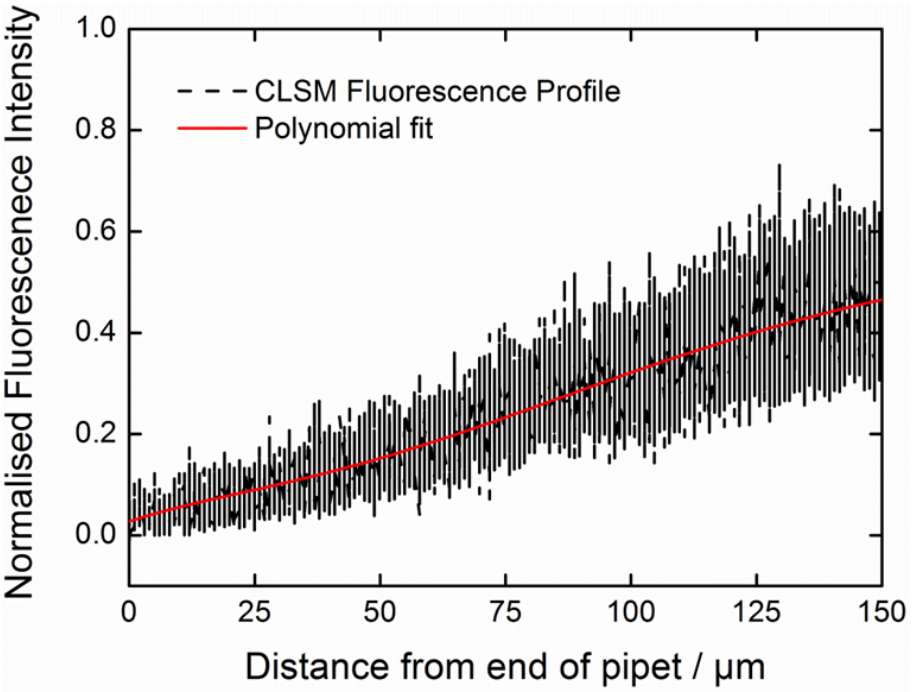

Figure 7.6: Fluorescence intensity-distance plot normal to the end of a pipet extending into the bulk solution, together with the corresponding polynomial fit for the permeation of propanoic acid (100 mM in the pipet).

layer at the end of a pipet separates a solution of pH 4.2 in the pipet (HCl) from bulk solution at pH 8. This firstly confirms that without a weak acid carrier, protons are confined to the pipet, as evidenced by a fairly sharp change in pH between the interior and exterior of the pipet. However, closer inspection of the profile in the region of the bilayer (pipet end) reveals a change in fluorescence (increase over a finite distance of ca. 25 μm) from the end of the pipet. This is an artefact of CLSM imaging at this magnification (10x objective). Light from outside the focal plane is not perfectly rejected, such that in the region around the end of the pipet the measured fluorescence is a combination of that from inside and outside the pipet. If this profile is compared to that of acetic acid, which shows the steepest

change in fluorescence between the inside and outside of the pipet (because of the lowest permeation coefficient), there is a clear difference between the two, and it is evident that this imaging artefact does not significantly affect the shape of the measured fluorescence profile over most of the distance (Figure 7.7B).

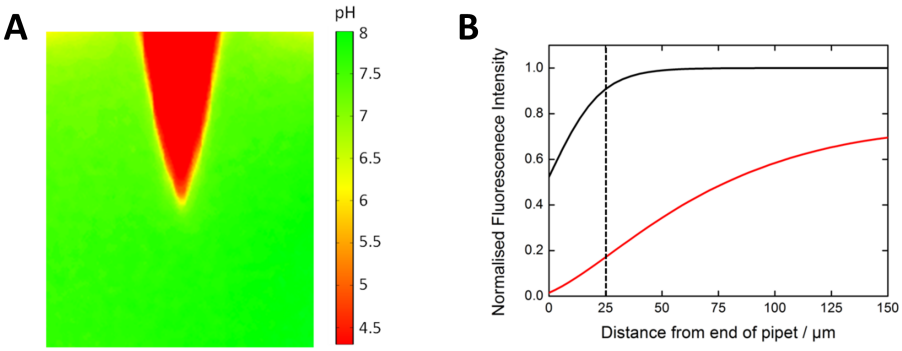

Figure 7.7: (A) CLSM image of a pipet containing only 0.1 M KCl at pH 4.2 after bilayer formation. (B) Fluorescence intensity profiles normal to the pipet orifice for the same pipet (black line) compared to that for 100 mM acetic acid at pH 4.2 (red line).

However, in order to reduce the error in fitting a simulated profile to the experimental data, the first 25 μm of each of the profiles was discarded; after this point the profile without weak acid has reached 90 % of its maximum value and so the contribution of this effect for further distances in the weak acid profiles can be reasonably assumed to be minimal.

Figure 7.8 shows a typical experimental profile for the permeation of 100 mM propanoic acid matched to the simulated data, using a permeation coefficient of 7.0 x 10^{-4} cm s^{-1} as the only adjustable parameter. Excellent agreement between experiment and simulation is evident.

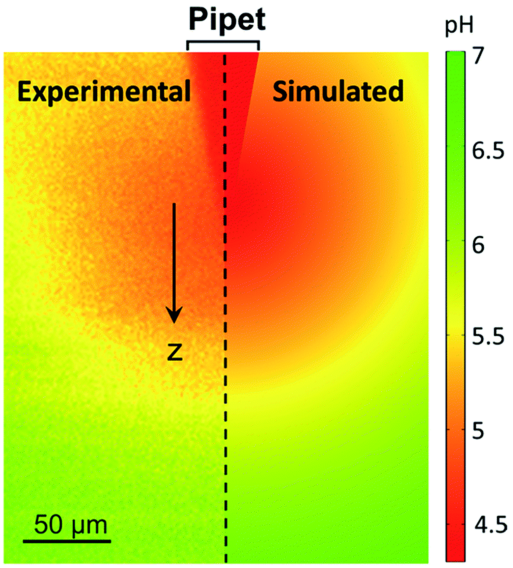

Figure 7.8: Experimental (left) and simulated (right) pH profile for the permeation of 100 mM propanoic acid across a DPPC bilayer located at the end of a pipet. A permeation coefficient of 7.0 x 10^{-4} cm s^{-1} was the only adjustable parameter used to fit the experimental data.

To analyze data, pH profiles in the z-direction, normal to the membrane, extending into the bulk solution were examined. Figure 7.9 shows the experimental profiles for each of the acids, which fit the simulated profiles well over the length scale shown, 25-150 μm from the end of the pipet. Further into the solution, the effects of natural convection will influence the transport process,[49] providing an upper limit on the range of the profiles considered. Note that, as discussed earlier, there are some optical effects due to the finite magnification of the CLSM system, and so to reduce these, data within 25 μm of the pipet on the trans side of the membrane were not analyzed.

As expected from visual inspection of the CLSM images, the permeation coefficients of each of the weak acids were found to increase monotonically with

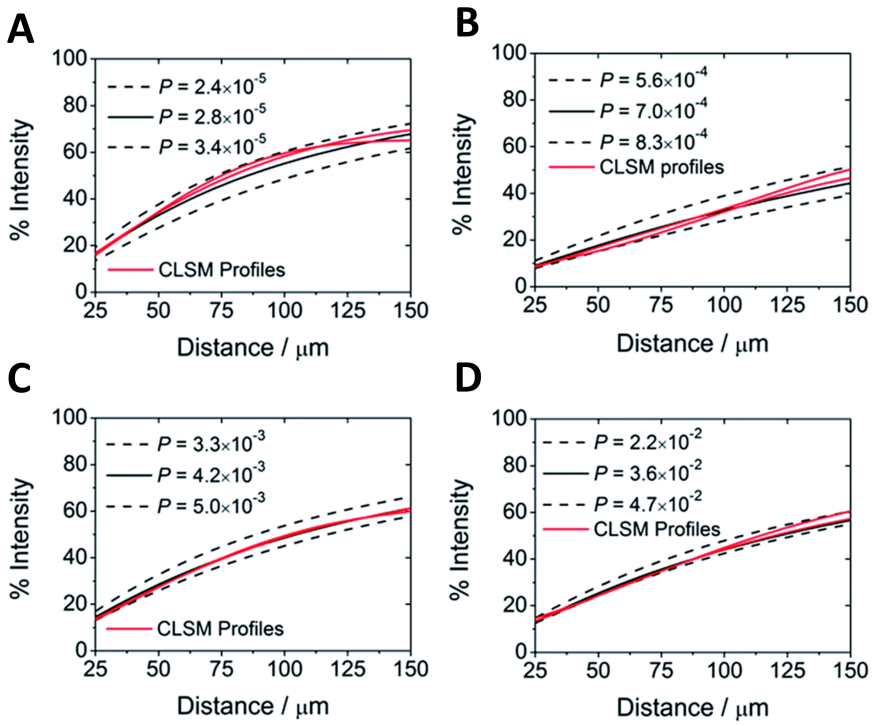

Figure 7.9: Experimental and corresponding simulated fluorescence-distance plot for (A) 100 mM acetic acid, (B) 100 mM propanoic acid, (C) 10 mM butanoic acid and (D) 10 mM hexanoic acid. The permeation coefficients corresponding to the upper and lower bounds and best fit of the CLSM data are shown (units cm s^1).

acyl tail length and water/octanol partition coefficient, K. The relationship of permeation coefficient to acyl tail length is shown quantitatively in Figure 7.10A for bilayers formed from both DPPC and soy PC. For propanoic and butanoic acid, permeation coefficients are rather similar for both types of bilayer. However, for weakly permeating acetic acid, it is evident that the bilayer type has a significant impact on transport rates, with much faster transport (by nearly two orders of magnitude) seen for soy PC compared to DPPC. This is because a bilayer formed from saturated lipids such as DPPC will be in the gel phase at room temperature

and hence will give slower permeation rates than unsaturated bilayers, formed from, for example, soy or egg phosphatidylcholine (PC), which exist in the fluid phase. Figure 7.10B shows how P changes with K, and also compares the permeation coefficients in this study to earlier values.

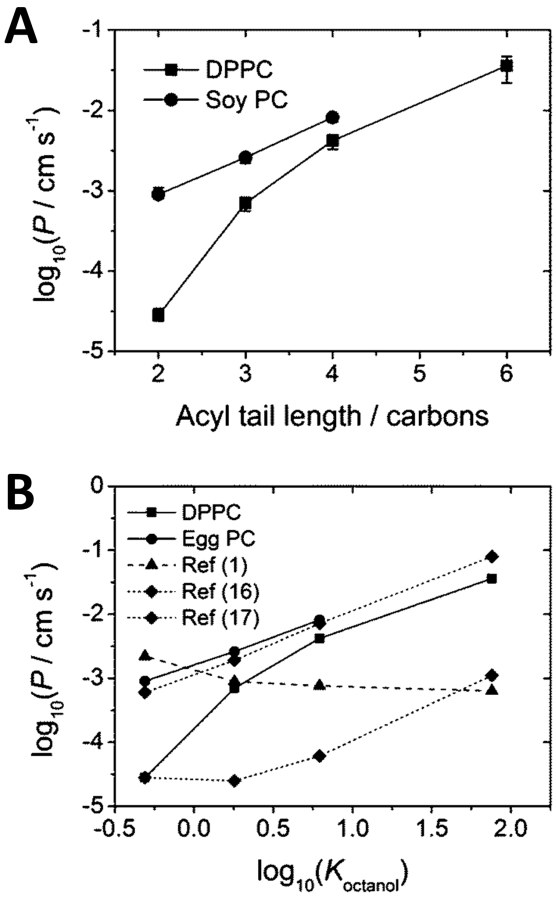

Figure 7.10: Plots of the permeation coefficient (P) of each weak acid across DPPC and soy PC bilayers vs. (A) acyl tail length and (B) water/octanol partition coefficient (K). In (B) data are also shown for three previous studies.

The data presented here lie within the range of values reported previously, although there is considerable variation in the values of previous studies. As

discussed above, the composition of a bilayer will influence its phase at room temperature, affecting molecular transport rates. Moreover, for membranes formed from soy or egg PC lipids, the paint brush method has commonly been used to form bilayers, leaving residual organic solvent molecules within the bilayers which may significantly impact on the rate of transport. This may explain the rather weak relationship between P and K seen in our earlier study;[1] data in Figure 7.10B.

The DPPC data obtained in the present study also show a strong linear trend between P and K with the exception of acetic acid, where the P value is lower than would be expected based on Overton's rule. This observation could be attributed to the gel phase structure of the bilayer creating a greater energy barrier for the permeation of the more hydrophilic molecule, compared to those with longer acyl tails.[50] Li and co-workers, avoided this issue by using a mixture of lipids to ensure the bilayers were in the fluid phase and which explains their higher reported permeation coefficients.[16] The data obtained on fluid phase (soy PC) bilayers herein, show a clear correlation between P and K, and are in excellent agreement with values reported by Li et al using spinning-disk confocal microscopy. The similarity of our reported permeation coefficients and those determined previously for both gel phase and fluid phase lipids confirms the validity of our new method of bilayer formation. In particular, the close match between the permeation coefficients determined with soy PC bilayers and those reported for unilamellar vesicles[16] confirms our assumption that this method produces uniform, solvent-free bilayers.

7.5.4 Effect of Potential Field on Permeability

The configuration developed herein is particularly attractive for allowing the ready study of electric field effects on the rate of transport of molecules across membranes. Potential fields have been shown to increase the rate of transport of ions across lipid membranes via the formation of pores within the membrane,[51,52] however, there is much less information on the effect of an applied electric field on molecular transport. It is reasonable to postulate that such electric-field induced pores could provide an additional route for the permeation of molecules.

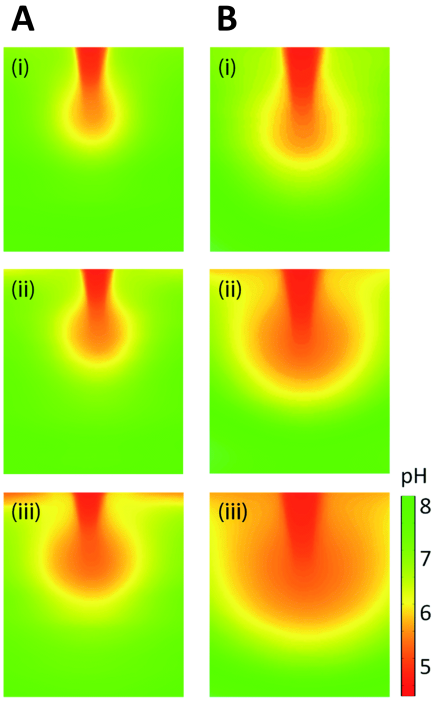

Figure 7.11: CLSM pH profiles illustrating the permeation of (A) 5 mM hexanoic acid at trans-membrane potentials of (i) 0 V, (ii) 0.5 V and (iii) 1 V and (B) 100 mM propanoic acid at potentials of (i) 0.1 V, (ii) 0.5 V and (iii) 1 V.

Figure 7.11B shows CLSM pH profiles of 5 mM hexanoic acid permeating

across bilayers with applied potentials of 0 V, 0.5 V and 1 V. It can be seen visually that there is a clear increase in permeability with increasing potential difference, supporting the idea that the potential field enhances membrane transport. Analysis of these profiles gave permeation coefficients of 6.5 x 10^{-3} cm s^1 at 0 V, 8.1 x 10^{-3} cm s^1at 0.5 V and 13 x 10^{-3} cm s^1 at 1 V, showing a two-fold increase in permeability from 0 to 1 V. This increase in permeability is unlikely to be due to an increased flux of protons through the pores formed, since the concentration of protons compared to the weak acid differs by over 3 orders of magnitude, indicating that the permeation coefficient of protons would have to be unfeasibly high to account for the change in pH on the trans side of the bilayer.[53]

The experiment was repeated with propanoic acid, yielding P values of 1.9 x 10^{-4} cm s^1 at 0.1 V, 2.3 x 10^{-4} cm s^1 at 0.5 V, and 3.1 x 10^{-4} cm s^1 at 1 V (Figure 7.11B), indicating that the effect of the potential field on permeability is not influenced by the lipophilicity of the molecule.

7.6 Conclusions

A new method of producing suspended BLMs containing negligible amounts of residual solvent molecules at the end of a tapered glass theta pipet has been described. The BLMs can be formed simply and rapidly, are durable over long time periods, and exhibit high seal resistances. This method can be readily coupled with microscopy techniques, such as CLSM used herein, to study the permeation of molecules across these bilayers. The permeation of a series of carboxylic acids across DPPC and soy PC bilayers has been investigated, by monitoring the change in fluorescence intensity of a pH-sensitive fluorophore, allowing the local pH change

to be visualized as the weak acid permeated the bilayer. A clear trend was observed from the fluorescence images, with the more lipophilic acids showing larger changes in pH and therefore faster permeation rates.

Accurate values for permeation coefficients have been extracted by fitting experimental data to simulated fluorescence profiles generated by a FEM model that is highly representative of the experimental geometry, so that the permeation coefficient is the only adjustable parameter. Analysis of the fluorescence profiles generated by each carboxylic acid demonstrated that the permeation coefficient is related to the partition coefficient, although the relationship does not strictly follow Overton's rule. This trend applied to both DPPC and soy PC bilayers, however, much higher permeation coefficients were observed for bilayers formed from lipids in the fluid phase (soy PC). An attractive feature of the experimental configuration is that electric field effects on permeation rates can readily be investigated. There is a clear impact of an applied electric field enhancing transport, which we attribute to the formation of pores in the membrane induced by the potential field.

Since weak acids and bases are commonly used as pharmaceutical agents, the technique developed is of considerable value in analyzing permeation rates of these molecules to determine how particular molecular characteristics influence rates of transport. Additionally, there are further possible applications of this technique to asymmetric bilayer studies, due to the method used to form bilayers, via the coupling of individual monolayers. These BLMs could also be investigated as a platform for ion-channel measurements due to their high seal resistances. Indeed, the ability to control the size of the pipet tip opening could allow the system to be optimized for single ion-channel recordings for possible applications as biosensors, where nanometer sized apertures are highly beneficial.[29,54]

7.7 References

[1] Grime,J. M. A., Edwards, M. A., Rudd, N. C.,Unwin, P. R., *Proc. Natl. Acad. Sci. U. S. A.* **2008**, 105, 1427714282.

[2] Wolosin, J. M., Ginsburg, H., *Biochim. Biophys. Acta*, **1975**, 389, 2033

[3] Walter, A., Hastings, D., Gutknecht J., *J. Gen. Physiol.* **1982**, 79, 917933.

[4] Walter, A., Gutknecht, J., *J. Membr. Biol.* **1984**, 77, 255264.

[5] Walter, A., Gutknecht, J., *J. Membr. Biol.* **1986**, 90, 207217.

[6] Evtodienko, V. Y., Kovbasnjuk, O. N., Antonenko, Y. N., Yaguzhinsky, L. S., *Biochim. Biophys. Acta*, **1996**, 1281, 245251.

[7] Orbach, E., Finkelstein, A., *J. Gen. Physiol.*, **1980**, 75, 427436.

[8] Missner, A., Kgler, P., Saparov, S. M., Sommer, K. , Mathai, J. C., Zeidel, M. L., Pohl, P., *J. Biol. Chem.* **2008**, 283, 2534025347.

[9] Kansy, M., Senner, F., Gubernator, K., *J. Med. Chem.* **1998**, 41, 10071010.

[10] Sugano, K., Nabuchi, Y., Machida, M., Aso, Y., *Int. J. Pharm.* **2003**, 257, 245251.

[11] Chen, X., Murawski, A., Patel, K., Crespi, C., Balimane, P., *Pharm. Res.* **2008**, 25, 15111520.

[12] Yamada, H., Shiku, H., Matsue, T., Uchida, I., *J. Phys. Chem.* **1993**, 97, 95479549.

[13] Tsionsky, M., Zhou, J., Amemiya, S., Fan, F.-R. F., Bard, A. J., Dryfe, R. A. W.,*Anal. Chem.* **1999**, 71, 43004305.

[14] Overton, C., *Vierteljahrsschr. Naturforsch. Ges. Zurich.* **1899**, 44, 88135.

[15] Overton, C., *Studies in Narcosis*, Chapman Hall, 1901.

[16] Li, S., Hu P. C., Malmstadt, N., *Biophys. J.*, **2011**, 101, 700708.

[17] Xiang, T.-X., Anderson, B. D., *Biophys. J.* **1998**, 75, 26582671.

[18] Tien, H. T., *Bilayer Lipid Membranes (BLM): Theory and Practice*, Dekker, New York, 1974.

[19] Mueller, P., Rudin, D. O., Tien, H. T., Wescott, W. C., *J. Phys. Chem.* **1963**, 67, 534535.

[20] Moscho, A., Orwar, O., Chiu, D. T., Modi, B. P., Zare, R. N., *Proc. Natl. Acad. Sci. U. S. A.* **1996**, 93, 1144311447.

[21] Montal, M., Mueller, P., *Proc. Natl. Acad. Sci. U. S. A.*, **1972**, 69, 35613566.

[22] Coronad, R., Latorre, R., *Biophys. J.* **1983**, 43, 231236.

[23] Ide, T., Ichikawa, T., *Biosens. Bioelectron.*, **2005**, 21, 672677.

[24] Malmstadt, N., Jeon, T. J., Schmidt, J. J., *Adv. Mater.* **2008**, 20, 8489.

[25] Lu, X., Leitmannova Ottova, A., Tien, H. T., *Bioelectrochem. Bioenerg.* **1996**, 39, 285289.

[26] Beddow, J. A., Peterson, I. R., Heptinstall, J., Walton, D. J., *Anal. Chem.* **2004**, 76, 22612265.

[27] Hirano, M., Kobayashi, T., Ide, T., *e-J. Surf. Sci. Nanotechnol.*, **2008**, 6, 130133.

[28] Shim, J. W., Gu, L. Q., *Anal. Chem.* **2007**, 79, 22072213.

[29] White, R. J., Ervin, E. N., Yang, T., Chen, X., Daniel, S., Cremer, P. S., White, H. S., *J. Am. Chem. Soc.* **2007**, 129, 1176611775.

[30] Schibel, A. E. P., Edwards, T., Kawano, R., Lan, W., White, H. S., *Anal. Chem.* **2010**, 82, 72597266.

[31] Tien, H. T., Ottova-Leitmannova, A., *Membrane Biophysics*, Elsevier, Amsterdam, The Netherlands, 2000.

[32] Li, S., Hu, P., Malmstadt, N., *Anal. Chem.* **2010**, 82, 77667771.

[33] Suarezisla, B. A., Wan, K., Lindstrom, J., Montal, M., *Biochemistry*, **1983**, 22, 23192323.

[34] Hirano, A., Wakabayashi, M., Matsuno, Y., Sugawara, M., *Biosens. Bioelectron.* **2003**, 18, 973983.

[35] Marsh, D., *Biochim. Biophys. Acta, Rev. Biomembr.* **1996**, 1286, 183223.

[36] Saparov, S. M., Antonenko, Y. N., Pohl, P., *Biophys. J.* **2006**, 90, L86L88.

[37] Davies, C., *Ion Association*, Butterworths, London, **1962**.

[38] Schibel, A. E. P., Heider, E. C., Harris, J. M., White, H. S., *J. Am. Chem. Soc.* **2011**, 133, 78107815.

[39] Fertig, N., Meyer, C., Blick, R. H., Trautmann, C., Behrends, J. C., *Phys. Rev. E: Stat., Nonlinear, Soft Matter Phys.* **2001**, 64, 040901.

[40] Andersen, O. S. , *Biophys. J.* **1983**, 41, 119133.

[41] Li, Q., Xie, S., Liang, Z., Meng, X., Liu, S., Girault, H. H., Shao, Y., *Angew. Chem., Int. Ed.*, **2009**, 48, 80108013.

[42] Bruckbauer, A., Zhou, D., Ying, L., Korchev, Y. E., Abell, C., Klenerman, D.,*J. Am. Chem. Soc.* **2003**, 125, 98349839.

[43] Taylor, G., Girault, H. H. J., *J. Electroanal. Chem.* **1986**, 208, 179183.

[44] Williams, C. G., Edwards, M. A., Colley, A. L., Macpherson, J. V., Unwin, P. R., *Anal. Chem.* **2009**, 81, 24862495.

[45] Snowden, M. E., Gell, A. G., Lai, S. C. S., McKelvey, K., Ebejer, N., OConnell, M. A., Colburn, A. W., Unwin, P. R., *Anal. Chem.* **2012**, 84, 24832491.

[46] Barry, P. H., Diamond, J. M., *Physiol. Rev.* **1984**, 64, 763872 .

[47] Korjamo, T., Heikkinen, A. T., Mnkknen, J., *J. Pharm. Sci.* **2009**, 98, 44694479.

[48] Antonenko, Y. N., Denisov, G. A., Pohl, P., *Biophys. J.* **1993**, 64, 17011710.

[49] Rudd, N. C., Cannan, S., Bitziou, E., Ciani, I., Whitworth, A. L., Unwin, P. R., *Anal. Chem.* **2005**, 77, 62056217.

[50] Xiang, T. X., Anderson, B. D., *Biophys. J.* **1997**, 72, 223237.

[51] Weaver, J. C., Chizmadzhev, Y. A., *Bioelectrochem. Bioenerg.* **1996**, 41, 135160.

[52] Kinosita, K., Ashikawa, I., Saita, N., Yoshimura, H., Itoh, H., Nagayama, K., Ikegami, A., *Biophys. J.* **1988**, 53, 10151019.

[53] Deamer, D. W., J. B*ioenerg. Biomembr.* **1987**, 19, 457479 .

[54] Bayley, H., Cremer, P. S., *Nature*, **2001**, 413, 226230

Chapter 8

Conclusions

The aim of this thesis was to further the understanding of various interfacial processes by developing different electrochemical techniques capable of studying the interfacial physicochemical and biochemical processes. To achieve this different electrochemical scanning probe microscopy based systems were developed and tested and are presented in this thesis.

In chapter 3, an easy and fast fabrication of a nanoscale dual carbon probe was attempted. These probes are well suited to investigate various interfacial phenomena because of their relatively small footprint, enabling close positioning onto an interface, while the small inter-electrode distance leads to high sensitivity. In addition, a FEM model was developed to assist in characterizing these probes based on simple steady-state limiting current measurements. It was demonstrated that the dual carbon probes developed herein can be used to interrogate interfaces and surfaces with high sensitivity by employing them to assess local changes ionic flux during illumination of a thylakoid membranes and in 2D imaging of a single thylakoid membrane. In both cases, subtle interactions of electrogenerated elec-

tron acceptors with the active surface were determined readily using an SECM based electrochemical measurement scheme. In addition, we have shown that individual electrodes within these probes can be functionalized, as exemplified by selective deposition of Pt on one electrode while leaving the other one unmodified. Platinized nanoelectrodes have been shown to be promising probes for intracellular measurements hence these probes may find applications as single-cell chemical sensors and other modifications are evidently realizable.

As presented in chapter 4, a nanoscale pH-scanning ion conductance microscopy probe was developed to extend the use of electrochemical scanning probe microscopy for simultaneous topographical and potentiometric imaging of surfaces and interfaces. The capability of these probes for generating spatially resolved pH maps of surfaces and interfaces has been demonstrated by employing them to image topographically challenging calcite microcrystals. Both the pH distribution and height change yielded rates that are consistent with expected values based on known dissolution kinetics, highlighting the promise of these probes for high resolution quantitative pH mapping in the future.

In Chapter 5, a fast and inexpensive method to fabricate multifunctional probes for electrochemical imaging and voltammetric studies were reported. These probes incorporates key features of two popular electrochemical scanning probe microscopy techniques namely the scanning electrochemical microscopy and scanning electrochemical cell microscopy and hence is an extremely powerful tool for localized electrochemical investigation of surfaces even in non-aqueous environments. This is particularly noteworthy, as electrochemical measurements in non-aqueous environment with SECM are recognized to be difficult especially in case of room temperature ionic liquids where the low diffusion coefficients and often large differ-

ences of the diffusion coefficients of oxidized and reduced species, making steady-state feedback measurements difficult with micrometer sized probes and hitherto necessitating the use of extremely high redox concentrations with smaller probes. Further, the capability of these probes for transient current measurements on insulating and reactive surfaces were also demonstrated, suggesting the prospect of surface titrations and adsorption/modification measurements on a wide range of surfaces. In general, these probes permit simultaneous detection of multiple targets in a confined droplet, which may allow many interesting and difficult substrates to be investigated in the future.

The detection and investigation of individual molecules in solution and near a surface represents a major frontier in analytical chemistry, following the emergence of electrochemical and optical techniques. However, while optical methods have evolved into powerful spectroscopic techniques electrochemical methods have lagged behind mainly because of the huge technical challenges in isolating, detecting and measuring the electrochemical current produced by a single molecule. Chapter 6, described a new type of probe based approach, employing a nanoscale tunable electrochemical droplet cell for single molecule electrochemical detection that overcomes previous limitations. A significant advantage of this method is the ability to characterize the tip-substrate separation and electrode area directly, instead of relying on the redox electrochemical signal itself, as in some past work, which provides an indirect estimate of these parameters. The currents generated during single molecule electrochemical detection were supported by a random walk simulation (3D), which indicates that the molecule rapidly explores the entire volume of the droplet. In the future, by increasing the probe electrode area in combination with the high sensitivity capability realized here, potential dependent

measurements could become possible. Moreover, in an alternative configuration employing independently addressable electrodes, it would become possible to measure the spatial location of a molecule in addition to redox cycling.

Finally, in chapter 7 a new method of planar bilayer lipid membrane formation is presented that allows stable, solvent-free lipid bilayers exhibiting high seal resistances to be formed rapidly, easily and reproducibly. Using these bilayers the passive permeation of a series of week acids is investigated, to determine quantitatively the trend in permeability with lipophilicity of the acid. Since weak acids and bases are commonly used as pharmaceutical agents, the technique developed is of considerable value in analyzing permeation rates of these molecules to determine how particular molecular characteristics influence rates of transport. Additionally, there are further possible applications of this technique to asymmetric bilayer studies, due to the method used to form bilayers, via the coupling of individual monolayers. Also the ability to control the size of the pipet tip opening could allow this system to be optimized for single ion-channel recordings for possible applications as biosensors, where nanometer sized apertures are highly beneficial

In conclusion, the rage of techniques developed and described in this thesis were demonstrated to have the capability to aid the visualization of interfacial ion fluxes and could open up new avenues for the understanding of various physiochemical and biochemical interfacial processes.